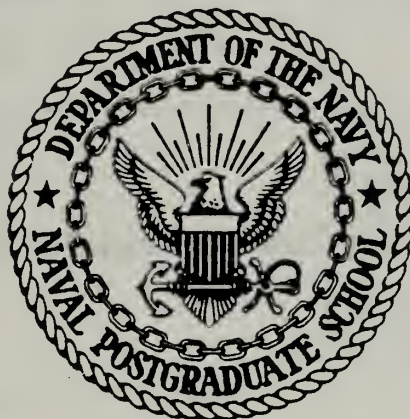


NPS ARCHIVE
1983
CALLAND, W.

Donnerstag, Knox Library, NPS
Monterey, CA 93943

NAVAL POSTGRADUATE SCHOOL

Monterey, California



THESIS

QUASI-LAGRANGIAN DIAGNOSTICS APPLIED
TO AN EXTRATROPICAL EXPLOSIVE
CYCLOGENESIS IN THE NORTH PACIFIC

by

Wynn E. Calland

June 1983

Thesis Advisor:

C. H. Wash

Approved for public release; distribution unlimited.

T209077

REPORT DOCUMENTATION PAGE

READ INSTRUCTIONS
BEFORE COMPLETING FORM

1. REPORT NUMBER		2. GOVT ACCESSION NO.	3. RECIPIENT'S CATALOG NUMBER
4. TITLE (and Subtitle) Quasi-Lagrangian Diagnostics Applied to an Extratropical Explosive Cyclogenesis in the North Pacific		5. TYPE OF REPORT & PERIOD COVERED Master's Thesis, June 1983	
7. AUTHOR(s) Wynn E. Calland		6. PERFORMING ORG. REPORT NUMBER	
9. PERFORMING ORGANIZATION NAME AND ADDRESS Naval Postgraduate School Monterey, California 93940		8. CONTRACT OR GRANT NUMBER(s)	
11. CONTROLLING OFFICE NAME AND ADDRESS Naval Postgraduate School Monterey, California 93940		10. PROGRAM ELEMENT, PROJECT, TASK AREA & WORK UNIT NUMBERS	
14. MONITORING AGENCY NAME & ADDRESS (if different from Controlling Office)		12. REPORT DATE June 1983	
		13. NUMBER OF PAGES 154	
		15. SECURITY CLASS. (of this report) Unclassified	
		15a. DECLASSIFICATION/DOWNGRADING SCHEDULE	
16. DISTRIBUTION STATEMENT (of this Report) Approved for public release; distribution unlimited.			
17. DISTRIBUTION STATEMENT (of the abstract entered in Block 20, if different from Report)			
18. SUPPLEMENTARY NOTES			
19. KEY WORDS (Continue on reverse side if necessary and identify by block number) Western Pacific, Explosive Maritime Cyclogenesis, Quasi-Lagrangian Diag- nostics, FGGE Year, Mass Budget, Vorticity Budget, Stability Analysis, Synoptic Discussion			
20. ABSTRACT (Continue on reverse side if necessary and identify by block number) A case of explosive extratropical cyclogenesis in the North Pacific is analyzed employing quasi-Lagrangian diagnostic techniques in isobaric coordinates. The First GARP Global Experiment (FGGE) Level III-b data set from the European Center for Medium-range Weather Forecasting (ECMWF) is used in a synoptic investigation and mass and vorticity budget diag- nostic evaluation of storm development.			

Mid-tropospheric positive vorticity advection (PVA) acts in concert with low-level thermal advection to enhance surface layer organization during the initial periods. Explosive development occurs under upper-level zonal flow when the surface system, developing along the low-level baroclinic zone, moves under the front left quadrant of a strong jet streak. Stability in the lower troposphere decreases steadily as an intense two-layer mass circulation is established. The divergence term provides the largest contribution to the vorticity tendency during explosive development due to substantial surface layer convergence and upper-level divergence.

Approved for public release; distribution unlimited

Quasi-Lagrangian Diagnostics Applied to an
Extratropical Explosive Cyclogenesis in the North Pacific

by

Wynn E. Calland
Lieutenant, United States Navy
E.S. , United States Naval Academy, 1975

Submitted in partial fulfillment of the
requirements for the degree of

MASTER OF SCIENCE IN METEOROLOGY AND OCEANOGRAPHY

from the

NAVAL POSTGRADUATE SCHOOL
June 1983

ABSTRACT

A case of explosive extratropical cyclogenesis in the North Pacific is analyzed employing quasi-Lagrangian diagnostic techniques in isobaric coordinates. The First GARP Global Experiment (FGGE) Level III-b data set from the European Center For Medium-range Weather Forecasting (ECMWF) is used in a synoptic investigation and mass and vorticity budget diagnostic evaluation of storm development.

Mid-tropospheric positive vorticity advection (PVA) acts in concert with low-level thermal advection to enhance surface layer organization during the initial periods. Explosive development occurs under upper-level zonal flow when the surface system, developing along the low-level baroclinic zone, moves under the front left quadrant of a strong jet streak. Stability in the lower troposphere decreases steadily as an intense two-layer mass circulation is established. The divergence term provides the largest contribution to the vorticity tendency during explosive development due to substantial surface layer convergence and upper-level divergence.

TABLE OF CONTENTS

I.	INTRODUCTION	12
II.	ENVIRONMENTAL DATA BASE DESCRIPTION	18
	A. FGGE DATA	18
	B. SUMMARY OF ANALYSES AND PROGNOSSES UTILIZED . .	21
III.	QUASI-LAGRANGIAN DIAGNOSTIC (QLD) TECHNIQUES . . .	22
IV.	SYNOPTIC OVERVIEW	29
	A. GENERAL	29
	B. MODEL PREDICTION PERFORMANCE	30
	C. SYNOPTIC DISCUSSION	33
V.	MASS BUDGET ANALYSIS	49
	A. GENERAL	49
	B. POTENTIAL TEMPERATURE AND STATIC STABILITY ANALYSIS	50
	C. HORIZONTAL MASS FLUX	54
	D. VERTICAL MASS TRANSPORT	59
	E. CONCLUSIONS	61
VI.	VORTICITY BUDGET ANALYSIS	63
	A. GENERAL	63
	B. TIME SECTIONS , TIME TENDENCIES AND SELECTED PROFILES	64
	C. LATERAL TRANSPORT	68
	D. MEAN MCDE LATERAL TRANSPORT	71

E.	EDDY MCDE LATERAL TRANSPORT	73
F.	VERTICAL REDISTRIBUTION	77
G.	SOURCES AND SINKS	80
H.	RESIDUALS	82
I.	CONCLUSIONS	84
VII.	CONCLUSIONS AND RECOMMENDATIONS	87
APPENDIX A.	FGGE DATA BIAS CHARACTERISTICS	89
APPENDIX E.	TABLES	93
APPENDIX C.	FIGURES	100
LIST OF REFERENCES	151
INITIAL DISTRIBUTION LIST	153

LIST OF TABLES

TABLE I.	Availability of FGGE Data	93
TABLE II.	Listing of Analyses and Prognoses Utilized .	94
TABLE III.	Generalized QLD Budget Equation in Isobaric Coordinates	95
TABLE IV.	QLD Mass Budget Equations in Isobaric Coordinates	96
TABLE V.	QLD Circulation Budget Equations in Isobaric Coordinates	97
TABLE VI.	Mean and Eddy Mode Transport Equations . . .	99

LIST OF FIGURES

Figure 1.	The Overall Data Management During FGGE . .	100
Figure 2.	Storm Track Positions and SLP Analyses. . .	101
Figure 3.	36-h Forecast SLP and Storm Position Errors.	102
Figure 4.	Synoptic Fields for 0000 GMT 12 January 1979.	103
Figure 5.	DMSP Visual Satellite Imagery for 0041 GMT 12 January	104
Figure 6.	DMSP Infrared Satellite Imagery for 0041 GMT 12 January	105
Figure 7.	Same as Figure 4 except for 0000 GMT 13 January	106
Figure 8.	Same as Figure 5 except for 2341 GMT 12 January	107
Figure 9.	Same as Figure 6 except for 2341 GMT 12 January	108
Figure 10.	Same as Figure 4 except for 0000 GMT 14 January	109
Figure 11.	FNCC SST Analysis Valid 1200 GMT 14 January	110
Figure 12.	Same as Figure 5 except for 1405 GMT 13 January	111
Figure 13.	Same as Figure 6 except for 1405 GMT 13 January	112
Figure 14.	Same as Figure 5 except for 0023 GMT 14 January	113
Figure 15.	Same as Figure 6 except for 0023 GMT 14 January	114
Figure 16.	Same as Figure 4 except for 1200 GMT 14 January	115
Figure 17.	Same as Figure 5 except for 1205 GMT 14 January	116

Figure 18.	Same as Figure 6 except for 1205 GMT 14 January	117
Figure 19.	Same as Figure 4 except for 1800 GMT 14 January	118
Figure 20.	Same as Figure 5 except for 2124 GMT 14 January	119
Figure 21.	Same as Figure 6 except for 2124 GMT 14 January	120
Figure 22.	Same as Figure 4 except for 0000 GMT 15 January	121
Figure 23.	Same as Figure 4 except for 0000 GMT 16 January	122
Figure 24.	Same as Figure 5 except for 1005 GMT 16 January	123
Figure 25.	Same as Figure 6 except for 1005 GMT 16 January	124
Figure 26.	Same as Figure 4 except for 0000 GMT 17 January	125
Figure 27.	Area-Averaged Potential Temperature Time Sections	126
Figure 28.	Stability Index	127
Figure 29.	Corrected Lateral Mass Transport Time Sections	128
Figure 30.	Radial Section of Lateral Mass Transport .	129
Figure 31.	Radial Section of Lateral Mass Transport .	130
Figure 32.	QID Derived Vertical Velocities	131
Figure 33.	FGGE Derived Vertical Velocities	132
Figure 34.	Kinematic Vertical Velocities	133
Figure 35.	Budget Volume Absolute Vorticity	134
Figure 36.	Area-averaged Absolute Vorticity Vertical Time Sections	135

Figure 37.	Absolute Vorticity Vertical Time-Tendency Sections	136
Figure 38.	Total, Mean and Eddy Mode Lateral Vorticity Transport	137
Figure 39.	Same as Figure 37 except for Lateral Vorticity Transport.	138
Figure 40.	Same as Figure 37 except for Mean Mode Lateral Transport.	139
Figure 41.	Same as Figure 37 except for Eddy Mode Lateral Transport.	140
Figure 42.	Same as Figure 37 except for Lateral Vorticity Divergence.	141
Figure 43.	Same as Figure 37 except for Lateral Vorticity Advection.	142
Figure 44.	Divergence of the Vertical Transport.	143
Figure 45.	Same as Figure 37 except for Vertical Vorticity Divergence.	144
Figure 46.	Same as Figure 37 except for Vertical Vorticity Advection.	145
Figure 47.	Same as Figure 37 except for the Tilting Term.	146
Figure 48.	Same as Figure 37 except for Frictional Dissipation.	147
Figure 49.	Same as Figure 37 except for Budget Residuals.	148
Figure 50.	FGGE 6-h Radius 6 Vorticity Budget Fields .	149
Figure 51.	FGGE 6-h Stability Trace.	150

ACKNOWLEDGEMENT

Suggestions by Jim Peak and Mike McDermet in computational and graphics areas were greatly appreciated. Had it not been for their ready answers to perplexing problems, many hours would have needlessly been spent. I would also like to thank the many courteous and industrious computer operators at the W. R. Church computer center. A special thanks goes to Dr. R. L. Elsberry for his critical and extensive review of this document. I sincerely appreciate all the time and efforts of Dr. C. H. Wash. This thesis would not have been started were it not for his suggestions, knowledgeable insight, and direction. Finally, and most importantly, my love and heartfelt thanks are extended to my wife, Barbara. Without her unfailing support this thesis effort would never have been accomplished.

I. INTRODUCTION

Extratropical maritime cyclones restrict commercial, industrial and military use of the sea. The more intense storms which form over very small time periods are especially dangerous to navigation due to the effects of the associated wind, waves and visibility restrictions. Accurate and reliable prediction of these atmospheric processes has been a goal for many decades. During the past few decades, significant advances in forecasting these synoptic-scale atmospheric circulation features have been realized through the development of numerical weather prediction (NWP) models.

While current numerical models provide satisfactory accuracy in forecasting most synoptic-scale processes, they perform poorly in predicting the predominantly cold-season explosive genesis of maritime cyclones. Sanders and Gyakum (1980) define explosive cyclogenesis as an extratropical cyclone which undergoes central pressure falls of at least 1 mb/h for 24 h. Accurate forecasting of these meteorological events is limited by the scarcity of observations over oceanic areas, which inhibits the model initialization process, and by the smaller spatial and temporal scales of the explosively developing cyclone.

Accurate forecasting of these maritime events is of great significance to commercial, industrial and military organizations which routinely use the oceans in the transaction of business and in the fulfillment of commitments. Several recently publicized examples, specifically, the loss of the Russian trawler Metrostoy (Mariners Weather Log, 1979), and the sinking of the oil rig Ocean Ranger (Lemoyne, 1982), illustrate only a minute fraction of the total loss of life and operational hazards associated with these intense meteorological events.

Explosive deepening is a characteristic of the vast majority of the most intense cyclones (Sanders and Gyakum, 1980). In connection with associated severe weather and the failure of numerical forecast models to accurately predict these events, it is of paramount importance that the processes which contribute to the formation of these vigorous storms be examined and fully understood. Several recent studies have focussed attention on detailed analyses of these processes. Roman (1981) completed a mass budget study and Conant (1982) completed a circulation and angular momentum budget study of a case of east-coast cyclogenesis. Intercomparisons of these results with conclusions derived

in this thesis provide valuable insight into the formative mechanisms of maritime explosive cyclogenesis and lead to a general quantitative understanding of the forecast problem associated with these intense systems.

This thesis is part of a broadly-based research effort attempting to understand better the formative processes inherent in the genesis of maritime cyclones. Specifically, this study concentrates on a clearly defined structured approach to the analysis of a case of explosive cyclogenesis over the North Pacific Ocean during the period 12-17 January 1979. The mass and circulation (vorticity) budgets are examined using quasi-Lagrangian diagnostics (QLD) as developed by Johnson and Downey (1975 a and b) in order to determine the role of dynamic forcing in the budget volume. The local contribution of vorticity sources and sinks and the vertical and horizontal mass and vorticity transports are specifically explored.

Identification of these processes is uniquely interesting in that the cyclone under study consists of the classic frontal wave development from strong low level baroclinicity. The distinguishing feature is the absence of a strong migratory short wave aloft, which categorizes this storm as

a Petterssen type-A system, as opposed to the type-B feature which contains a 500 mb short wave responsible for the rapid surface deepening (Petterssen and Smebye, 1971). In the type-A case, the flow aloft is predominantly zonal through the early explosive deepening phase with positive vorticity advection of minor significance. Low level thermal advection plays the important role in the deepening process. This thesis is believed to be one of the first detailed analyses of this class of maritime storms. In addition, the vast majority of explosive deepeners form in the North Pacific Ocean (Sanders and Gyakum, 1980). Inasmuch as the most severe weather is directly associated with these severe storms, this study assumes particular significance in attempting to understand this meteorological phenomenon in order to minimize its disastrous effects.

The specific approach employed in this thesis is the use of QID techniques in an isobaric spherical coordinate system which is translated with the storm. Horizontal advection associated with wave translation is isolated from the relative advection and the divergence of the transport associated with cyclone development. The fluctuations of meteorological variables are then analyzed through the use

of a cylindrical budget volume centered on and translating with the cyclone surface center. Vertical distributions, lateral exchanges and sources and sinks of cyclone properties resulting from purely developmental processes are then analyzed. Application of QLD techniques in studying cyclone development (Wash, 1978) has proven valuable in diagnoses of poorly forecast storms, and Roman (1981) and Conant (1982) have demonstrated QLD applicability in detailed analyses of east-coast cyclogenesis.

The main objectives of this thesis are:

- A synoptic investigation of the classical frontal wave cyclogenesis in the North Pacific Ocean;
- A synoptic assessment of the validity of the First GARP Global Experiment (FGGE) data and the quality of the FGGE analyses for depicting storm dynamical processes;
- A diagnostic investigation of storm dynamics through the use of QLD budget analyses of mass and vorticity.

The detailed analyses of these processes is further aided by an exceptionally strong supporting data base. The case under study occurred during the first special observation period (SOP-1) of the First GARP Global Experiment (FGGE). This FGGE data set was assimilated by the European Center for Medium-range Weather Forecasting (ECMWF) and obtained through the auspices of the Goddard Space Flight Center. This data set is special, in that observations from

aircraft, ships, buoys and satellites gathered during an intense collection effort were manually checked and then systematically integrated into a dense network of observations. Consequently, the supporting data base analyzed in this thesis effort is exceptionally broad-based, complete, and integrated into a well-diversified observational network.

Quantitative analysis of FGGE-type data bases gives specific insights into development processes inherent in maritime explosive cyclogenesis. In the following chapters, examination of the FGGE data (Chapter 2) and an abbreviated description of QLD procedures (Chapter 3) are presented. Chapter 4 discusses the cyclone under study through a synoptic overview which highlights significant flow patterns and associated upper and lower-level features. Chapters 5 and 6 present the results of the budget calculations and Chapter 7 contains specific conclusions from these budget calculations and discusses recommendations for further research.



II. ENVIRONMENTAL DATA BASE DESCRIPTION

A. FGGE DATA

During the first special observation period (SOP-1) of the Global Weather Experiment, the largest concentration of meteorological resources ever assembled was deployed to observe the atmosphere and oceans. The quality of the data generated from this effort marked a milestone in the development of numerical weather prediction models and synoptic meteorology in general. By any standard, this experiment showed an unparalleled example of scientific cooperation and excellent resource management.

The FGGE Level III-b data set used in this thesis was constructed from observations integrated through a data assimilation system at ECMWF. Bengtsson et al., (1982) describe the system as a three-dimensional, multivariate, optimum interpolation scheme using a nonlinear normal-mode initialization and an automatic system for data checking. The direct field-level observations (Level I-b) were transformed into the basic meteorological variables (Level II-b), which constituted the basic meteorological product of the

experiment. A 15-level model with horizontal resolution of 1.875 degrees of latitude and longitude was used to transform the Level II-b data to Level III-b. At the III-b level, the observations were manually checked and objectively analyzed into a set of dynamically derived meteorological fields. The flowchart of this data assimilation process is depicted in Fig. 1. The FGGE Level III-b data production effort was completed in June 1981 and the data fields were catalogued for 6-h observations for all standard levels up to and including 10 mb. A detailed description of this assimilation scheme can be found in Bengtsson et al., (1982).

The FGGE data base is currently undergoing validation by a variety of groups. Roman (1981) and Conant (1982) demonstrated its validity on a case of east-coast cyclogenesis. In an independent assessment of the FGGE data set, Halem et al., (1982) present a detailed analysis in connection with the coverage and accuracy of the remote sensing portion of the network covering the oceanic regions. Analyses based on these inputs provided the following conclusions:

- The FGGE observing system has a positive effect on forecast skill using S1 criteria;
- Significant corrections to the 300 mb first guess fields occur over oceanic regions with the FGGE data;
- Nearly all of the forecasts that retain useful skill by day five show a positive impact from the FGGE system;
- In certain synoptic situations, the FGGE observing system is capable of measuring the atmosphere globally with sufficient accuracy for current NWP models to make useful extended-range forecasts beyond one week.

These and other conclusions as well as a detailed description of the analysis scheme can be found in Halem et al., (1981) and Baker et al., (1981). It is evident from these and other studies that the FGGE Level III-b data set provides a strong foundation for accomplishing the objectives of this thesis.

A summary of the FGGE data availability by field-type and level is depicted in Table I. The advantages of this type of augmented data support over the standard data base include:

- A considerably richer data base, particularly over data-sparse oceanic areas;
- The high resolution grid is convenient for depicting the smaller synoptic-scale features associated with cyclogenesis;
- Basic and derived fields (vertical velocity, humidity, etc.) are included in the data set;

- The full area of cyclogenesis and storm translation enjoys similar data coverage.

These significant advantages demonstrate the value of the FGGE Level III-b data set in quantitative analyses of storm features.

B. SUMMARY OF ANALYSES AND PROGNOSSES UTILIZED

Three sets of analyses are utilized in this thesis:

- National Meteorological Center (NMC) analyses and prognoses;
- Fleet Numerical Oceanography Center (FNOC) analyses and prognoses;
- ECMWF Level III-b analyses.

These analyses are used in conjunction with the synoptic discussion (Chapter 4) and for the verification of the forecast problem alluded to earlier. A complete listing of all analyses and prognoses utilized in this study is contained in Table II. A complete description of the FNOC products can be found in the U.S. Naval Weather Service Numerical Environmental Products Manual (NAVAIR 50-1G-522).

III. QUASI-LAGRANGIAN DIAGNOSTIC (QLD) TECHNIQUES

To derive generalized budget analysis techniques for processes related to cyclone development, changes in the budget volume properties due to migration of the system must be separated to isolate true developmental trends. In the past, synoptic-scale diagnostic approaches (e.g. Kung and Baker, 1975) evaluated storm processes relative to a fixed coordinate system. This type of approach is effective for selected time periods when storm translation is negligible, but suffers markedly when applied to rapidly translating systems of appreciable intensity. In particular, changes may occur due to system movement, system development, or both. The only accurate approach to assess true developmental fluctuations associated with cyclone development is to construct a moving budget volume centered on some distinguishing storm feature. In this way, horizontal advection associated with wave translation may be isolated. In addition, any vertical redistribution of a budget property may be analyzed in terms of vertical transport processes within the cyclone budget regime. QLD techniques employed in this

thesis provide the means for this type of approach. Roman (1981) and Conant (1982) have demonstrated the validity of this type of approach on a case of east-coast cyclogenesis.

To study the fluctuations in any storm property, a generalized budget equation is constructed in terms of the storm budget coordinate system. The equation consists of the time rate of change of the desired budget quantity (df/dt) and the lateral flux transport, vertical flux transport and sources/sinks (see Table III). The equation is applicable to the storm budget volume in spherical coordinates. The spherical portion of the atmosphere incorporated within the budget volume is approximated by a cylinder for ease in computations and definition of budget properties. This approximation is valid for the relatively thin slab of atmosphere (1000-100 mb) selected for budget analyses.

The formulation of the storm budget coordinate system and details of the budget equation notation are discussed by Wash (1978). The storm budget volume is defined in terms of 10 mandatory pressure levels in the vertical, and in the horizontal by outwardly directed radii originating from a central point. For example, the budget property at a point

may be analyzed by describing the level/layer (1000/925 mb), the budget radius in degrees of latitude from the storm center (6), and the quadrant desired (grid points 1-36). The mass and vorticity budget equations employed in this analysis are depicted in Tables IV and V respectively.

In the mass budget (Table IV), the general equation representing the change in mass with time is composed of contributions from lateral and vertical transports. The lateral transport term represents the net horizontal convergence of mass flux within the budget volume. The vertical transport is calculated through the use of derived vertical velocity fields and is necessarily a reflection of net lateral flux into the volume. Application of boundary conditions that vertical motion is zero at the top and bottom surfaces of the budget volume simplifies the equation, as shown in the middle of Table IV.

Several useful relationships can be derived from this simplified equation and the boundary conditions. Contributions to the mass time tendency in isobaric coordinates arises chiefly from pressure fluctuations in the surface layer, as the other layers in the budget are fixed pressure surfaces. This term is computed easily and with

considerable accuracy. The net lateral mass transports in the layers are calculated from the wind fields and necessarily balance the vertical transports through continuity. Errors in the wind fields cause the vertically integrated lateral mass transport to differ from the vertically integrated mass tendency, and cause a residual in the budget.

Application of the boundary conditions to the divergence of the vertical transport causes the vertical sum to vanish, and thereby isolates the residual correction which must be applied layer by layer to force the vertical sum of the divergence to zero. The O'Brien (1970) linear correction scheme is utilized to correct for these residual imbalances. The upper layers are weighted more due to the greater inaccuracies of the wind measurements at these levels. These corrections are applied to the layer mass transports, and are combined with the translation correction (discussed earlier) to give the final corrected form of the mass transport term. The vertical velocities representing the vertical mass transport are then recovered through continuity.

In the vorticity budget formulation, the contributions to vorticity changes occur from lateral and vertical fluxes, sources and sinks (Table V, Section A). The flux (transport) terms can be expanded into divergence and advection contributions by the use of vector identities (Table V, Section B), which facilitates further insight into the physical processes they represent. The source/sink terms arise from net generation/dissipation of vorticity within the budget volume, and in isobaric coordinates are comprised of divergence, tilting and friction components. Notice that three divergence terms arise from this expansion of the general vorticity budget equation. The horizontal transport component is identical to the source divergence term, and the horizontal and vertical transport components are equal and opposite. Thus, the net contribution of divergence in the budget is manifest in the source term. A specific breakdown of the partitioned vorticity budget equation is presented in Section B of Table V.

To isolate the contributions of both the rotational and irrotational wind components to the transport of a desired budget quantity, mean and eddy modes (analogous to divergence and advection terms in the vorticity equation),

are derived from the transport terms (Table VI). The purpose of this technique is to isolate the changes in the mean budget properties from those occurring on the eddy scale. Thus, a comprehensive analysis of the lateral and vertical flux terms can be made by separating them into mean and eddy mode contributions and comparing them with the divergence and advection terms for analysis of the physical processes they represent. The relation of the mean/eddy mode and divergence/advection partitions to the total transport is also illustrated in Section B of Table V.

The budget analysis begins with the choice of the particular property to be analyzed. The next step in the budget calculations consists of interpolating the u and v components of the FGGE data set onto the cylindrical budget volume grid. Next, the interpolated winds are converted to tangential and radial components relative to the outer volume boundary and corrected for storm motion. In this form, the data are ready to be used in the budget equations discussed above. Derived fields (moisture, vertical velocity, kinetic energy, etc.), not directly used in budget computations can be used to supplement insight into storm dynamics. Interesting comparisons between FGGE derived

vertical velocity and QLD calculated vertical velocity, for example, serve to validate the QLD technique approach.

The QLD approach provides insight into the following key properties:

- The magnitude and significance of the horizontal mass transport structure;
- The magnitude and significance of the horizontal vorticity transport structure;
- The vertical transport structure of mass and vorticity derived from vertical motion estimates;
- The magnitude and nature of source/sink contributions to budget analyses.

The next chapter discusses the development sequence of the storm through a synoptic discussion utilizing synoptic fields, analyses and forecasts, and satellite imagery.

IV. SYNOPTIC OVERVIEW

A. GENERAL

Oceanic cyclogenesis mechanisms can in part be portrayed by graphical representation of pertinent meteorological and oceanic fields. This chapter explores the synoptic conditions associated with a specific case of North Pacific explosive cyclogenesis during 12-17 January 1979. An attempt is made to gain insight into formative processes and possible factors related to the serious shortcomings in the model representation of the dynamics associated with these vigorous events. Use is made of FGGE data analyses, Defense Military Satellite Program (DMSP) imagery and FNOC sea surface temperature (SST) analyses. Comparisons are made between FGGE, FNOC and NMC sea level pressure analyses and prognoses to highlight differences in forecast deepening rates and analyzed and forecast storm positions. Explosive deepening criteria were adopted from Sanders and Gyakum (1980), who addressed the NMC 7-layer PE model performance associated with "explosive" prediction. Predicted deepening rates for the cyclones they studied were consistently less

than 1/3 of the observed rates, and North Pacific explosive deepening east of the dateline was virtually missed by the model. An assessment of the FNOC 5-layer PE model performance (Gyakum, 1981) demonstrated similar results. Specifically, the model captured only 1/3 of the observed central pressure falls for all time periods. In addition, the most accurate of all the forecasts were shown to be valid between 24-36 h. In comparing the FGGE analyses with the FNOC and NMC analyses, it should be noted that the FNOC analyses and prognoses are derived from the 5-layer PE coarse mesh (381 km horizontal resolution) model. In contrast, the NMC analyses are strictly hand-analyzed Northern Hemisphere strips, while the prognoses are derived from the 7-layer PE fine mesh (190.5 km horizontal resolution) model.

B. MODEL PREDICTION PERFORMANCE

The storm track (at 12-h increments) is presented in Fig. 2a. The cyclone develops southeast of Japan in the vicinity 30N, 135E and transits toward a final position off the west coast of Alaska. Notice the significant translation increase after 0000 GMT 13 January. The 5-day evolution (0000 GMT 12 January 1979 to 0000 GMT 17 January 1979) in central sea-level pressure, as analyzed from the FGGE

data, NMC and FNOC analyses, is illustrated in Fig. 2b. Assuming the representativeness of the FGGE data, both series of FNOC and NMC analyses fail markedly in representing the intense deepening phase (0000 GMT 13 to 0000 GMT 15 January 1979). There is close agreement between FGGE and NMC analyses at other times. It appears that specific inputs to the FGGE data set (mentioned earlier) not available to FNOC or NMC for real-time analyses provide a more accurate portrayal of the deepening period. Close inspection of the observations included in the FGGE analyses shows that the deepening phase is well documented at all levels. At 1200 GMT 14 January 1979, for example, as many as seven sea-level observations from land and sea stations are available in the north and east quadrants of the storm and form the surface data network. In the upper levels, satellite-derived temperature and height anomalies, and 250 mb aircraft winds and temperatures combine to form a dense observational network. In the NMC analysis, ship reports in the area were conspicuously absent, as the analysis appeared to be based upon land stations only. The FNOC analysis, however, contained four of the seven FGGE surface observations, but did not contain the two observations

closest to the storm center, and this caused a misrepresentation of the surface central pressure. Thus, the more accurate representation of the deepening phase in the FGGE analysis is directly attributed to a superior data base and not just to the benefit of a "better" first guess.

A comparison between the 36-h sea-level pressure forecasts is shown in Fig. 3a. All curves show the general deepening trends, but the FNOC and NMC forecasts consistently lag the FGGE analyzed pressure, and are highly variable in predicting the magnitude of the central pressure falls. From these displays, it is evident that both models fail significantly in the timely and accurate prediction of storm intensification, especially during the explosive stage. This example illustrates further the forecast problems discussed by Sanders and Gyakum (1980) alluded to earlier.

The location error in 36-h storm positions for NMC and FNOC predictions, relative to the FGGE analyzed position, is presented in Fig. 3b. It is clearly seen that significant errors exist in both forecasts at various times during the deepening phase. Such significant errors in the analyzed and forecast features of this system reflect an inability of

current operational models to accurately forecast these events.

C. SYNOPTIC DISCUSSION

The synoptic analysis approach in this section consists of an examination of the basic meteorological fields in three displays of two fields each. Display A contains 250 mb winds and isotachs, B presents 500 mb heights and absolute vorticity, and C shows 1000-500 mb thickness and sea-level pressure patterns. This approach generally allows only subjective insights into features of interest during the storm life cycle. The quantitative analysis of the dynamical processes is presented in the following chapter. The intent of this section is to trace the development of the system through a synoptic discussion of major features contributing to overall storm development.

Examination of atmospheric conditions at 0000 GMT 12 January 1979 in the area southeast of Japan shows marked cyclogenetic potential. The surface picture (Fig. 4c) is dominated by a broad trough (vicinity 30N, 140E) extending northeast-southwest through the center of a checkerboard pattern of fairly strong low and high centers. The significant features include the Siberian High near 55N, 100E (just

off the western edge of the chart) which is very strong and stationary. The parent low in the vicinity of 53N, 170E is now quasi-stationary and filling (950 mb). A large maritime high (1030 mb) dominates the north central Pacific (vicinity 30N, 178W), and the northern fringe of Typhoon Alice is just visible near 20N, 140E). The combination of flow from these systems serves to funnel cold, polar continental air southward towards northward flowing warm, moist tropical air, which enhances the frontogenesis potential. A general destabilization of the polar air occurs north of the area of strong low level baroclinicity shown by the concentration of thickness contours just east of Japan.

In the mid-troposphere (Fig. 4b), two distinctive features are evident. The flow over the western Pacific is dominated by an extensive region of low heights associated with a quasi-stationary long wave trough, which is a portion of a four-wave planetary pattern. This significant feature accounts for the steady progression of mobile short waves and associated surface features through the region during the preceding week, in addition to supporting the steady flow of cold air off the Siberian continent. The second major feature of interest is the predominantly zonal flow

over the entire incipient region with areas of weak and small absolute vorticity upstream.

In the upper troposphere (Fig. 4a), the presence of a broad jet (> 50 m/sec) aloft is a further manifestation of the baroclinicity of the lower troposphere. As yet, significant jet streak (> 75 m/sec) propagation into the region remains well upstream, and therefore is not a factor in the low-level development.

Examination of the visual (Fig. 5) and infrared (Fig. 6) satellite imagery valid at 0041 GMT 12 January 1979 shows a couplet of similar low level cloud masses (labelled A and B) southeast of Japan. Lack of significant vertical development is evident on the infrared imagery, in contrast to the area of enhanced convection (labelled C) associated with an area of positive vorticity advection (PVA) upstream over Korea (Fig. 4b). Cloud mass B is the precursor of a weak cyclone which moves to the east and rapidly dissipates. Cloud mass A is the precursor of the cyclone analyzed in this study. The evolving low-amplitude "s-shape" configuration with a distinct edge on the western flank is indicative of increasing thermal and low level absolute vorticity gradients with time (Weldon, 1977). Although fairly small, the

cloud mass is beginning to take on the familiar "leaf-shape" which Weldon (1977) characterizes as typical of incipient oceanic cyclogenesis.

During the next 24 h ending at 0000 GMT 13 January 1979, surface development continues (vicinity 35N, 150E) into a closed center (995 mb). The incipient system (Fig. 7c) appears as a broad area of low pressure, and the development of a weak thermal ridge near the surface center indicates frontogenesis continues during the period. Ships in the vicinity reported seas on the order of 15 ft, with periods ranging between 3-5 s, which indicates a duration limited wave spectrum. Of interest is the continued strengthening of the Siberian high (now 1080 mb) which steadily pumps cold air southward, in association with the backside circulation of the stationary cold low to the east. Destabilization of the surface layer continues as cold air streams southward over the warm ocean surface, and a polar low has become organized over the southeast tip of Japan due west of the incipient system (indicated on detailed NMC analyses, not shown here).

In the mid-troposphere (Fig. 7b), the 500 mb low anchored off the Kamchatka Peninsula has deepened. A short

wave with an associated broad absolute vorticity area has formed over Japan, approximately 800 nm upstream of the incipient system. A smaller, less distinct vorticity area has formed directly over the surface system.

Increased vorticity in the mid-troposphere can also be linked to the approach of a jet streak from the west. At this stage, however, the position of the jet streak indicates only minimal influence on the low-level circulation, as the jet core is directly superposed in the vertical, and no clear pattern of cyclonic shear or diffluence can be seen at 250 mb (Fig. 7a).

The increased vertical development over the period can be seen in the DMSP satellite imagery (Figs. 8 and 9) valid at 2341 GMT 12 January 1979. The developing system is labeled A and is centered approximately 600 nm southeast of Japan. Cold plumes extend for virtually the entire breadth in the infrared image (Fig. 9), with cloud tops becoming progressively warmer toward the tapered end to the southwest. Enhanced convection and continued development of the leaf structure is shown in the visual image (Fig. 8). The region under the leaf appears to contain marked baroclinicity in a zone in advance of the propagating jet streak

aloft, which is similar to the conditions observed by Weldon (1977) in a case study.

During the following 24-h period ending 0000 GMT 14 January 1979, continued development is evident in the low and middle troposphere. Central surface pressure (Fig. 10c) falls steadily to 977 mb, which is a decrease of 18 mb. If one adopts the explosive criteria of Sanders and Gyakum (1980) for a latitude of 40 degrees, the storm has entered the explosive stage during this period. The surface low moves rapidly toward the northeast, to a position close to the maximum SST gradient (Fig. 11). Close proximity to this gradient fulfills another observation of explosive development described by Sanders and Gyakum (1980). Analysis of the thickness contours (Fig. 10c) indicates a pattern of diffluence 10 degrees of longitude downstream from the surface center. The diffluence at 10 degrees upstream is considerably greater. Bjerknes (1954) showed that these conditions favor formation of a diffluent trough in the upper levels within the cyclonic shear zone north of the jet streak axis. The NW-SE tilt of the 500 mb trough evident by 1200 GMT 14 January (Fig. 16b), combined with the favorable superposition of the jet streak support the

diffluent trough formation argument. In addition, a combination of the superposition of the upper level divergence zone over the surface center and the approach of the upper-level thermal trough in close proximity to the 500 mb trough promotes self-amplification through the mid-troposphere. Mid-level vorticity increases due to the movement of concentrated cyclonic shear vorticity into the budget volume as the jet enters the diffluent trough. As a result, increased vertical development occurred from vorticity increases as a result of jet streak interaction and self-amplification.

Indeed, the first evidence of mid-tropospheric development is visible in Fig. 10b. The vorticity pattern has an expanded area of significant vorticity associated with the mid-tropospheric circulation. A region of strong vorticity also exists upstream northeast of Japan, but that center appears to be associated with the polar low forming to the west (Fig. 10c), as indicated earlier. The interesting feature to notice is the absence of the short wave that was present over Japan 24 h earlier, which would seem to indicate that further explosive development from the short wave PVA aloft is unlikely.

At 250 mb (Fig. 10a), however, the arrival of the jet streak (maximum velocity 85 m/sec) in favorable superposition over the surface system acts to promote the lower-level circulation. Diffluence in the region of the jet stream split and cyclonic wind shear to the left of the jet axis combine to induce positive circulation increases and strong vertical motion through the mid-troposphere. Increased vertical motion enhances vertical redistributions of all properties, including an increase in the convergence in the surface layer, and hence, explosive development continues.

Inspection of satellite imagery (Figs. 12 and 13 valid 1405 GMT 13 January 1979 and Figs. 14 and 15 valid at 0023 GMT 14 January 1979) shows a discernable comma-shape formation. In Figs. 12 and 13, the southern boundary of the jet axis is delineated by subsidence along the cirrus band paralleling the low-level front. The jet crosses just south of the vortex at A. The very cold tops evident near the vortex center and along the frontal band indicate strong convection throughout the region. An interesting feature in Figs. 14 and 15 is the relatively low level clouds (labeled A) that appear as fingers extending from the vortex center and look similar to feeder bands. When coupled with the

extensive cirrus shield aloft, the cloud pattern presents a hurricane-like appearance. Two significant changes have occurred during the past 10 h. The area of deep convection has expanded markedly both near the vortex and along the frontal band, which indicates continued strengthening. Second, the storm has organized to the point that clear slots have formed in the cold air behind the front, which indicates the penetration of cold and subsiding air toward the vortex.

During the next 12-h period ending 1200 GMT 14 January 1979, the surface pressure falls an additional 11 mb to 965 mb (Fig. 16c). Notice the shift of the reference grid 10 degrees to the north and 30 degrees to the east in this and subsequent figures. The increased amplitude of the thickness ridge implies increased circulation in the lower troposphere, most probably as a result of warm advection and extreme latent heating from deep convection. Sensible heat input presumably weakens during the period as the storm center moves north of the maximum SST gradient (shown earlier in Fig. 11).

At 500 mb (Fig. 16b), self-amplification continues with the development of the upper-level trough and associated

vorticity maximum. The apparent lack of appreciable vorticity advection at this level suggests that continued intensification of the system must be manifest in either the lower or upper levels. The most likely factors which serve to maintain the deepening phase consist of a combination of processes: jet stream interaction at 250 mb; and the extreme surface convergence generating pockets of sustained deep convection.

An increase in cyclonic vorticity appears at the 250 mb level during this time frame (Fig. 16a). Cyclonic curvature and shear to the left of the jet axis continues to promote the circulation discussed above. The wind speeds in the jet have diminished slightly in intensity due to the decreased baroclinicity through the lower troposphere.

Strong development of the system during the previous 12 h is indicated in Figs. 17 and 18 (valid at 1205 GMT 14 January 1979). Vertical velocities within the storm volume increase during the period, as deep convection becomes intense and widespread surrounding the vortex and along the entire frontal band. The growth of convective activity indicates that development continues upward through the troposphere during the period, as the jet crosses the

frontal band at a more northerly point. In addition, the "hook" or tip of the cloud band in the northwest sector develops markedly. In typical cases (Weldon, 1977), these conditions indicate the onset of the mature stage.

Interestingly, the next 6-h period ending 1800 GMT 14 January 1979 marks the most explosive period of the storm's development cycle. The surface pressure (Fig. 19c) falls 18 mb (averaged between FGGE and NMC analyses). Ship observations at 1200 and 1800 GMT were limited in both analyses. It is possible that some of the extreme deepening observed during this 6-h period actually occurred before 1200 GMT, but there were inadequate ship observations to detect it. Thus, the magnitude of the surface pressure fall may be less than mentioned above or presented in Fig. 3b. In any event, the nature of the explosive deepening has caused the thickness ridge to double in amplitude along an east-west orientation, indicating that cold air has begun to wrap around the vortex at the surface. In the mid-troposphere (Fig. 19b), the positive vorticity center elongates along the flow and intensifies slightly. The elongation of the vorticity center and the continued digging of the mid-level trough indicate the system should weaken in

the near future (Weldon, 1977). At 250 mb (Fig. 19a), evidence still suggests that the jet stream is in favorable superposition over the surface system and is continuing to induce vertical motion and associated low-level convergence. Although the jet remains fairly stationary and strong, the surface low continues northeast at a high speed, which suggests decreased jet influence in future development.

A look at the satellite imagery (Figs. 20 and 21) valid at 2124 GMT 14 January 1979 shows the storm at maximum development. The dry tongue aloft has penetrated to the vortex center. A solid deck of stratocumulus to the southeast of the vortex center exists in the strong cyclonic surface flow. An interesting "hole" appears to the east of the vortex in the dense frontal band clouds, which is not due to orographic effects as the area is still south of the Aleutian chain. A detailed look at the preceding satellite picture (Fig. 17a) shows a clear slot formed in about the same relative position. Thus, the feature is associated with the rotation of the cloud band around this dry tongue in the strong cyclonic flow at the surface, and gives the appearance of the formation of a secondary vortex in the frontal band. Further inspection of this imagery shows the

continuance of strong vertical motion induced by deep convection along the frontal band, and to the north and east of the vortex center. The penetration of cold air into the vortex is visible and signals the start of the occlusion phase.

At 0000 GMT 15 January 1979, the surface circulation is dominated by the surface low over the Aleutian Islands (Fig. 22c) with a central pressure at 947 mb. The explosive period has ended with the onset of the occlusion process. The thickness gradient has diminished markedly, and a polar low is organized in the cold air to the west, while a new disturbance forms along the baroclinic zone to the southwest. At 500 mb (Fig. 22b), a closed circulation has formed, which indicates cold air influx through most of the troposphere. A broad positive vorticity pattern exists, but negative vorticity advection into the region is inducing subsidence and filling. The system is vertically stacked, which also indicates the fully mature stage. At 250 mb (Fig. 22a), development of the trough is evident from the cyclonic rotation of the wind vectors. The jet has diminished in intensity due to the reduced low-level baroclinicity and the migration of the surface system north of the jet axis.

During the next 24 hours ending 0000 GMT 16 January 1979, the occlusion process continues. The surface system (Fig. 23c) has stalled over the west Alaskan coast and filled to 955 mb. Ship reports in the vicinity show 35 ft seas with 30 ft swell and indicate that the storm is still a potent force. Other signs indicate, however, that the storm is beginning to dissipate. The decrease in the thickness gradient indicates that the lower tropospheric front is occluded. The 500 mb absolute vorticity (Fig. 23b) decrease indicates a large reduction in relative vorticity from negative vorticity advection and the discontinuance of the jet stream influence (Fig. 23a). Extreme height falls are reflected in the 250 mb flow as the wind field becomes closed, indicating an upward cyclonic development through this level.

Inspection of the satellite imagery for this period (Figs. 24 and 25) valid at 1005 GMT 15 January 1979 shows a fully mature occluded system. The penetration of cold air to the vortex center is evident along with a marked decrease in deep convective activity near the vortex and along the frontal band, except in the northern fringe where the strong cyclonic flow is still producing some low-level convergence

and associated deep convection. The developing low to the south is just visible in the imagery.

By 0000 GMT 17 January 1979, the surface system has filled to 962 mb and the thickness gradient is small (Fig. 26c). At 500 mb (Fig. 26b), the low has combined with a stationary feature to the west to produce a vast area of low heights. Positive vorticity has decreased as the vertical gradients have deteriorated markedly while the system slowly dies. At 250 mb (Fig. 26a), the increased closed circulation indicates vertical stacking through the whole troposphere. These features suggest that the storm has reached the dissipating phase, which marks the termination of the synoptic portion of the analysis.

It is interesting to notice that during the period of lowest central pressure (0000 GMT 15 January 1979), ship reports in the region indicate 40 ft waves, 20 ft swell and 38 kt winds. The dramatic deepening of this and similar storms is not without its consequences. These storms pose significant threats to ships and land facilities within their paths. The intent of the next chapter is to pursue those processes qualitatively described in this chapter by mass and vorticity budget analyses. The budget framework

provides a computational base through which significant aspects of the storm are explored.

V. MASS BUDGET ANALYSIS

A. GENERAL

It is clear from the synoptic discussion (Chapter 4) that the key factors necessary for cyclone development are inherently related to dynamical processes occurring in the lower tropospheric regime. One such vital process is the destabilization of the surface layer. Another includes the horizontal and vertical mass circulation structure, as pressure falls and resultant storm intensity are directly dependent upon the nature and magnitude of the mass flux into and out of the budget volume.

The mass budget portion of this chapter includes a quantitative approach to determine the destabilization and horizontal and vertical mass transport within the budget volume. The stability analysis is based on area-averaged potential temperatures for the layer. For example, the layer labelled 775 mb represents the 850-700 mb layer. The lateral mass transport is also calculated for the layer and is averaged over time periods. Vertical mass transport is inferred from the vertical velocity (ω) fields. Time periods refer to

the 12-h time increment between synoptic times. For example, period 1206 refers to 0000-1200 GMT. Radial distances of 6 and 10 degrees of latitude specify the horizontal budget area and correspond to 360 and 600 n mi radial distances from storm center. These particular radii were chosen after inspection of radial sections depicting the storm's major circulation features. The inner radius (6) incorporates the zone of maximum cyclone circulation associated with the strong two-layer inflow/outflow regime (subsequently addressed). The outer radius (10), in contrast, shows the weaker storm circulation near its periphery.

B. POTENTIAL TEMPERATURE AND STATIC STABILITY ANALYSIS

The steady flow of polar continental air from the Siberian mainland over the warm waters of the western Pacific was described in Chapter 4. Destabilization of the boundary layer in this manner is a critical factor for oceanic cyclogenesis, as demonstrated by Roman (1981) and Sandgathe (1981). The amount of destabilization is contingent upon the latent heat release in the layer and the sensible heat flux from the ocean. These quantities are dependent to a large degree on the air-sea temperature difference, and the magnitude of the lapse rate through the lower troposphere.

Roman (1981) found stability decreases of nearly $2 \text{ K} / 100 \text{ mb}$ fully 12 h before the onset of maximum deepening using a budget volume analysis. Numerical model simulations by Sandgathe (1981) showed a similar trend, with magnitudes roughly half that observed by Roman (1981) for a western Atlantic storm. An analysis of the destabilization of the lower troposphere in this case will be described using the potential temperature vertical-time sections.

Inspection of the time sections of area-averaged potential temperature for radii 6 and 10 (Fig. 27a and b) shows similar interesting features. Notice that potential temperature values in this figure are presented for 12-h synoptic times. Lower tropospheric (1000-750 mb) and upper tropospheric (450-175 mb) potential temperature changes imply warming during the early time periods. In the mid-troposphere (750-450 mb), potential temperature changes little in the early time periods. Of interest is the apparent lack of a well-defined tropopause (indicated by a dense vertical packing of isentropes) during the early time periods. Possible factors accounting for this observation include the impact of jet streak propagation (described in Chapter 4) into the budget volume, or the characteristic

upward slope of the tropopause toward the tropics, or a combination of both. At later time periods, the entire budget volume is seen to cool, with the most significant decrease occurring below 350 mb, as the cyclone takes on familiar extratropical cold-core characteristics. The tropopause becomes well established by 0000 GMT 15 January, which coincides with the movement of the budget volume out of the region of the baroclinic zone and into the colder polar air. Several substantial potential temperature fluctuations exist during the 1800 GMT times (not shown) and are addressed later.

To convert potential temperature changes to static stability features, a procedure similar to that employed by Sandgathe (1981) will be used. He defines the static stability of the layer as directly proportional to the specific volume of the layer and to the change in potential temperature between pressure surfaces ($d\theta/dP$), and inversely proportional to the average potential temperature of the layer. For periods of interest here, the static stability of the 1000-500 mb layer will be explored. The specific volume of the layer is assumed constant with time (variations are less than 3%). The potential temperature fields (Fig. 27) imply

rather uniform average temperature structure for the lower troposphere through time. Thus, the static stability variations are predominantly a function of the change in the lapse rate with time.

The static stability trends for inner and outer radii are shown in Fig. 28a. Destabilization of the layer occurs for both radii until 1200 GMT 14 January. The increase in stability after 1200 GMT 14 January is a reflection of cold advection in the lower troposphere. The marked decrease in stability during the early periods (Fig. 28a) is associated with an increase in the surface layer potential temperature. Thus, surface instability promotes the generation of organized convection in the storm region, and serves to foster the cyclonic circulation tendency. A similar trend was observed by Sandgathe (1981) in his numerical simulations (Fig. 28b). Direct comparison of observed and simulated stability magnitudes is not feasible due to the significant differences in the horizontal scales over which the data was averaged. It can be seen, however, that the trends in the observational data match the simulated data very closely, and show the characteristics of one of the main ingredients that is favorable for oceanic cyclogenesis.

One interesting feature of Fig. 27a deserves special scrutiny. The dramatic fluctuations in potential temperature (8 K) between 1200 GMT 14 January and 0000 GMT 15 January between 800 and 500 mb is remarkable for such a small time interval. In general, the atmosphere requires much longer periods for such large fluctuations. Inspection of 850-500 mb potential temperature fields for both radii for times immediately preceding and subsequent to 1200 GMT shows significant warming evident in the 1800 GMT field. In addition, potential temperature biases of smaller magnitudes were evident at the 1800 and 0600 GMT times on other days (Fig. 27a and b). The nature of these (1800 and 0600 GMT) potential temperature fluctuations suggests a problem with the FGGE data assimilation schemes, and its impact on this study is specifically addressed in Appendix A.

C. HORIZONTAL MASS FLUX

The system horizontal mass transport analysis consists of vertical time sections for radii 6 and 10 (Fig. 29a and b) in terms of g/sec for the 100 mb layer. Flux values are corrected for mean cyclone movement and residual imbalances (see Chapter 3). Time periods refer to the 12-h period between synoptic times. For example, period 1206 refers to 0000-1200 GMT 12 January.

Inspection of Fig. 29a for radius six shows a two-layer regime consisting of strong low-level mass influx associated with surface layer convergence below a layer of mass outflow associated with middle and upper-level divergence. The strength of the mass flow is seen to increase in both regimes as the storm develops, with a distinct inflow maximum near 925 mb and an outflow maximum near 350 mb. The inflow maximum (3.27×10^{13}) at 1318 GMT is roughly twice the outflow maximum (1.56×10^{13}). Although the low-level inflow is intense, it is restricted to a relatively narrow layer. The deeper, though weaker, upper-level outflow causes a net vertically integrated mass loss within the column. The net horizontal mass outflow in the vertical columns (Fig. 29a) is reflected in the surface pressure falls (Fig. 2b) during the developing periods.

The temporal variation in the level of non-divergence (LND) and the associated inflow maxima (Fig. 29a) between 1306 and 1406 GMT indicates vertical growth of the convergent layer as intense cyclogenesis occurs. By 1306 GMT, when closed isobars become evident at the surface, the convergent layer begins to grow as the surface circulation is established. The growth of the convergent layer during

cyclogenesis is consistent with results found by Roman (1981). The radius 6 LND reaches maximum height (at 1406 GMT) soon after the occurrence of the maximum surface layer transport and just before the period of lowest surface pressure (1500 GMT), and then exhibits a gradual reduction with time as the storm begins to dissipate.

Comparable features exist within radius 10 (Fig. 29b) but interesting differences exist. The mass buildup in the outer volume (1318 GMT) shows a greater relative increase, which indicates differential transport between the two radii, since the inner volume increases are incorporated in the outer volume tendency. The differential mass transport can be explained by the earlier influence of the migratory jet streak (discussed in Chapter 4) as it propagates first into the outer budget volume. The decrease in mass transport after 1318 GMT reflects the decrease in jet streak influence as it propagates through the inner volume and dissipates (see Chapter 4). These patterns substantiate the intensity of associated "weather" observed by stations hundreds of n mi from the storm center and clearly illustrate the immense scale of these meteorological events. It should also be noticed that the increase in low-level circulation

during the last few time periods at radius 10 (Fig. 29b) is attributed to the incorporation of the developing circulation to the south (see Chapter 4).

Several interesting features of the development stage of this cyclone can be observed by inspection of the radial-vertical sections of the corrected lateral mass flux. A sequence of four times was chosen (0000 and 1200 GMT 14 January and 0000 and 1200 GMT 15 January) illustrated in Figs. 30 and 31 respectively.

At the outer radii in Fig. 30a, the mass transport is a maximum near radius 11. The LND is relatively constant in height through all radii. A broad region of strong upper level divergence is also evident near the outer radius. Notice the significant change twelve hours later (Fig. 30b). An additional layer of surface convergence near 775 mb approaches the storm center from the outer radii. This feature suggests that a major significant change in the circulation has occurred during the past twelve hours. Normal cyclone development might explain a portion of the increase, but the explosive development indicated during this time from the rapid pressure falls suggests some additional forcing present in the budget volume.

In the subsequent 12-h period (Fig. 31a), the surface transport maximum decreases and moves well inside radius 6. Divergence aloft is well established and the positive transport inside radius 3 between 400-125 mb suggests net subsidence and adiabatic warming near the cyclone core, which arrests at least to some small degree the cold-core formation process. Transport values markedly decrease 12 h later (Fig. 31b) and suggest cyclone dissipation.

These circulation features may be compared with major characteristics of tropical storm intensification (e.g. Holland and Merrill, 1983). Explosive development in both cases appears to be characterized by large circulation and mass transport increases at the outer radii, with subsequent inner radial development after organized transport has moved near the inner region with deep convection. The inner radial development is also largely dependent on the formation of a broad and strong outflow regime in the upper troposphere. As these significant features form, organized convection dominates the inner radii and triggers the rapid pressure falls due to large latent heat inputs into the lower troposphere. Large pressure falls set the stage for increased winds, circulation etc.. The storm rapidly

develops with warming near the central core until the surface system becomes detached from the upper-level ventilation and divergence source. The significant observed difference in the formation processes lies in the expanded radial scale of the extratropical system compared to the mesoscale structure of the tropical system. Otherwise, upper-level ventilation features, inner radius organized deep convection, weak stability of the surface layer and large outer region transports in the early development periods suggest reasonable similarities. The conclusions cited above are only suggestions from the available FGGE fields and will not be explored in detail, as these aspects are not considered a primary objective of this study.

D. VERTICAL MASS TRANSPORT

The storm vertical mass transport analysis consists of vertical time sections of omega fields (Figs. 32, 33 and 34) for radius 6 and 10. Three distinct omega fields are calculated by slightly different methods and the differences are examined. The omega fields discussed below represent the vertical mass transport and necessarily reflect periods of intense horizontal mass transport through continuity (see Chapter 3).

The differences between the three omega fields are shown clearly in Figs. 32, 33 and 34. The budget calculated (QLD) omega fields (Fig. 32) are area-averaged values derived from the lateral transport through mass continuity. The FGGE Level III-b vertical motion estimates (Fig. 33) are derived as point estimates without diabatic internal adjustments. Omega fields calculated at grid points using the kinematic method, which implicitly includes small-scale diabatic effects, are shown in (Fig. 34).

The difference in magnitude and level of the vertical motion maxima between the three vertical motion fields is interesting. The QLD (Fig. 32) and FGGE (Fig. 33) vertical velocity maxima match fairly closely in time of occurrence and magnitude, but differ considerably in level. Compensation for the residual imbalances in the budget calculations (discussed in Chapter 3) are applied layer by layer (highest layers are weighted more) in the QLD omega field derivation. Thus, the QLD omega magnitudes are comparable but the level of the maxima is biased toward the higher layers (Fig. 32).

The kinematic vertical velocities differ both in magnitude and level. This is not surprising considering the values include small-scale diabatic effects. Paegle (1983)

demonstrated similar results and found that the FGGE derived fields were roughly $1/3$ the magnitude of the kinematically derived fields, which is consistent with a comparison of Figs. 33 and 34 (the ratio is closer to $2/3$ here). For the purpose of this study, the kinematic omega fields are considered to best represent the actual vertical motion.

A comparison of the vertical velocity fields with the horizontal mass transport shows consistent features. The vertical velocity maxima (Fig. 34a) correlate well temporally with the surface convergence and upper level divergence maxima (Fig. 29a), and with periods of rapid surface deepening (Fig. 2b). In addition, the more intense vertical motion at radius 6 (Figs. 32, 33 and 34), which is roughly 1.5 times greater than at radius 10, agrees well with the satellite discussion which depicted extreme amounts of deep convection in the inner radius (see Chapter 4).

E. CONCLUSIONS

In summary, stability and QLD mass budget analyses have revealed the following insights:

- Surface stability decreases during the early time periods favor organized convection;
- The stability analysis shows destabilization trends consistent with numerical model simulations (Sandgathe, 1981);

- Evolution of cold core characteristics is evident throughout most of the troposphere after the surface circulation intensifies;
- Maxima in surface layer convergence occur during periods of intense vertical motion and strong upper-level divergence, coincident with observed maximum cyclone deepening rates (Fig. 2b);
- The broad divergent layer aloft contributes to central pressure falls even though the maxima are considerably smaller than the associated surface layer convergent maxima, indicating overall net mass outflow during periods of storm intensification;
- The LND varies according to the strength of the surface convergent layer, and rises during the period of explosive development;
- Vertical velocity fields employing kinematic calculation methods represent well the LND and vertical mass transport which is a vital link in the lifeblood of storm dynamics.
- Vertical-radial cross sections of mass transport during extratropical cyclogenesis suggest similar development characteristics to tropical storm rapid intensification.

The next chapter seeks to explore the circulation tendencies as delineated by the absolute vorticity buildup within the budget volume as the storm evolves. Horizontal and vertical transport, and sources and sinks of absolute vorticity will be explored quantitatively to further delineate storm dynamical features.

VI. VORTICITY BUDGET ANALYSIS

A. GENERAL

The absolute vorticity budget analyses are presented by vertical-time sections and by selected vertical profiles. Time periods refer to the 12-h span between synoptic times. For example, period 1206 refers to 0000-1200 GMT 12 January. In figures not referencing time periods, times refer to the specific time (GMT). The 775 mb layer refers to the layer between the 850 and 700 mb. The sign convention is positive for processes producing vorticity increases in the budget volume (sources), and negative for vorticity decreases (sinks).

The main feature of this section includes a discussion of the absolute vorticity time tendency as a measure of storm development. Specifically, an investigation is conducted into the role of horizontal and vertical absolute vorticity transport, advection, generation and dissipation in storm dynamics. Horizontal transport terms are separated into mean and eddy mode components to gain better insight into their specific contributions toward storm development.

Vertical transport terms reflect vertical divergence and advection from omega estimates using the kinematic method. Referral to Section B of Table V is recommended as specific budget terms are identified and discussed.

B. TIME SECTIONS , TIME TENDENCIES AND SELECTED PROFILES

The dramatic buildup of absolute vorticity in the budget volume at both radii over the 2-day span of intense development is illustrated in Fig. 35. At 0000 GMT 13 January (1300 GMT), the relative cyclonic vorticity in the inner volume through the 600 mb level is not much different from the coriolis parameter (7.82×10^{-5}). Notice the presence of anticyclonic relative vorticity aloft, which is associated with the weak and dissipating upper level ridge. The dramatic increase in absolute vorticity by 0000 GMT 15 January in the inner radius occurs from two sources. The rapid movement to the northeast over the period has resulted in a larger value of planetary vorticity ($f = 11.56 \times 10^{-5}$), while the increased storm circulation accounts for the additional buildup. Although the surface circulation is strong, the maximum absolute vorticity exists in the middle troposphere. Similar changes occur at radius 10, although the magnitude of the absolute vorticity increase is smaller,

and there is a uniform increase through the troposphere below the jet core level. Specific factors contributing to the vorticity changes at the different vertical levels will be discussed as the specific budget terms are analyzed.

A different perspective of the absolute vorticity buildup in the budget volume is presented in Fig. 36. Here, vertical time sections of vorticity for both radii illustrate several key features. At radius 6 (Fig. 36a), a vorticity minimum can be seen at 200 mb during the early period. The increase with time at lower levels is a reflection of the nascent cyclone vertical structure which is composed of anticyclonic vorticity aloft over the low-level developing system. After 1212 GMT, absolute vorticity increases throughout the whole troposphere until 1500 GMT. Two significant features are evident during these times. A large buildup occurs in the upper troposphere (vicinity 225 mb) after 1300 GMT, which causes a temporary reduction in the vertical vorticity gradient. A distinct lower tropospheric maximum is evident at 1500 GMT, which occurs just after the period of intense circulation increase, and is substantiated by the mass transport maxima shown in the mass budget analysis (Fig. 29a) and the associated central

surface pressure falls illustrated in Fig. 2a of the synoptic discussion. This large maximum in vorticity is coincident with the period of lowest central pressure and maximum surface layer circulation. Vorticity values are seen to decrease in the middle and lower troposphere for 24 h after 1500 GMT, but at a significantly slower rate than the buildup. Values increase again through the whole troposphere after 1600 GMT due to the inclusion of the developing system to the south.

Several important differences exist at radius 10 (Fig. 36b). Vorticity values increase at a slower rate and at later times than in the inner volume. This result indicates that although vorticity values increase in both volumes during the development stage, the outer volume experiences a less significant increase due to the greater spatial extent and relatively smaller vorticity.

Absolute vorticity time tendency, which is the first term in the vorticity budget equation (see Table V), is presented in Fig. 37. This display is a time derivative of the fields depicted in Fig. 36. Recall that time periods, when used in subsequent figures, refer to the 12-h time interval between synoptic times.

A large increase in the vorticity tendency in the inner volume occurs in the upper levels from 1218-1318 GMT. Vorticity increases at a constant rate in the surface layer during the development stage. The general decrease in tendency values through the whole troposphere after 1506 GMT is consistent with the onset of the occlusion phase and storm dissipation. It is interesting that a vorticity tendency minimum occurs near 450 mb during a period of large surface pressure falls (Fig. 2b) and maximum mass transport (Fig. 29). No correlation to synoptic causes for this tendency minimum is apparent from detailed inspection of the 500 mb height and vorticity fields (Figs. 4b, 7b, 10b). One interpretation is that a subsynoptic scale system in the wind fields affects the vorticity values at these levels and times. An alternative cause could be linked to insufficient data input into the 1312 or 1400 GMT analyses.

Similar significant features exist at radius 10 (Fig. 37b). The nature of the buildup of absolute vorticity suggests inherently similar mechanisms are responsible for the absolute vorticity buildup between inner and outer volumes. Mechanisms such as the jet core influence, mid-tropospheric self-amplification, and horizontal and vertical

transport are possibilities explored in the following sections.

C. LATERAL TRANSPORT

The lateral transport of absolute vorticity is one of the three most significant forcing terms in the budget equation (Table V). Transport into the budget volume arises from the mean convergent flow (mean mode) and from asymmetries in the cyclonic flow (eddy mode).

A typical view of the lateral vorticity transport occurring during storm development is presented in Fig. 38. The curves are valid during the maximum development period at radius six. The mean mode and total lateral transport curves are similar and show similar trends. The mean mode is seen to dominate the total transport at levels below 800 mb. In the upper levels, the total lateral transport is small, but is the residual between two strong oppositely contributing processes. These features constitute significant differences from those observed by Conant (1982) in the President's Day storm, where he observed that the total and eddy mode lateral transport curves were the more strongly correlated. Although the curves presented in that study represented an earlier phase in the storm development, the

general features indicate that different mechanisms serve to increase inner volume vorticity levels within each storm budget volume. A look at the mean and eddy mode lateral transport vertical-time sections gives insights into processes responsible for these differences.

Another interesting feature is the presence of a measurable eddy mode contribution in the lower troposphere, which is an indication that processes other than mean convergence are acting to increase the vorticity and storm circulation within the six degree volume. These results should be expected, since processes such as intense convection in preferred quadrants of the storm, frontal asymmetries and elliptical vortex structure may cause asymmetric flow about and into the cyclone. Thus, some eddy mode contribution is evident through the whole troposphere. Mean and eddy mode contributions to the total vorticity lateral transport are discussed below.

The total lateral vorticity transport time sections for the inner and outer budget volumes are presented in Fig. 39. In the inner volume (Fig. 39a), inward transport exists below 775 mb through all time periods, with alternating inward and outward transport evident in the upper

troposphere (near 350 mb). Notice the mid-tropospheric (600 mb) outward transport (after 1506 GMT) as broad divergence is established. The outward transport maximum at 225 mb suggests strong divergence aloft as the jet stream dominates the upper troposphere flow. The surface layer regime is particularly noteworthy in that especially deep inward vorticity transport occurs during the deepening phase (1318-1506 GMT) through 450 mb and contains a maximum ($19.2 \times 10^{-10}/\text{sec}^2$) at 925 mb. This signature is entirely different from that observed by Conant (1982) in the President's Day storm. He showed a maximum at 220 mb with relatively weak surface transport. The emphasis on the level of maximum horizontal lateral transport serves to focus on the differences between the underlying processes responsible for vorticity increases within the budgets of both systems. In this case, the lateral transport surface maximum occurs in temporal coincidence with the largest central pressure falls and maximum mass transport, as discussed in previous chapters.

The total lateral transport at radius 10 (Fig. 39b) exhibits similar inward transport in the surface layer although the magnitude is considerably less and the maximum

occurs a time period earlier. Inward vorticity transport is evident through the rest of the troposphere (except above 450 mb after 1606 GMT), with a secondary maximum observed between 450 and 175 mb during the 1218-1318 GMT periods. The time and level of occurrence of this maximum strongly suggests vorticity import from jet streak interaction. Subsequent low-level inward transport occurs from circulation increases in response to this upper-level forcing. The earlier occurrence of both upper and lower-level maxima in the outer volume suggests earlier forcing from jet streak interaction as it enters the outer volume first and subsequently migrates toward the inner volume. The increase in the surface layer transport at 1618 GMT is again due to the developing system to the south.

D. MEAN MCDE LATERAL TRANSPORT

As described in Chapter 3 (Table V), the absolute vorticity transport can be partitioned into mean and eddy modes. The purpose of this partitioning serves to isolate contributions by the mean flow (mean cyclone convergence and divergence), and the perturbation flow (the covariance of vorticity and normal wind component deviations).

Specifically, the mean cyclonic low-level inflow and upper-level outflow of vorticity is represented by the mean mode and reflects necessarily the convergent/divergent nature of the lower/upper layers.

At radius six (Fig. 40a), the strong dual-centered transport maximum, the upper-level outflow maxima and the level of transition between inward and outward transport agree well both temporally and spatially with the mass budget transport features discussed in Chapter 5. Periods of maximum surface cyclone deepening coincide directly with the vorticity transport maxima discussed above. Differences in mean mode transport between the President's Day storm and the present case arise due to the significantly weaker surface-layer lateral vorticity transport in the President's Day storm, whereas the upper layer transports are nearly the same. Thus, the main difference in the growth and vitality in this storm is the significantly higher mean flow transport of vorticity in the lower layers.

At radius 10 (Fig. 40b), absolute vorticity lateral transport values are relatively weaker than at radius 6. A single inward transport maximum in the surface layer and a coincident upper-level outward maximum are evident. These

maxima occur earlier, again, in response to earlier dynamic forcing in the outer volume by the upper-level eddy structure changes (subsequently addressed). The effects of the new low to the south are again seen after 1518 GMT.

E. EDDY MODE LATERAL TRANSPORT

The eddy mode absolute vorticity lateral transport gives insight into the upper level vorticity increases which ultimately affect the low level circulation tendencies. As discussed above, the eddy mode component represents the horizontal transport due to asymmetries in the cyclonic flow induced by wind field correlated vorticity deviations.

Inspection of the eddy mode absolute vorticity transport for radius 6 (Fig. 41a) shows considerable vorticity import in the layer between 750 and 125 mb after 1206 GMT. Within this broad area of positive lateral vorticity transport are two significant time periods. Between 1206-1306 GMT, a maximum of vorticity transport is seen to exist in the 450-275 mb layer. Inspection of the 300 and 400 mb vorticity and winds for 1200 and 1212 GMT shows weak PVA into the budget volume, and this is substantiated by the coincident maximum in the calculated advection (Fig. 43a) discussed subsequently. These facts suggest vorticity import in the form

of the short wave that becomes established over southern Japan during this time frame (discussed earlier in the synoptic discussion, Fig. 4b). The effect of this perturbation diminishes with time as the cyclone accelerates to the northeast away from the slower moving upper-level trough after 1300 GMT, and thus, the eddy mode transport also diminishes. Vorticity increases are again evident after 1306 GMT when the jet streak has become well established in the budget volume (Fig. 7a). The influence of the jet streak continues until 1518 GMT when the jet core becomes detached from the budget volume as the surface center migrates steadily northward.

Significant eddy mode contributions are restricted to the upper levels, and are only roughly 1/2 those observed by Conant (1982) in the President's Day storm. This is an extremely valuable result, as Conant showed that the migratory short wave played a major role in that storm development. In this study, the migratory short wave is shown to be of minimal influence, and thus vorticity increases in the upper levels occur primarily from cyclonic shear vorticity input into the budget volume as the jet core becomes established. While the eddy mode contributes

considerably to the initial storm development, this effect is not nearly as dominant during the explosive stages as in the President's Day storm. In this case then, it is logical to conclude that explosive development occurs due to upper-level jet forcing acting in concert with the surface development along the baroclinic zone. The secondary eddy mode maximum near 925 mb at 1418 GMT is presumed to be due to asymmetries in the mean flow in specific quadrants of the storm circulation.

Similar features exist at radius 10 (Fig. 41b). As in the inner volume, significant contributions occur at the jet core level with maxima of similar magnitude occurring at coincident times. A weak maximum exists from 1406-1506 GMT in the surface layer, and as in the 6-degree volume, represents small asymmetries in the mean cyclonic flow.

Alternatively, the lateral transport may be expressed in terms of lateral divergence and advection components through the use of vector identities (see Table V). These terms provide a more traditional view directly in terms of the vorticity equation. The divergence component of the partitioned lateral vorticity transport (Fig. 42a), is composed of a two-layer regime with positive vorticity production due

to convergence in the surface layers and negative vorticity production with divergence aloft. These features match closely the associated mass transport features discussed in Chapter 5. The temporal and spatial occurrence of the inflow and outflow maxima agree well with similar features of the mean mode discussion, and with the general circulation increases and maximum pressure falls.

The most interesting comparison occurs between the eddy mode and horizontal advection transports (Figs. 41a and b and 43a and b). The upper tropospheric values match well both temporally and spatially, as well as in magnitude. However, the advection term in the lower troposphere shows a substantial negative vorticity advection (NVA) into the volume below 775 mb, which is quite different from the negative and positive eddy vorticity transports. In-depth examination of the vorticity and wind fields in the inner volume during a period of maximum development shows an asymmetric east-west oriented vorticity field coupled to a strong cyclonic inflow pattern, which causes a net advection of smaller vorticity values into the volume in the northeast and southwest quadrants. This net NVA is further enhanced by the 40-kt translation speed of the surface center to the

northeast during this period. The change to a westerly, more zonal wind component with height accounts for the sign reversal in the vorticity values above 775 mb. Notice that the addition of the advection and divergence terms is very close to the sum of the mean and eddy mode lateral transports. These results serve to verify the integrity of the transport calculations.

In summary, the total horizontal absolute vorticity transport has been shown to be composed of a mean mode representing contributions from the mean mass circulation, and an eddy mode representing contributions from asymmetries in the flow from advection and jet core sources. The mean mode transport was shown to be very similar to the total transport through all levels, while the eddy mode transport was shown to be significant only above 500 mb. The relatively smaller magnitude of the eddy mode transport maxima compared to that observed in the President's Day storm suggests this term plays a less significant role in the storm evolution.

F. VERTICAL REDISTRIBUTION

This section investigates the role of vertical vorticity transport from the upper and lower layers into the middle

troposphere (as discussed earlier in connection with Fig. 34). In this case the diffluent nature of the upward evolving trough will be explained in terms of this mid-level vorticity increase. The concentration of vorticity in the mid-troposphere serves to increase mid-level circulation, increase thermal advection, and amplify the trough. Vertical transport of vorticity was calculated using the kinematic ω fields (Chapter 5).

The effect of the vertical transport in the vorticity budget is given by the divergence of the vertical transport (Fig. 44a and b.). This term results from the vertical derivative of the transport between levels and represents the redistribution of vorticity upward through the troposphere. Notice the two-layer regime with strong transport from the surface layer into the middle and upper troposphere. The vertical transport of vorticity is a consequence of upper-level divergence which induces lower-level circulation and vertical motion increases throughout the low and middle troposphere. The maxima in both upper and lower regimes are temporally coincident with periods of maximum vertical motion (see Chapter 5). Values in the outer radius are considerably smaller which is consistent with the less intense vertical motions.

The divergent component (Fig. 45a) is the main contributor to vertical vorticity redistribution. This term is simply the opposite of the lateral divergence term (Fig. 42a), but differs slightly due to the kinematic vertical motion estimates. There is a decrease of vorticity below the maximum in the vertical motion, and a gain above this maximum. The reversal in sign from the lateral divergence term (Fig. 42) is consistent from continuity, and close agreement between the temporal and spatial magnitudes shows consistency. Similar features exist at radius 10, although the magnitudes are considerably less as expected.

The vertical advection portion (Fig. 46a) plays a relatively minor role in the budget. Positive vertical advection is seen to occur between 775 mb and 350 mb from 1318-1506 GMT. Accumulated values of surface layer vorticity are advected by the vertical motion during these times. Positive values below and negative values above 450 mb contribute to the vorticity buildup in the middle troposphere illustrated in Fig. 35. The relatively minor contribution of vertical advection to the budget results is consistent with results found by Conant (1982).

In summary, the vertical transport redistributes the large vorticity buildup in the lower troposphere into the mid and upper troposphere. The divergent component was the major contributor, as the advection term was relatively weak throughout the budget volume. Processes at radius 10 are similar with considerably lower magnitudes.

G. SOURCES AND SINKS

Sources of vorticity occur from the divergence and tilting terms, while frictional dissipation is a vorticity sink. Generation of vorticity by horizontal divergence is the fluid analog of the change in angular velocity of an object when it changes its moment of inertia while conserving angular momentum. If horizontal divergence occurs and circulation is conserved, the area enclosed by a fluid parcel will increase and the average vorticity of the parcel must decrease. Thus, the pattern of low-level convergence and upper-level divergence in a developing storm means there is a source of vorticity at low levels and a sink in the upper troposphere (Fig. 42a and b). This term is mathematically the same as that which appears in the lateral transport partition (see Section B, Table V).

An important feature to notice is the relatively large magnitude of the maxima in both regimes compared to the total lateral transport. These patterns suggest that the divergence term plays the dominant role in the budget. In the lower troposphere, convergence overwhelms all other processes, as is expected from a scale analysis of the general vorticity equation.

The tilting term (Fig. 47a and b) arises from vertical vorticity components generated by the tilting of horizontally oriented vorticity elements by a non-uniform vertical motion field. Strong vertical shear and a horizontally varying omega field are prerequisites for contributions from this source. It is apparent (from Fig. 47a and b) that the products of vertical shear and the change in the vertical motion fields in the horizontal are small compared to lateral and vertical transports.

Frictional dissipation (Fig. 48) is assumed to occur only in the surface boundary layer and is parameterized using a stability dependent scheme (Johnson and Downey, 1976). The calculated values were about 1.5 times greater than those observed by Ccnant (1982), as is expected from the larger intensity of the disturbance studied here. The

maximum at 1506 GMT has a magnitude very close to the value of the low-level maximum in the total lateral transport (Fig. 39a). These results suggest that frictional effects assume a prominent role in the dissipation of vorticity in the surface layer. Values in the outer volume (Fig. 48b) suggest minimal frictional influences on the vorticity averaged over a larger region.

In summary, the divergence term was a major factor in the overall budget as a source of cyclonic vorticity in the lower troposphere and a sink aloft. The friction term was an important sink of vorticity in the surface layer, whereas the tilting term had no significant effect on the budget.

H. RESIDUALS

The residual in the vorticity budget contains the effects of the omitted processes plus the accumulated errors in the calculation of the resolved terms. Inaccuracies in the vertical motion and horizontal wind fields contribute to the physical residual components, whereas spatial and temporal finite differencing and grid-point interpolation inaccuracies are causes for computational errors. A positive vorticity residual indicates an apparent vorticity source in which the observed vorticity increases at a point are larger than is estimated by the computed terms.

Residuals for the inner volume (Fig. 49a) during the development period indicate generally small values in the middle and upper troposphere, while large vorticity excesses are evident at 350 mb (1306 GMT) and at 275 mb (1406 GMT). Since these maxima occur during periods of rapid development and maximum vertical motion, it seems likely that improper representation of the intense mesoscale convection process is responsible. That is, inaccuracies in the vertical motion fields and therefore the vertical transport could lead to underestimation of the vertical redistribution. The pattern in Fig. 49a is consistent with vorticity transport by convection, which has been shown to be important in tropical circulations (Shapiro and Stevens, 1982). In addition, residuals could also be expected to be greater than normal in areas of significant jet streak activity where the horizontal wind fields are generally the most inaccurate. The large negative residual in the outer volume (Fig. 49b) is a likely result of this effect. Although computational residuals are difficult to isolate in an analysis such as conducted here, it appears that contributions from this source are relatively unimportant given the small residual values through most of the troposphere.

I. CONCLUSIONS

In summary, the increase of absolute vorticity in the budget volume during the development stage was shown to occur from a complicated interaction of processes. The period of surface layer circulation organization associated with incipient development is distinctly different from the period of explosive development in which the circulation increases throughout the troposphere.

During the incipient stage (period 1206-1318), the lower troposphere circulation increases were shown to occur primarily from the source divergence term, as the storm organized along the baroclinic zone. Lateral transport increased as the circulation developed and contributed to small net vorticity increases since the frictional dissipation was also enhanced.

Mid-troposphere vorticity values increased in the earliest period due to weak lateral transport in the form of PVA from the short wave established over Japan (discussed in detail in earlier sections). This mid-level vorticity import acted to enhance the low-level organization in the earliest stages. At later times prior to 1318 GMT, the divergence of the vertical transport was seen to account for

a significant portion of the mid-level vorticity increases. An increase in the deep divergence layer above the LND served to offset a portion of the mid-level increases.

In the upper troposphere, vorticity values increased as the jet core propagated into the budget volume. Additional increases of smaller magnitudes were evident from vertical redistribution from the surface layer. These two processes combined to more than offset negative vorticity due to the increased divergence. Thus, upper level forcing was available for surface development.

The most significant changes to account for the explosive development after 1318 GMT occurred in the upper troposphere. The small positive lateral transport was a balance between the mean mode (divergence) and eddy mode (advection) contributions. Large amounts of cyclonic shear vorticity were advected into the budget volume after 1306 GMT as the jet streak migrated into the budget volume. The corresponding divergence increases occurred 12 h later, which served to promote the explosive low-level development. The maximum divergence established a time period later served to ventilate the system and induce the maximum mass outflow aloft, increasing the surface circulation, and promoting the explosive development.

Mid-troposphere vorticity increases after 1318 GMT resulted primarily from the divergence of the vertical transport and the upward development of the mid-level diffluent trough from thermal advection. The satellite sequence in Chapter 4 indicates that convection becomes intense and widespread during the period due to vertical stretching in the mid-troposphere induced by the increased upper-level divergence. Vertical stretching acts to cool the middle troposphere and destabilize the vertical columns.

In the lower troposphere, intense circulation increases resulted from the induced upper-level forcing associated with the jet streak movement into the budget volume. The net vorticity increases results from the excess of the lateral transport over the frictional dissipation. Although the frictional effects increased at about the same rate and to the same magnitude as the lateral transport, there was a lag of 12 h. When the upper level forcing and ventilation decreased as the surface center was removed from the jet influence, the system dissipated after 1506 GMT.

VII. CONCLUSIONS AND RECOMMENDATIONS

A synoptic investigation was conducted of a Western Pacific case of extratropical explosive cyclogenesis during 12-17 January 1979. Storm related mass and vorticity budgets were computed for the cyclone using the ECMWF FGGE analyses. Overall storm development features were examined and discussed.

The following significant results were developed:

- Maximum circulation increases due to rapid pressure falls match well temporally and spatially to maxima in the surface layer inward mass transport (convergence) and upper-level outward transport (divergence).
- PVA in the mid-troposphere in the form of short wave interaction, in combination with thermal advection effects, enhances the organization of the low-level circulation in the initial stages of development;
- The initial short wave interaction decreases after the initial period while surface development continues. Explosive development occurs coincidentally with the migration of a strong jet streak into the budget volume, which provides the necessary upper-level forcing from divergence and shear vorticity advection. The lack of an upper-level migratory short wave evident during explosive development confirms Petterssen type-A development;
- The stability analysis reveals trends consistent with numerical simulations (Sandgathe, 1981). Stability decreases rapidly during surface development as cold air was drawn over the warm sea surface. Stability values increased after maximum storm development, as cold air advection dominated the lower troposphere.
- Mass transport radial cross sections suggest explosive development characteristics similar to those observed in tropical storm intensification with the following similarities: 1. low static stability in the surface layer, 2. the availability of an oceanic heat source, 3. strong outflow (divergence) aloft, and 4. strong convection near the inner radii;

- The FGGE data set was found to be less than optimum for supporting 6-h QLD budget analyses. The 0600 and 1800 GMT time periods contain spurious potential temperature biases affecting all of the budget calculations. The problem also affects both initialized and uninitialized fields which suggests inaccurate analysis inputs to the model first guess.

Recommendations for further research include:

- The O'Brien correction scheme applied to the horizontal mass transport should be examined to establish a more optimum representation of the vertical motion fields;
- Further efforts should be made to fully assess the impact of the FGGE 0600 and 1800 GMT data problems and their effects on represented fields in the FGGE data set.
- Energy diagnostic budget calculations should be completed on this cyclone to isolate the contribution of thermal advection, sensible heat and latent heat in the explosive development. Correct parameterization of these inputs could serve as a basis for further comparisons between explosive extratropical and tropical storm formation.

Accurate and reliable forecasts of maritime explosive cyclogenesis will remain a difficult problem until observational networks are improved, latent and sensible heat flux inputs to storm dynamics are better parameterized, and vertical and horizontal model resolutions are improved.

APPENDIX A

FGGE DATA EIAS CHARACTERISTICS

The following information is presented to document the 6-h FGGE data problem encountered in this study. As indicated in Chapter 5, a significant high potential temperature bias was observed in the 850-500 mb layer at 1800 GMT 14 January. Several additional fluctuations were observed to occur at 0600 and 1800 GMT on other days. The nature of these temperature biases radically affected the budget calculations and precluded the planned use of a 6-h interval format. The nature of the effects is shown in Figs. 50 and 51. The top portion of Fig. 50 is a 6-h representation of the vorticity time tendency term at radius six, whereas the bottom field is the inner volume budget residual. The significant 6-h oscillations in both fields are indicative of the difficulty encountered using QLD budget techniques on this particular FGGE data set.

An even more striking example of the complexity of the 6-h data problem is shown in the inner volume stability trace (Fig. 51). Notice the oscillation between maxima and minima indicating the alternate warming and cooling

tendencies in the 6-h fields. It is obvious that a synoptic time scale interpretation of this figure is virtually impossible. The 1300-1500 GMT period is especially interesting. The 0600 and 1800 GMT stability values are markedly larger than at 0000 and 1200 GMT. The increased stability during these times occurs from warm biases in the mid-level potential temperatures, as shown in Fig. 27a and b.

To determine possible causes for this 6-h data problem, specific mid-tropospheric observational data available as input to the FGGE analysis scheme at 1418 GMT was studied. The observations consisted solely of satellite input (microwave and infrared wavelengths). Close scrutiny of the satellite input in comparison with the FGGE gridpoint estimates revealed interesting discrepancies. The final FGGE potential temperature analysis was 5-7 K higher than the associated satellite data in the southwest quadrant of the budget volume. In all other regions the soundings and the FGGE fields matched very closely. In addition, potential temperature biases of smaller magnitudes were evident at the 1800 GMT time period on other days (Fig. 27).

Further insight is gained by an inspection of the uninitialized height fields (through the thickness analyses in

Figs. 16c, 19c and 22c). These fields also show fluctuations of the same scale occurring at the 1800 GMT time frame, as this thickness field departs markedly from the preceding and subsequent analyses. It is obvious that the 6-h data problem affects both initialized (potential temperature) and uninitialized (height) fields. The evidence presented above suggests that a problem existed in the analyzed potential temperature fields used in the first guess, and that the nature of the problem was not identified during the FGGE data post-processing evaluations.

Further support of these conclusions is presented by Paegle (1983), who summarized features of the FGGE data set in tropical regions. Lower tropospheric temperature biases on the order of 2-3 degrees were found for some time periods, which were presumably from the lack of conventional data input at the 1800 GMT times. In addition, the ECMWF forecast model was shown to be insensitive to diurnal temperature changes over land. To what degree this is evident over oceanic areas is still uncertain.

In summary, it is believed that the spurious warming at 1800 GMT between 850 and 500 mb is due to a problem with the FGGE analysis scheme rather than a lack of quality

observations. The impact of this assessment on the results of this thesis cannot be fully ascertained from the preliminary observations discussed here. Detailed investigation into specific analysis fields used in the first guess must be done level by level to fully assess the impact of this 6-h data problem.

APPENDIX B

TABLES

TABLE I
Availability of FGGE Data
(From Bengsston, 1982)

	Z	U	V	T	W	RH
10mb	x	x	x	x	x	
20mb	x	x	x	x	x	
30mb	x	x	x	x	x	
50mb	x	x	x	x	x	
70mb	x	x	x	x	x	
100mb	x	x	x	x	x	
150mb	x	x	x	x	x	
200mb	x	x	x	x	x	
250mb	x	x	x	x	x	
300mb	x	x	x	x	x	x
400mb	x	x	x	x	x	x
500mb	x	x	x	x	x	x
700mb	x	x	x	x	x	x
850mb	x	x	x	x	x	x
1000mb	x	x	x	x	x	x

TABLE II
 Listing of Analyses and Prognoses Utilized
 (FGGE=1,NMC=2,FNOC=3)

<u>LEVEL</u>	<u>TYPE</u>	<u>ANAL/PROG</u>	<u>ORIGIN</u>
sea-level	pressure	anal	1,2,3
sea-level	pressure	36-h prog	2,3
sea-surface	temperature	anal	3
500-mb	heights	anal	1,2,3

TABLE III

Generalized QLD Budget Equation in Isobaric Coordinates

(After Wash, 1978)

$$F = \int_{1000 \text{ mb}}^{100 \text{ mb}} \int_0^\beta \int_0^{2\pi} \frac{1}{g} f r^2 \sin\beta \, d\alpha d\beta \, (-dp)$$

where F is the volume integral of the desired budget property f.

The budget equation is

$$\frac{\delta F}{\delta t} = LT(f) + VT(f) + S(f)$$

where the lateral transport is

$$LT(f) = \int_{1000 \text{ mb}}^{100 \text{ mb}} \int_0^{2\pi} \frac{1}{g} (\underline{U-W})_\beta f r \sin\beta \, d\alpha (-dp) \Big|_\beta$$

and the vertical redistribution is

$$VT(f) = \int_{1000 \text{ mb}}^{100 \text{ mb}} \int_0^\beta \int_0^{2\pi} \frac{1}{g} (\omega f) r^2 \sin\beta \, d\alpha d\beta \, (-dp) .$$

The source/sink term is

$$S(f) = \int_{1000 \text{ mb}}^{100 \text{ mb}} \int_0^\beta \int_0^{2\pi} \frac{1}{g} \frac{df}{dt} r^2 \sin\beta \, d\alpha d\beta \, (-dp) .$$

TABLE IV
QLD Mass Budget Equations in Isobaric Coordinates
(After Wash, 1978)

The Definition

$$M = \int_{V_p} \frac{1}{g} r^2 \sin\beta \, d\alpha d\beta dp$$

where $f = 1$.

The Budget Equation

$$\frac{dM}{dt} = LT + VT ,$$

where

Lateral Transport

$$LT = - \int_{\eta_B}^{\eta_T} \int_0^{2\pi} \frac{1}{g} (U-W)_\beta \, r \sin\beta_B \, d\alpha dp \Big|_{\beta_B}$$

Vertical Transport

$$VT = \int_0^{\beta_B} \int_0^{2\pi} \frac{1}{g} (\omega - \omega_B) \, r^2 \sin\beta \, d\alpha d\beta \Big|_p$$

where

$$\omega = \frac{dp}{dt} , \quad \omega_B = \frac{dp_B}{dt} .$$

TABLE V

QLE Circulation Budget Equations in Isobaric Coordinates

(After Wash, 1978)

Section A

$$C_a = \int_{1000 \text{ mb}}^{100 \text{ mb}} \int_0^\beta \int_0^{2\pi} \frac{1}{g} \zeta_a r^2 \sin\beta \, d\alpha d\beta \, (-dp)$$

where C_a is the absolute circulation and ζ_a is absolute vorticity.

The budget equation is

$$\frac{\delta C_a}{\delta t} = LT(\zeta_a) + DVT(\zeta_a) + S(\zeta_a)$$

where the lateral transport is

$$LT(\zeta_a) = \int_{1000 \text{ mb}}^{100 \text{ mb}} \int_0^\beta \int_0^{2\pi} \frac{1}{g} (\tilde{U} - \tilde{W})_\beta \zeta_a r \sin\beta \, d\alpha (-dp) \Big|_\beta$$

and the divergence of the vertical transport is

$$DVT(\zeta_a) = \int_0^\beta \int_0^{2\pi} \frac{1}{g} \frac{\partial}{\partial p} (\omega \zeta_a) r^2 \sin\beta \, d\alpha d\beta .$$

The source/sink term is

$$S(\zeta_a) = \int_{1000 \text{ mb}}^{100 \text{ mb}} \int_0^\beta \int_0^{2\pi} \frac{1}{g} \frac{d\zeta_a}{dt} r^2 \sin\beta \, d\alpha d\beta (-dp) .$$

TABLE V (Cont.)

Section B

The partitioned form of the vorticity budget equation is

$$\frac{\delta(\zeta_a)}{\partial t} = + \text{LT}(\zeta_a) + \text{DVT}(\zeta_a) + \text{S}(\zeta_a)$$

<div style="display: flex; justify-content: space-between; width: 100%;"> mean mode eddy mode </div>		<div style="display: flex; justify-content: space-between; width: 100%;"> vertical divergence vertical advection </div>		<div style="display: flex; justify-content: space-between; width: 100%;"> divergence term tilting term frictional dissipation </div>		
horizontal divergence	horizontal advection					

The above partitions make use of Stokes' theorem

$$\oint \zeta_a \tilde{U} \cdot \tilde{m} d\ell = \iint_A \nabla \cdot \zeta_a \tilde{U} dA ,$$

and the division of total flux ($\tilde{U} \zeta_a$) into divergent and advective components,

$$\nabla \cdot \zeta_a \tilde{U} = \zeta_a (\nabla \cdot \tilde{U}) + \tilde{U} \cdot \nabla \zeta_a .$$

TABLE VI
Mean and Eddy Mode Transport Equations
(After Conant, 1982)

$$EM(\zeta_a) = \int_{1000 \text{ mb}}^{100 \text{ mb}} \int_0^{2\pi} \frac{1}{g} \overline{\zeta_a^* (\tilde{U}-\tilde{W})_\beta^*}^\alpha r \sin\beta \, d\alpha (-dp)|_\beta$$

$$MM(\zeta_a) = \int_{1000 \text{ mb}}^{100 \text{ mb}} \int_0^{2\pi} \frac{1}{g} \overline{\zeta_a^\alpha (\tilde{U}-\tilde{W})_\beta^\alpha} r \sin\beta \, d\alpha (-dp)|_\beta$$

$$EM(g_a) = \int_{1000 \text{ mb}}^{100 \text{ mb}} \int_0^{2\pi} \frac{1}{g} \overline{g_a^* (\tilde{U}-\tilde{W})_\beta^*}^\alpha r \sin\beta \, d\alpha (-dp)|_\beta$$

$$MM(g_a) = \int_{1000 \text{ mb}}^{100 \text{ mb}} \int_0^{2\pi} \frac{1}{g} \overline{g_a^\alpha (\tilde{U}-\tilde{W})_\beta^\alpha} r \sin\beta \, d\alpha (-dp)|_\beta$$

EM is the eddy mode and MM is the mean mode.

Note that $(\overline{\quad})^\alpha = \frac{1}{2\pi} \int_0^{2\pi} (\quad) \, d\alpha$

and $(\quad)^* = (\quad) - (\overline{\quad})^\alpha$ is the deviation of the property from its mean around a lateral boundary.

APPENDIX C

FIGURES

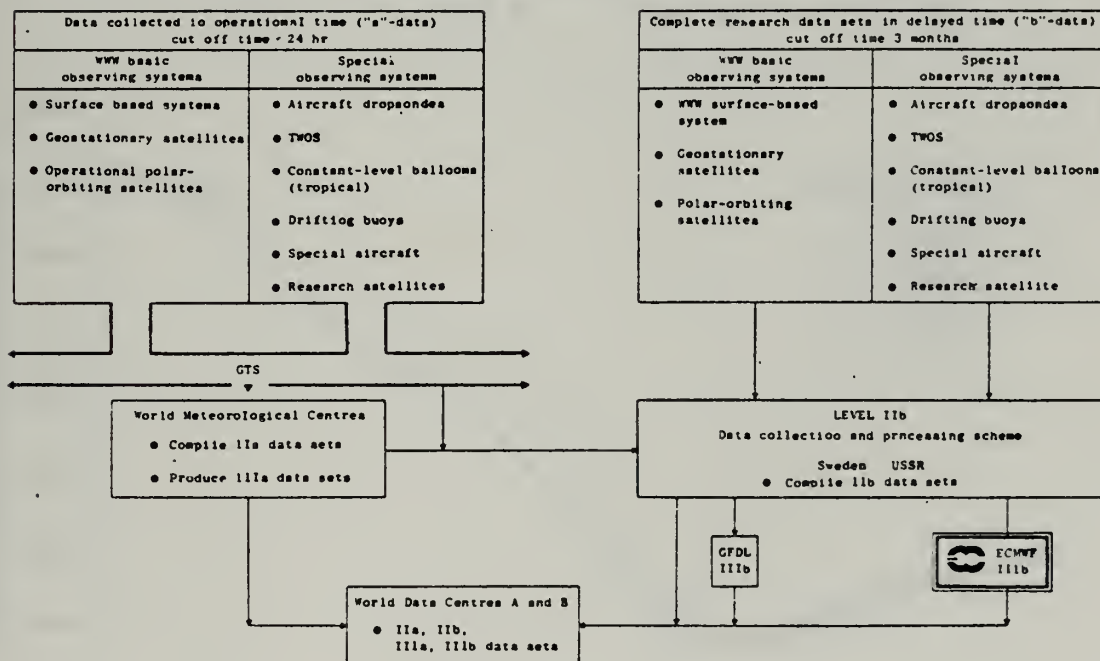


Figure 1. The Overall Data Management During FGGE (From Bengsston, 1982).

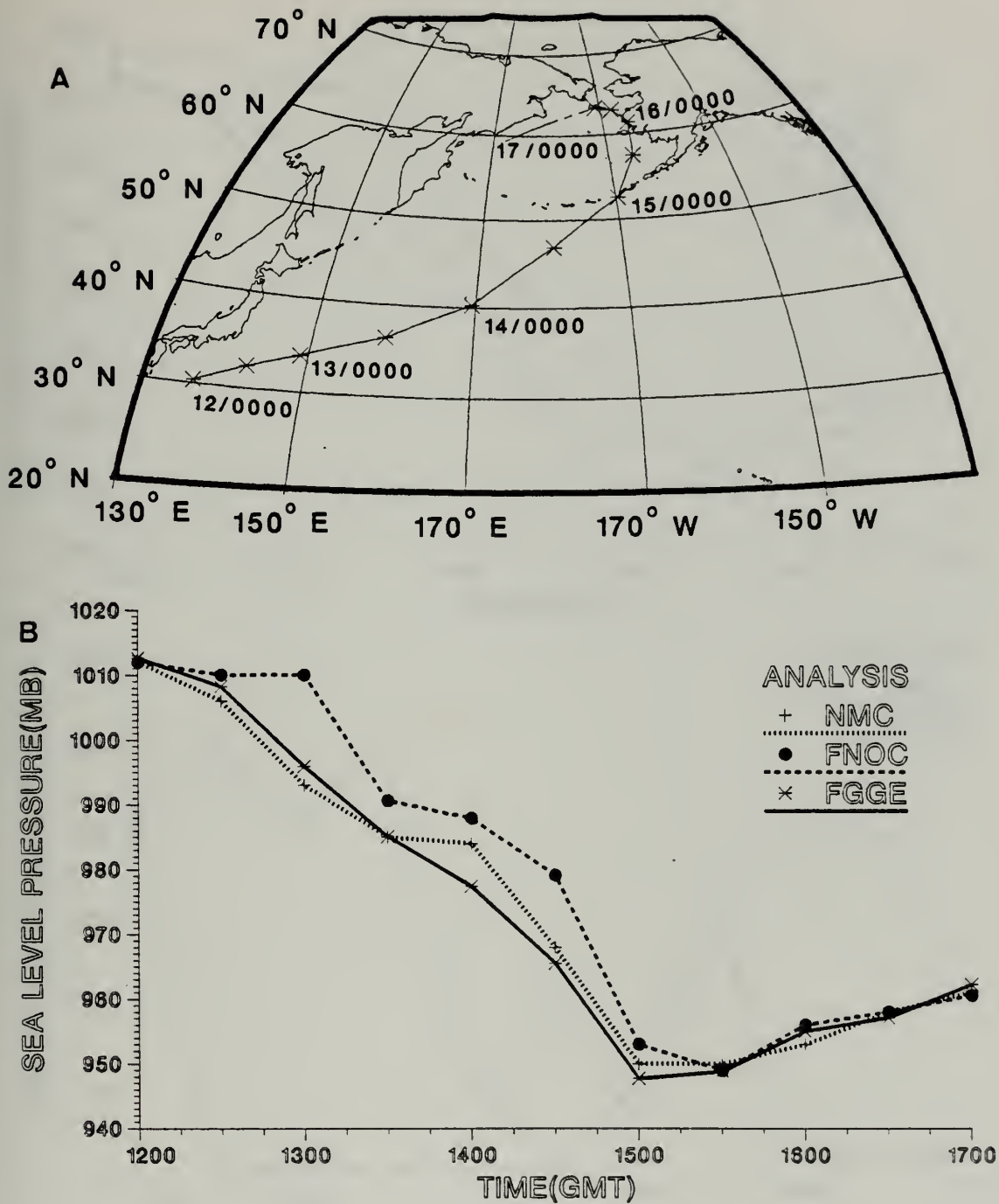


Figure 2. Storm Track Positions and SLP Analyses. (A) Storm Positions in 12-h Increments. (B) Sea Level Pressure Analyses in 12-h Increments. Times 12/0000 and 1200 refer to 0000 GMT 12 January 1979.

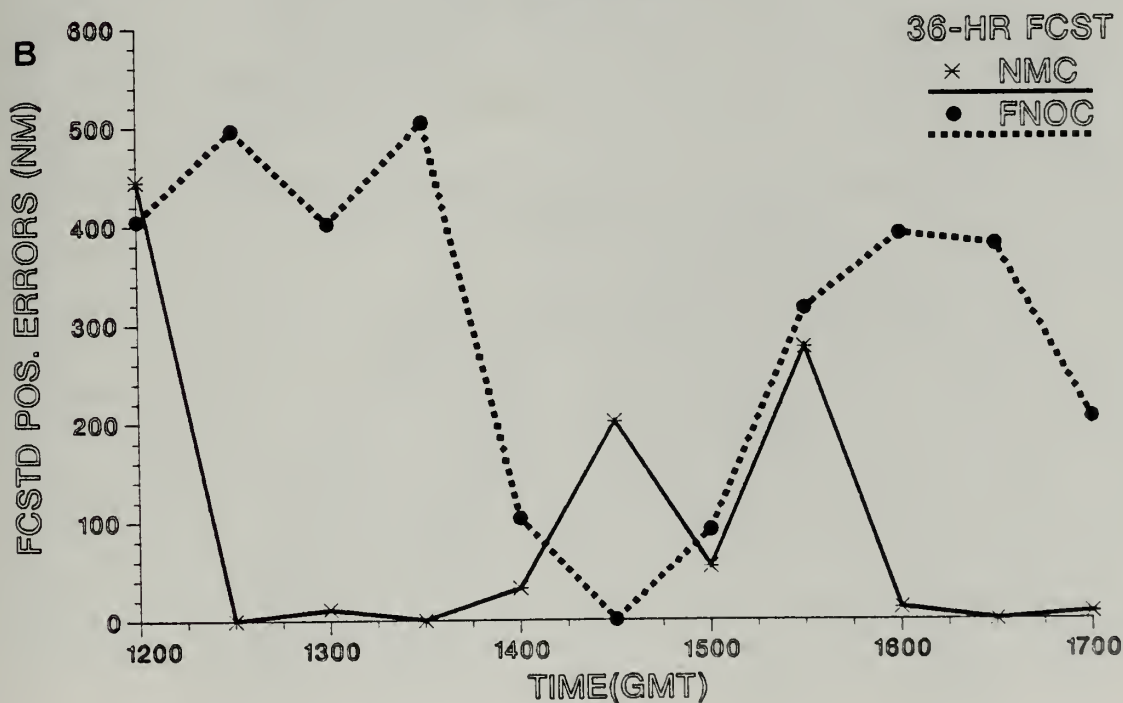
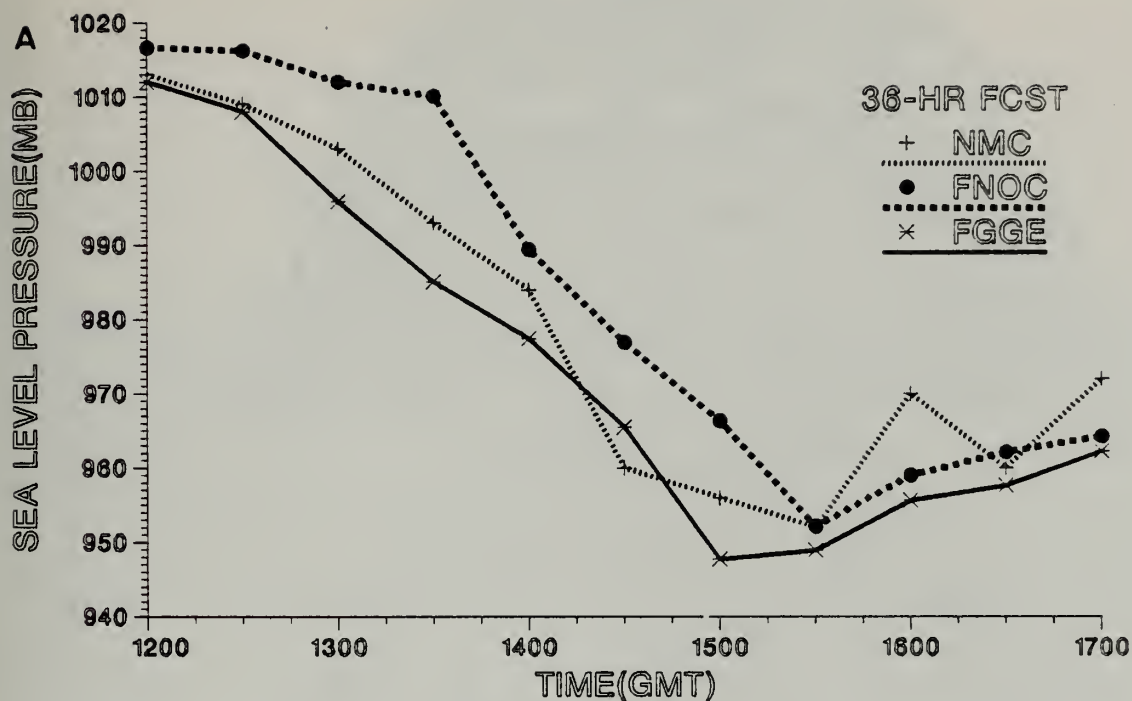
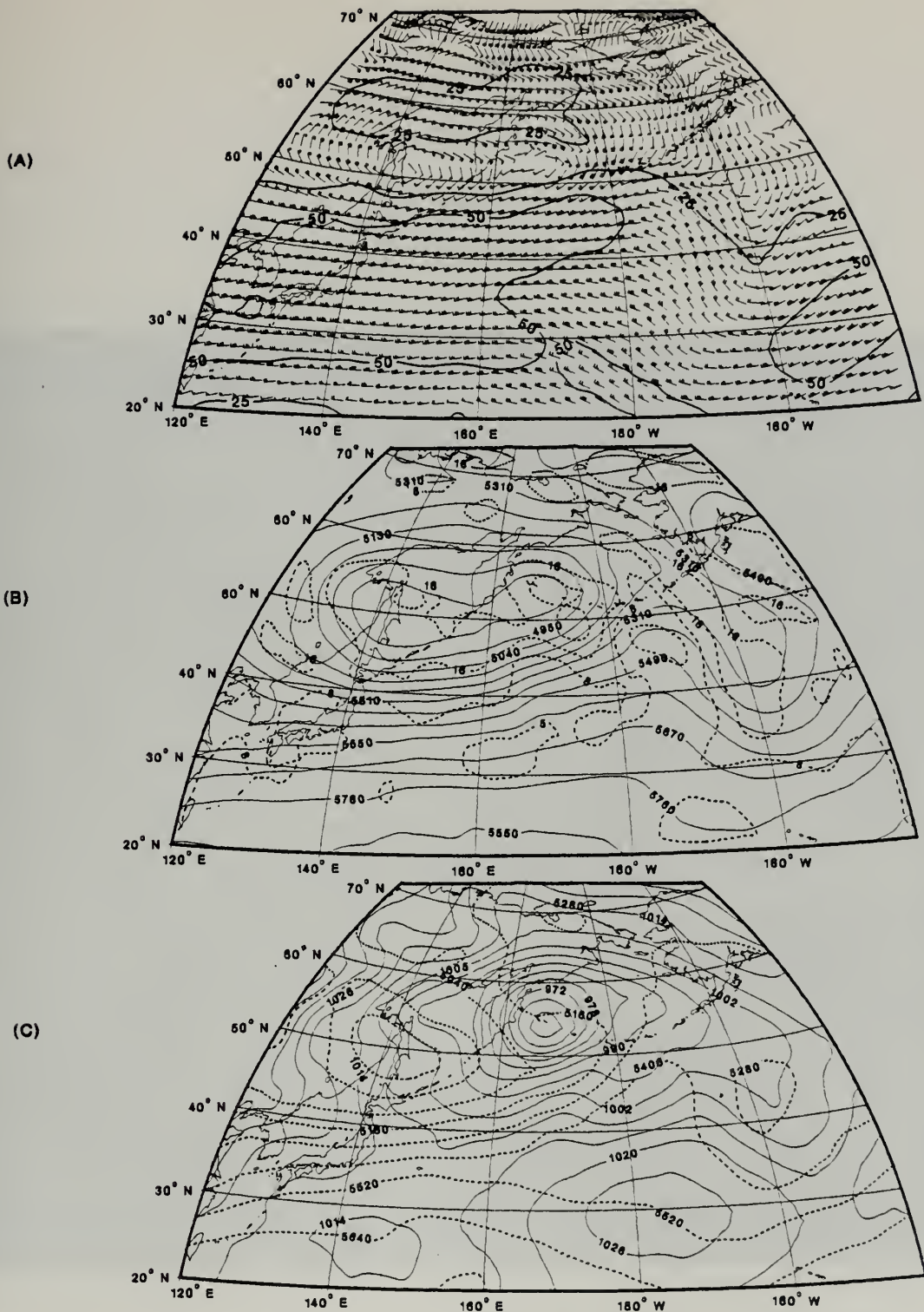


Figure 3. 36-h Forecast SLP and Storm Position Errors. (A) Sea Level Pressure Forecasts in 12-h Increments. (B) Position Errors Based on FGGE Positions. Time 1200 refers to 0000 GMT 12 January 1979.



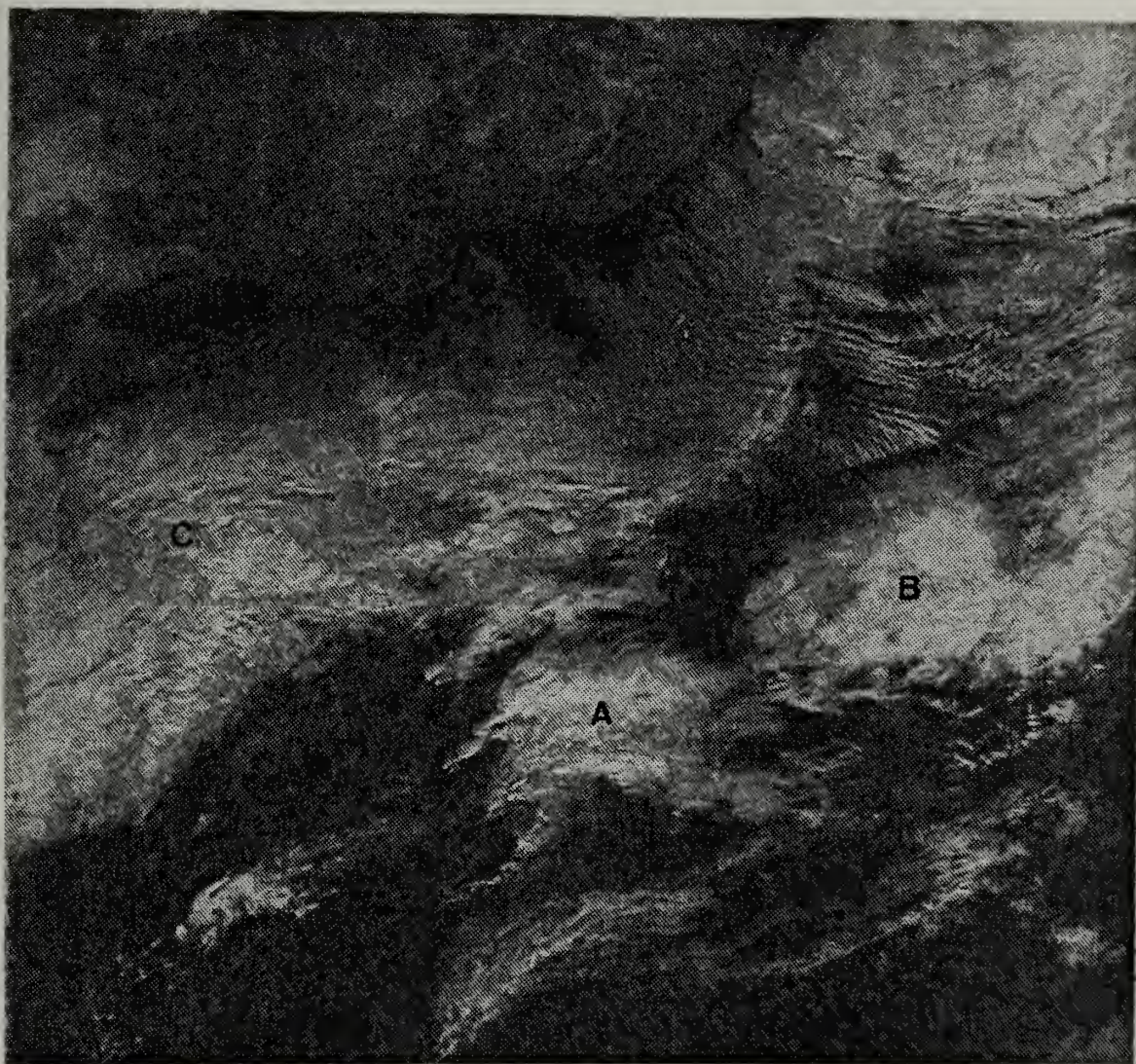


Figure 5. DMSF Visual Satellite Imagery for 0041 GMT 12 January 1979. Labels are (A) Incipient System (B) Secondary Developing System (C) PVA Area Upstream.

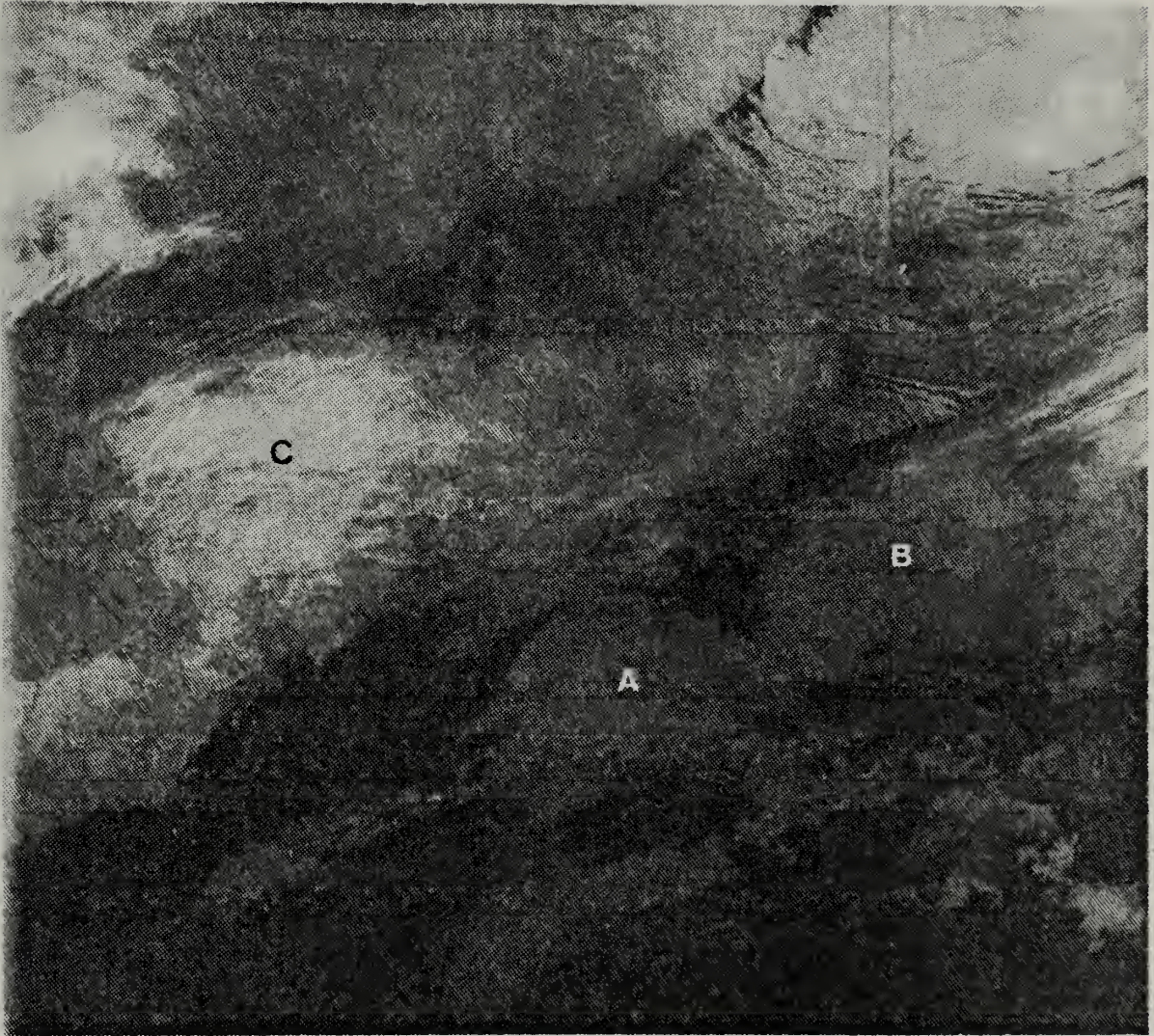


Figure 6. DMSF Infrared Satellite Imagery for 0041 GMT 12 January 1979. Labels are (A) Incipient System (B) Secondary Developing System (C) PVA Area Upstream.

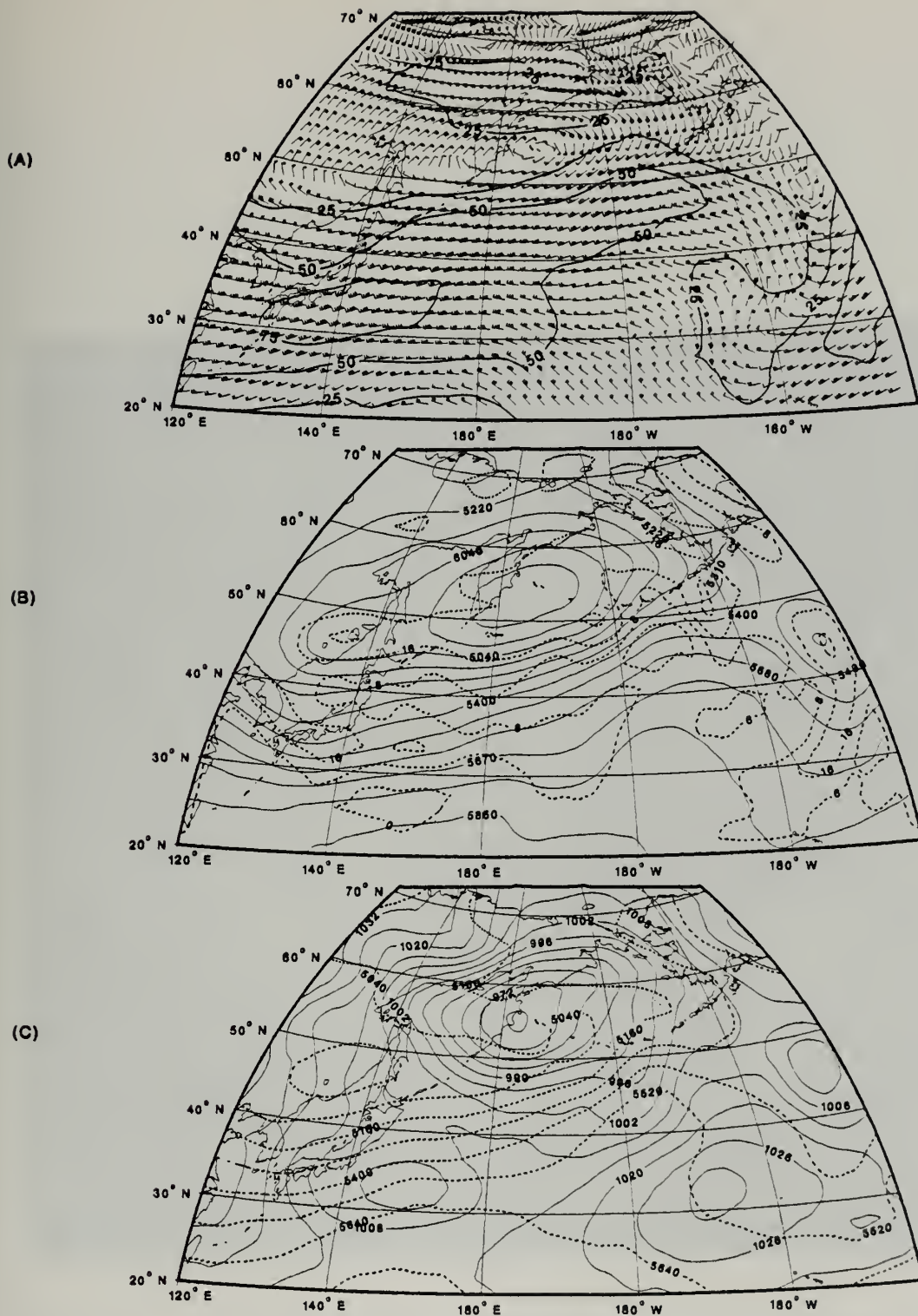


Figure 7. Same as Figure 4 except for 0000 GMT 13 January 1979.

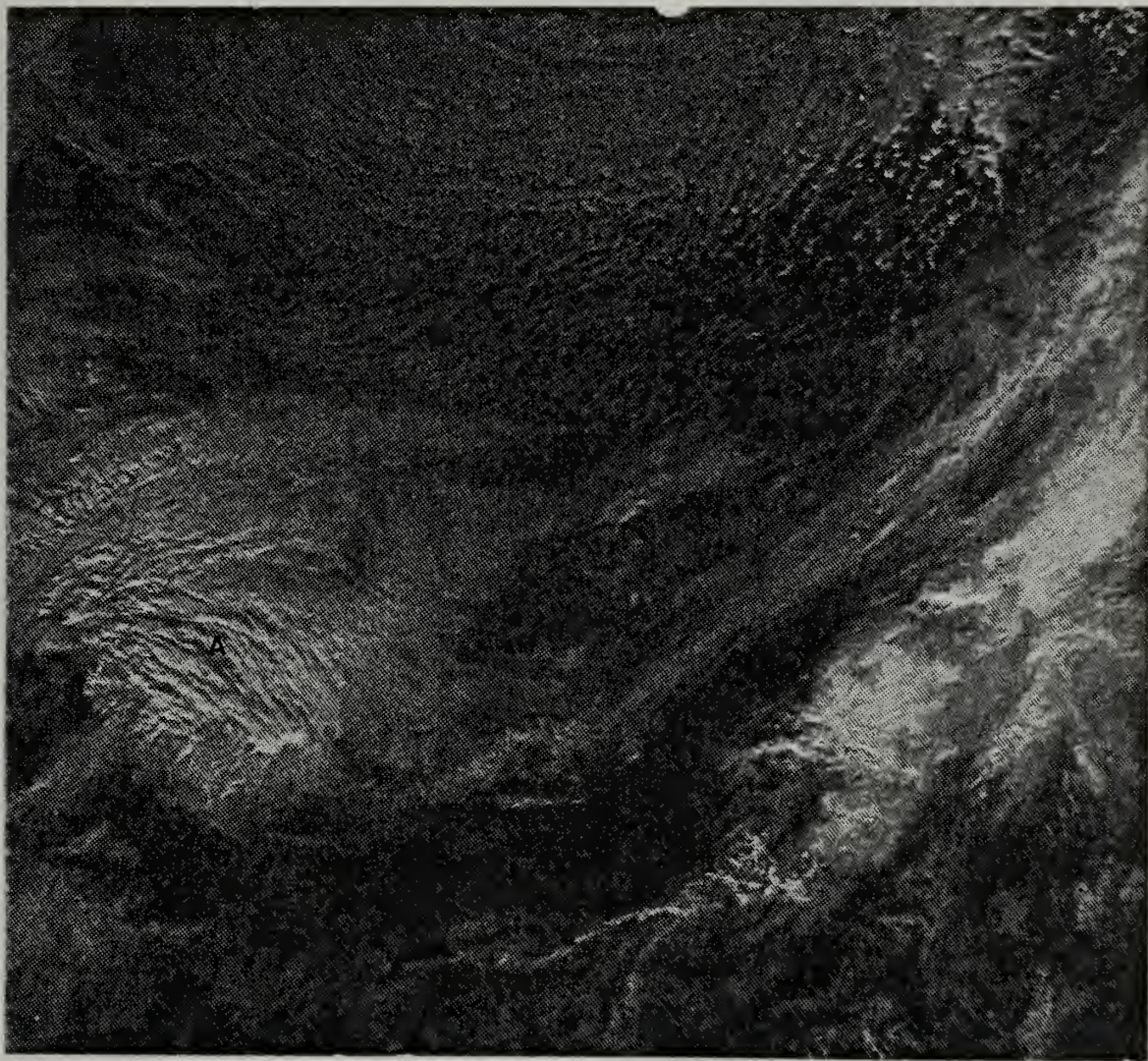


Figure 8. Same as Figure 5 except for 2341 GMT 12 January 1979. Label A is Incipient System.

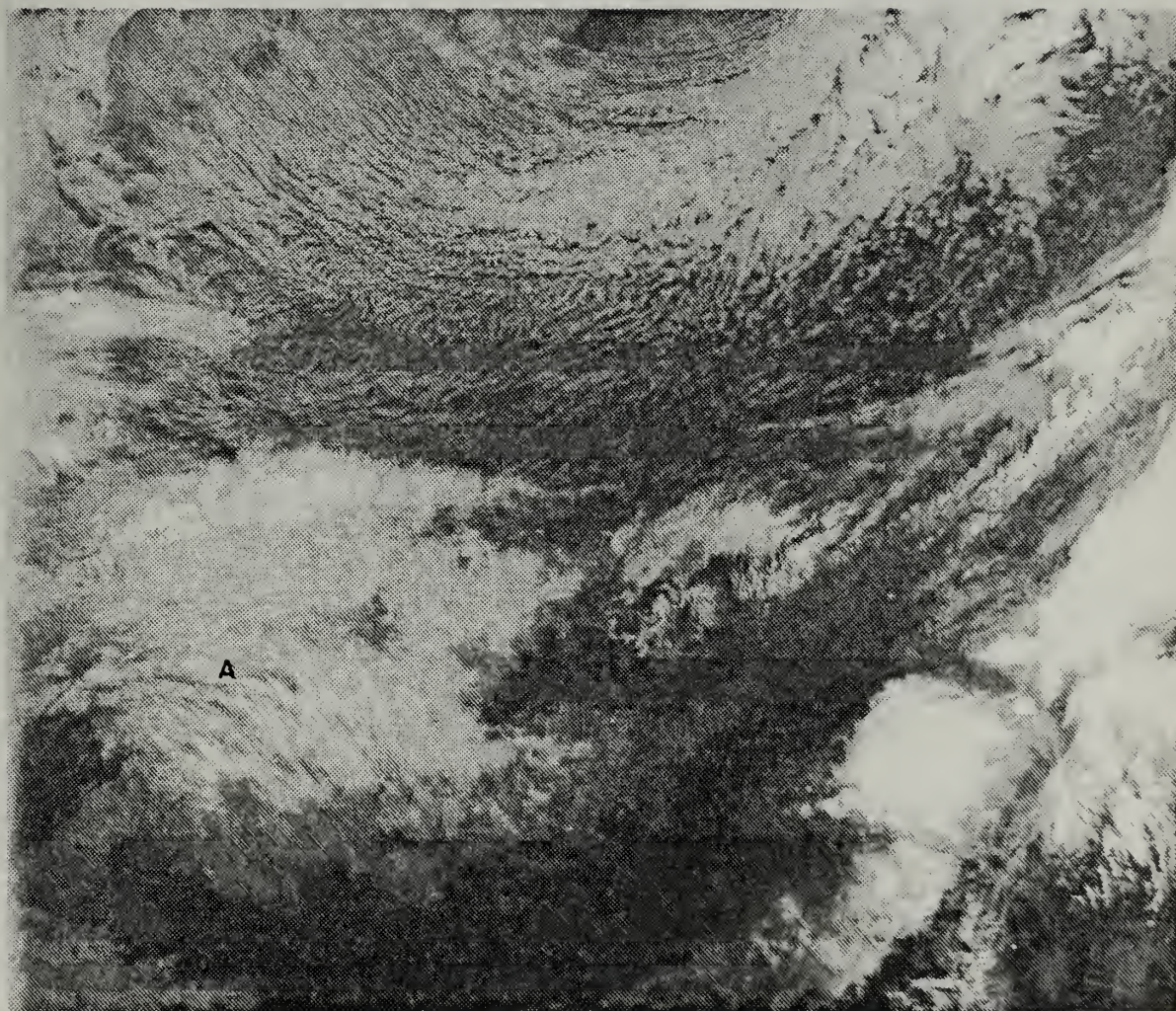


Figure 9. Same as Figure 6 except for 2341 GMT 12 January 1979. Label A is Incipient System.

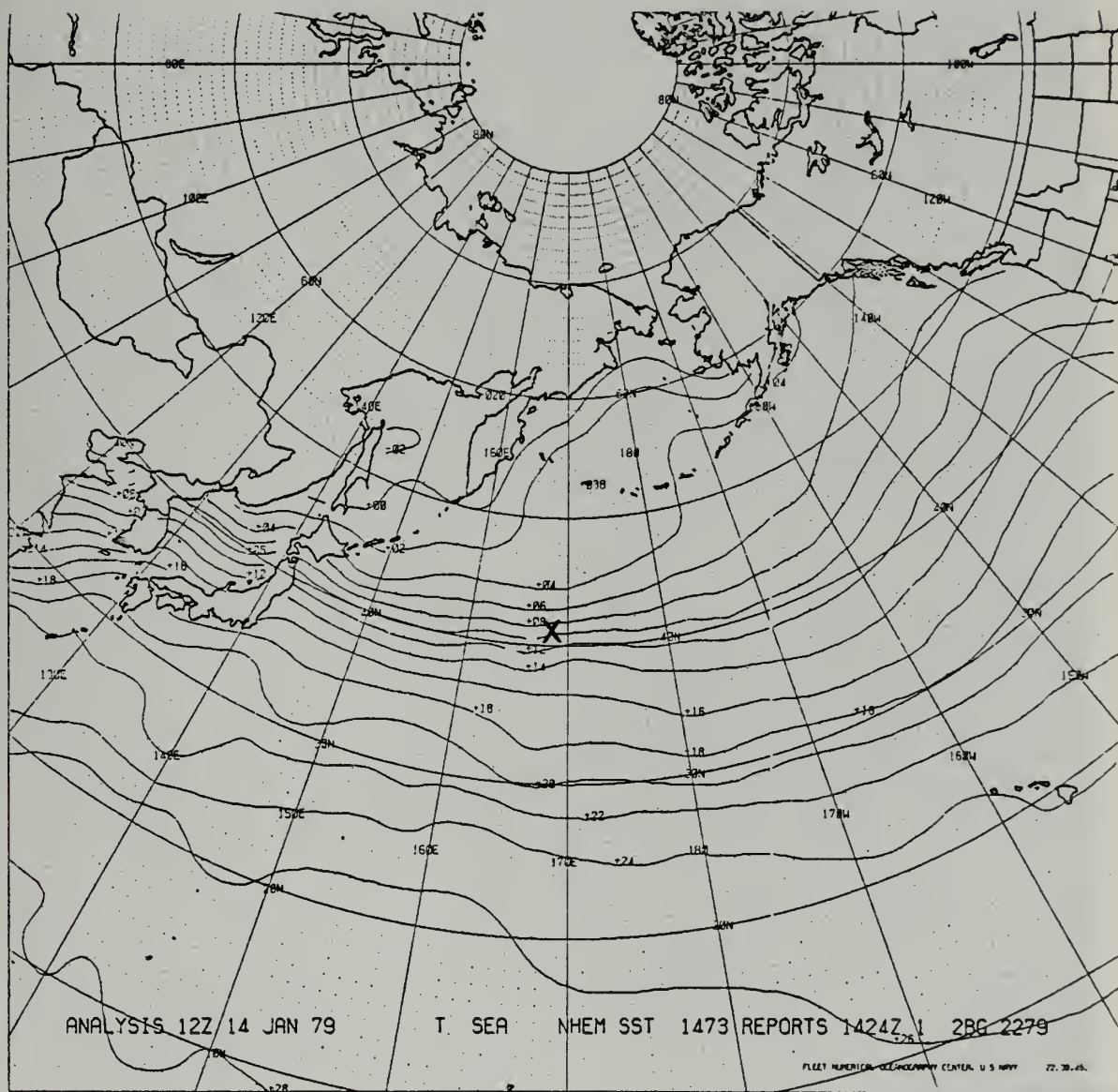


Figure 11. FNCC SST Analysis Valid 1200 GMT 14 January 1979. "X" marks cyclone position at 0000 GMT 14 January. Isotherms in degrees Celsius.

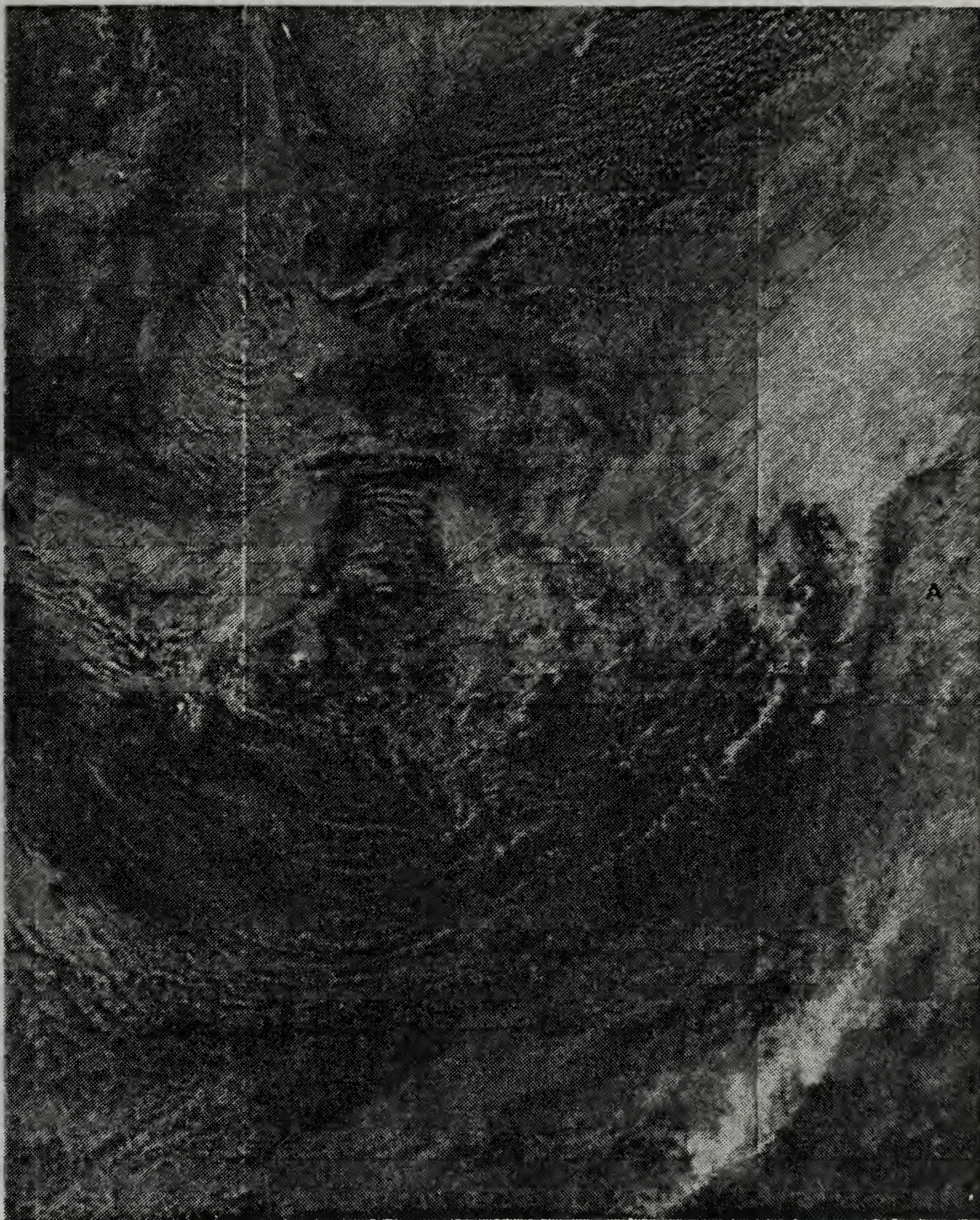


Figure 12. Same as Figure 5 except for 1405 GMT 13 January 1979. Label A Indicates Jet-Frontal Intersection.

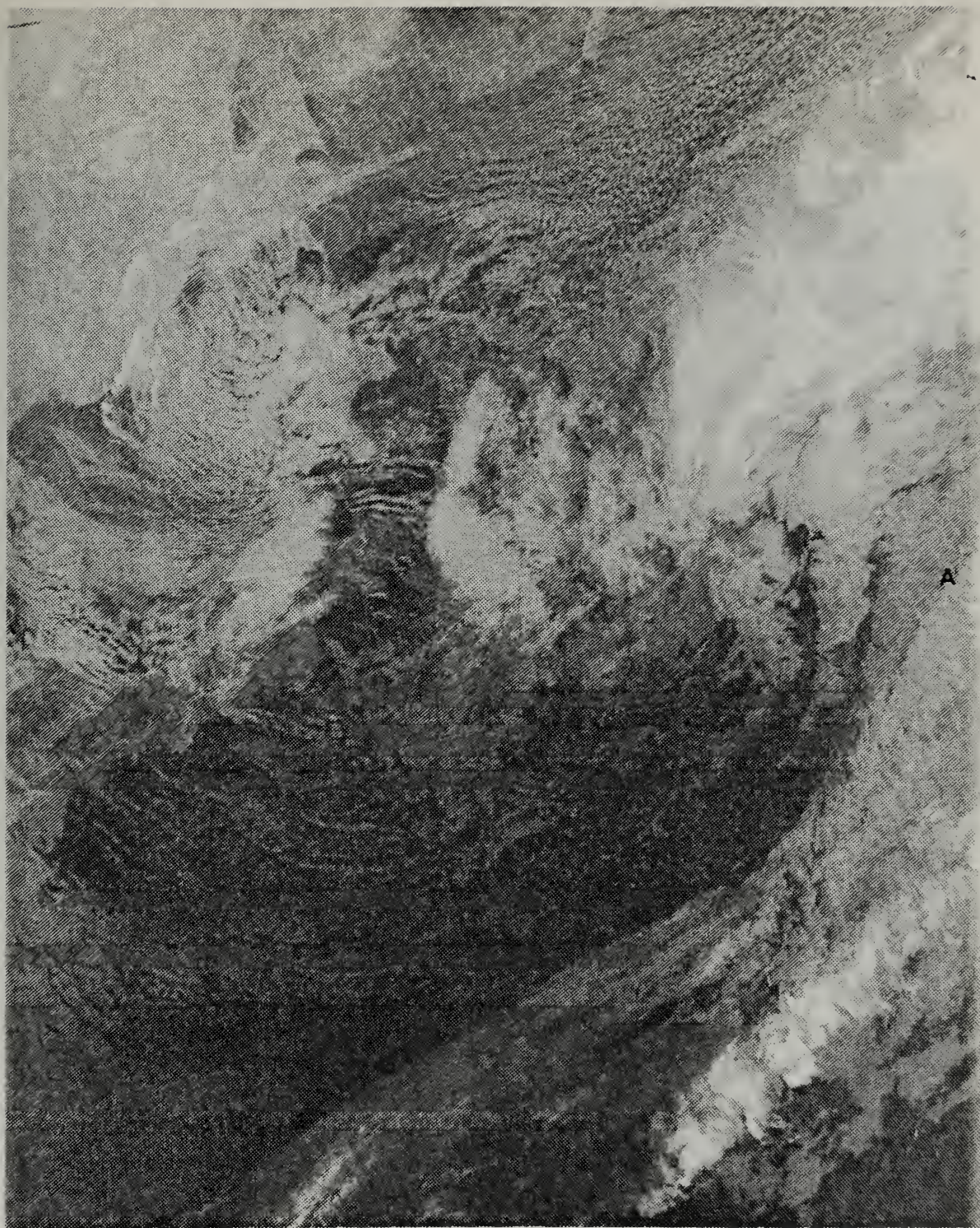


Figure 13. Same as Figure 6 except for 1405 GMT 13 January 1979. Label A Indicates Jet-Frontal Intersection.

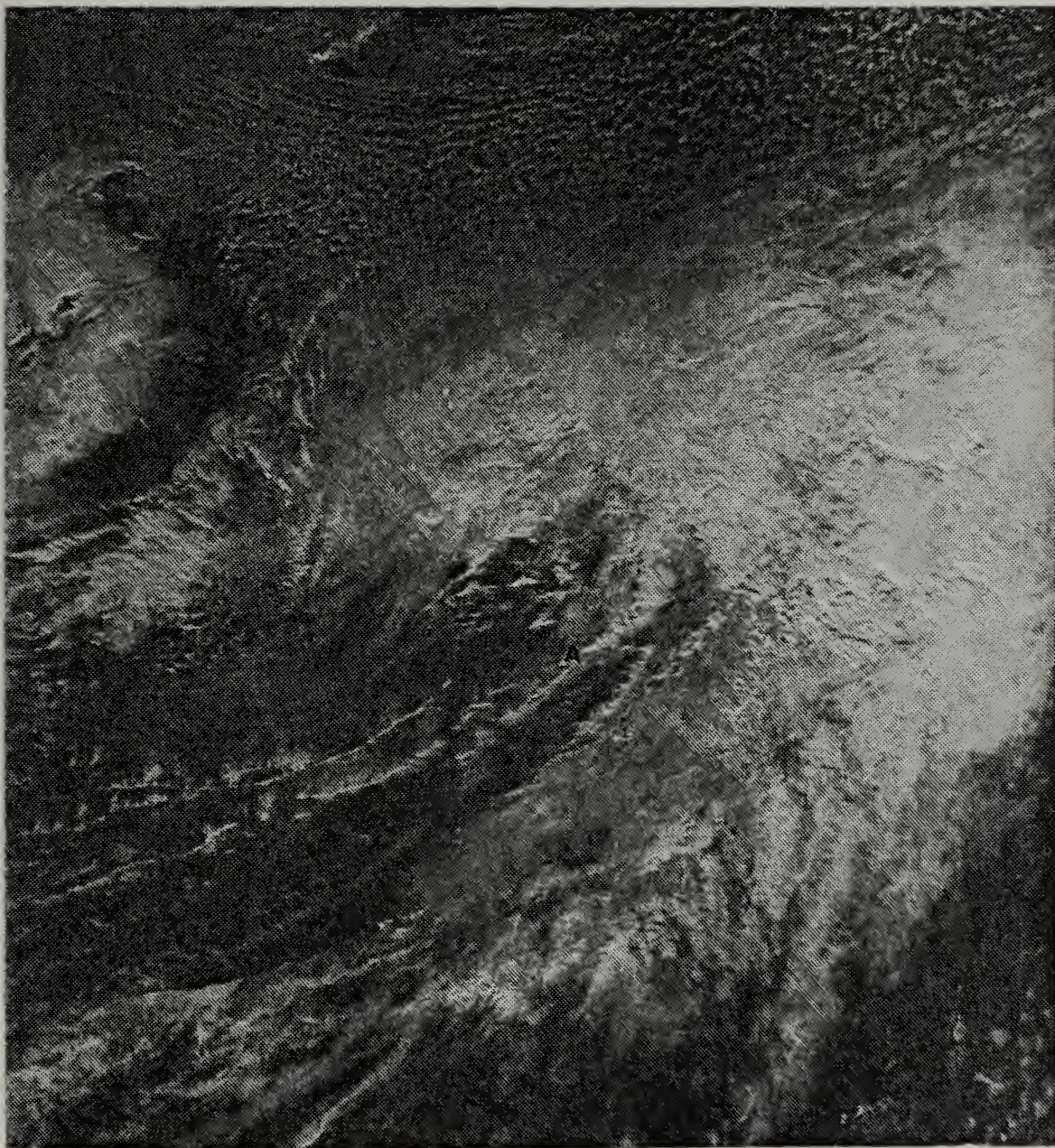


Figure 14. Same as Figure 5 except for 0023 GMT 14 January 1979. Label A Indicates Feeder Bands.

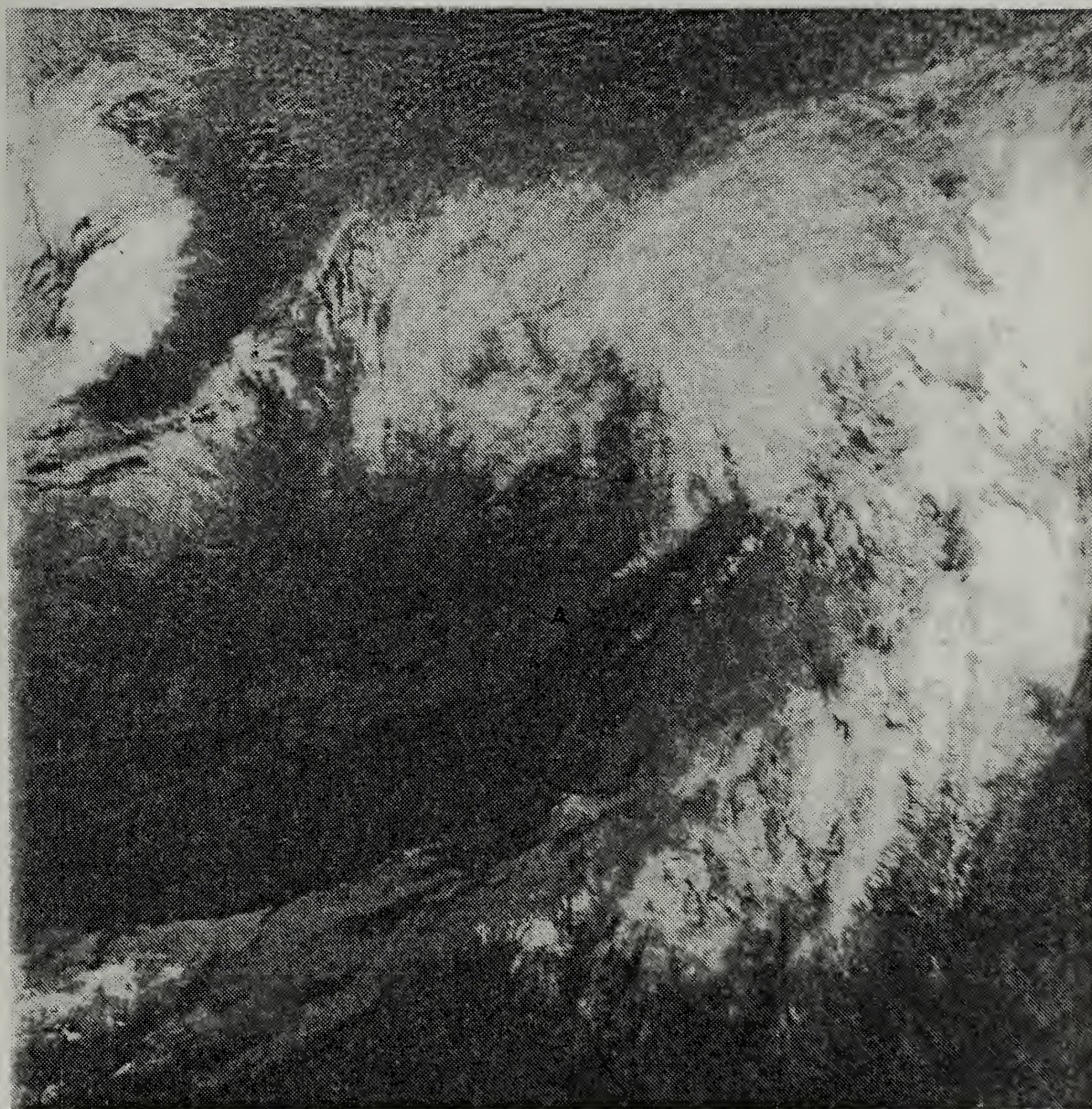


Figure 15. Same as Figure 6 except for 0023 GMT 14 January 1979. Label A Indicates Feeder Bands.



Figure 17. Same as Figure 5 except for 1205 GMT 14 January 1979.

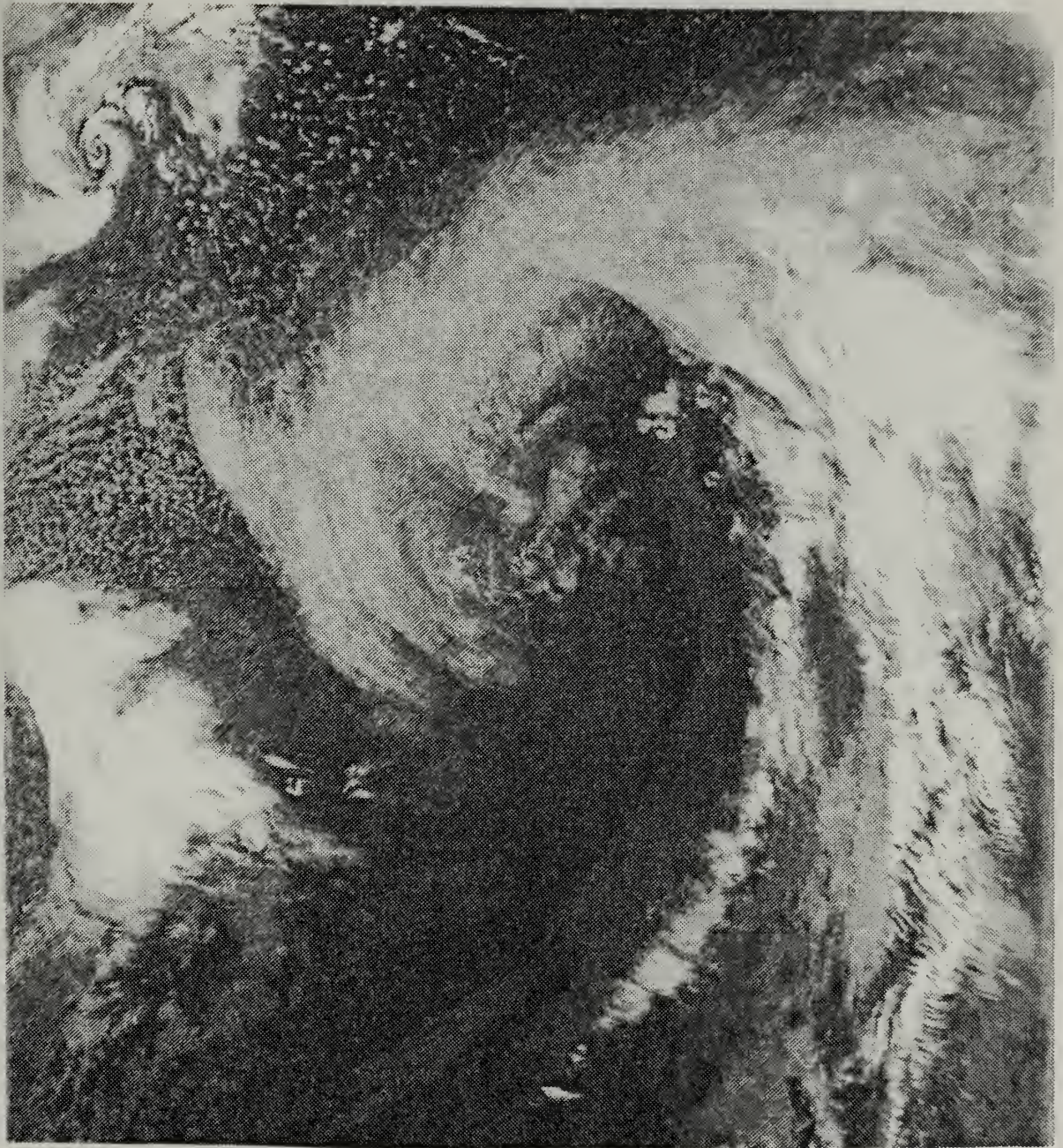


Figure 18. Same as Figure 6 except for 1205 GMT 14 January 1979.

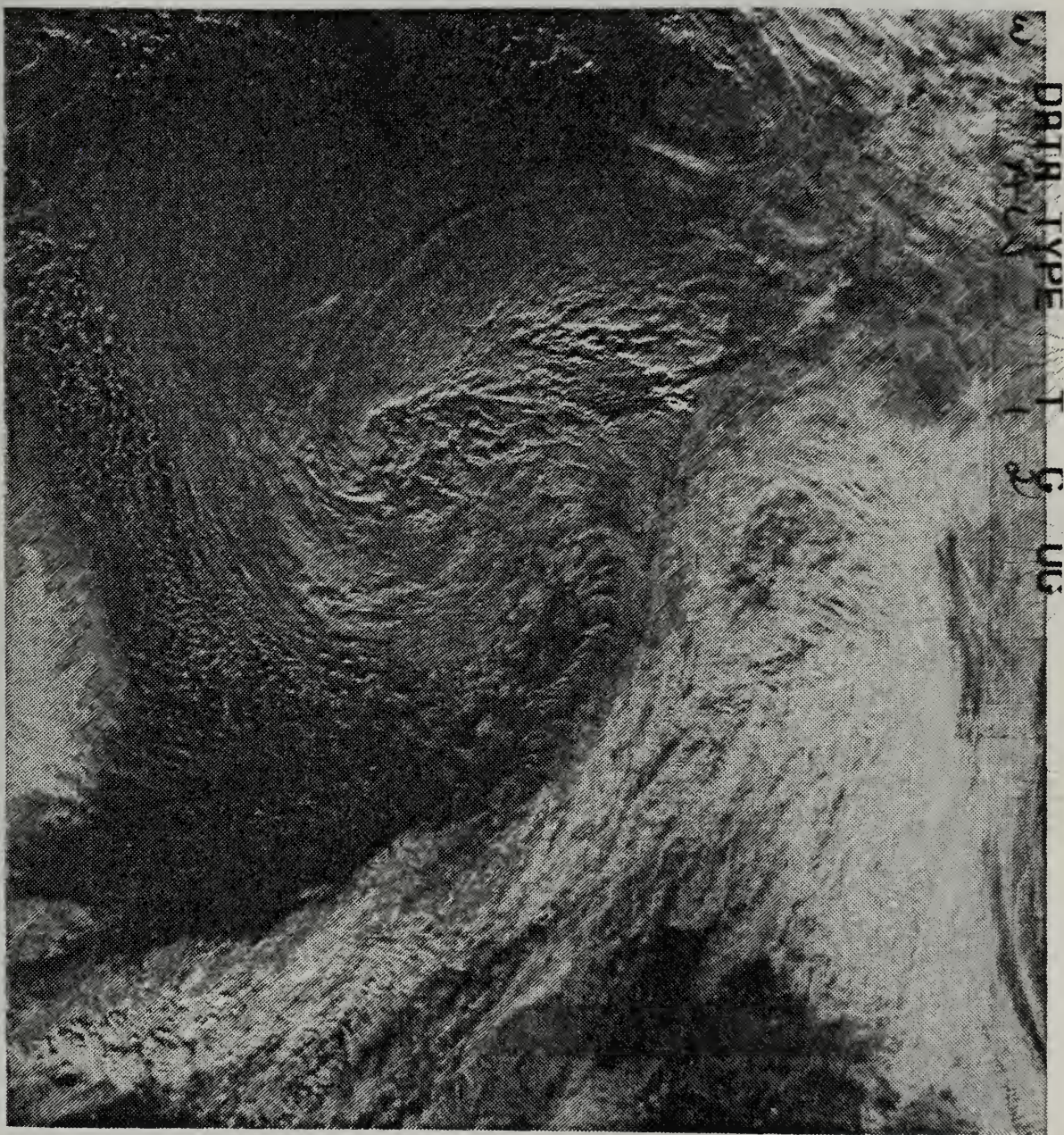


Figure 20. Same as Figure 5 except for 2124 GMT 14 January 1979.

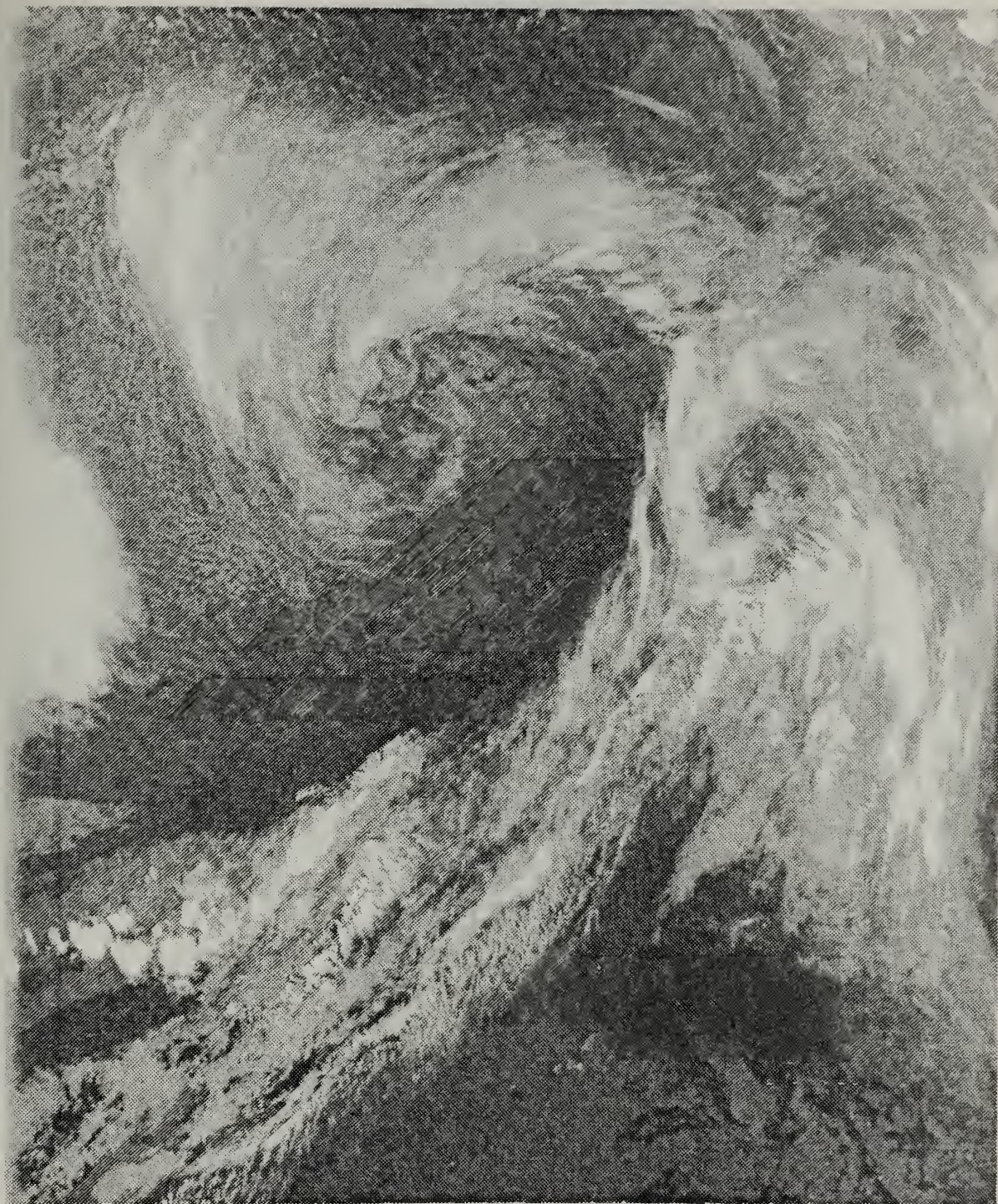
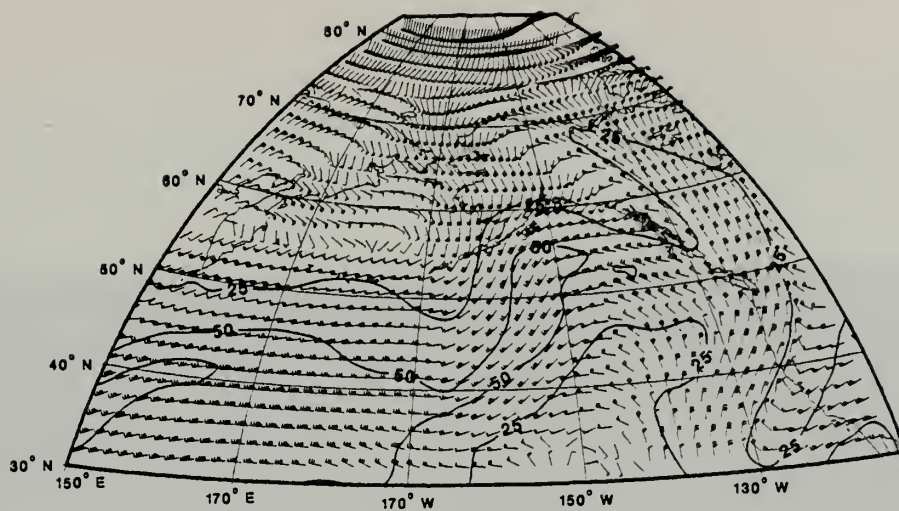
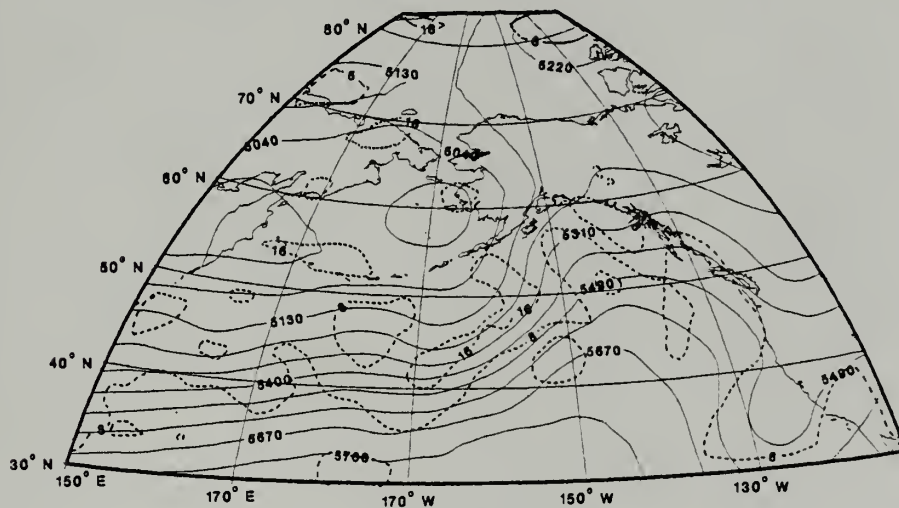


Figure 21. Same as Figure 6 except for 2124 GMT 14 January 1979.

(A)



(B)



(C)

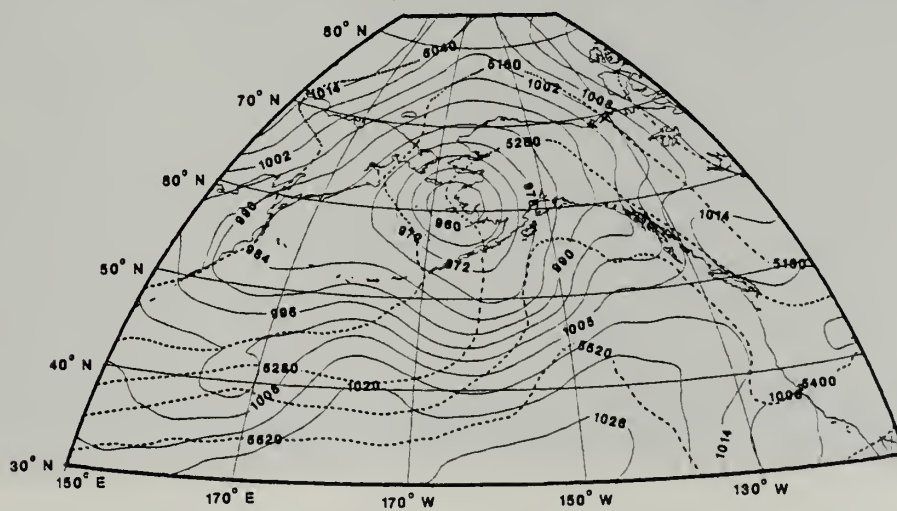


Figure 23. Same as Figure 4 except for 0000 GMT 16 January 1979.



Figure 24. Same as Figure 5 except for 1005 GMT 16 January 1979.



Figure 25. Same as Figure 6 except for 1005 GMT 16 January 1979.

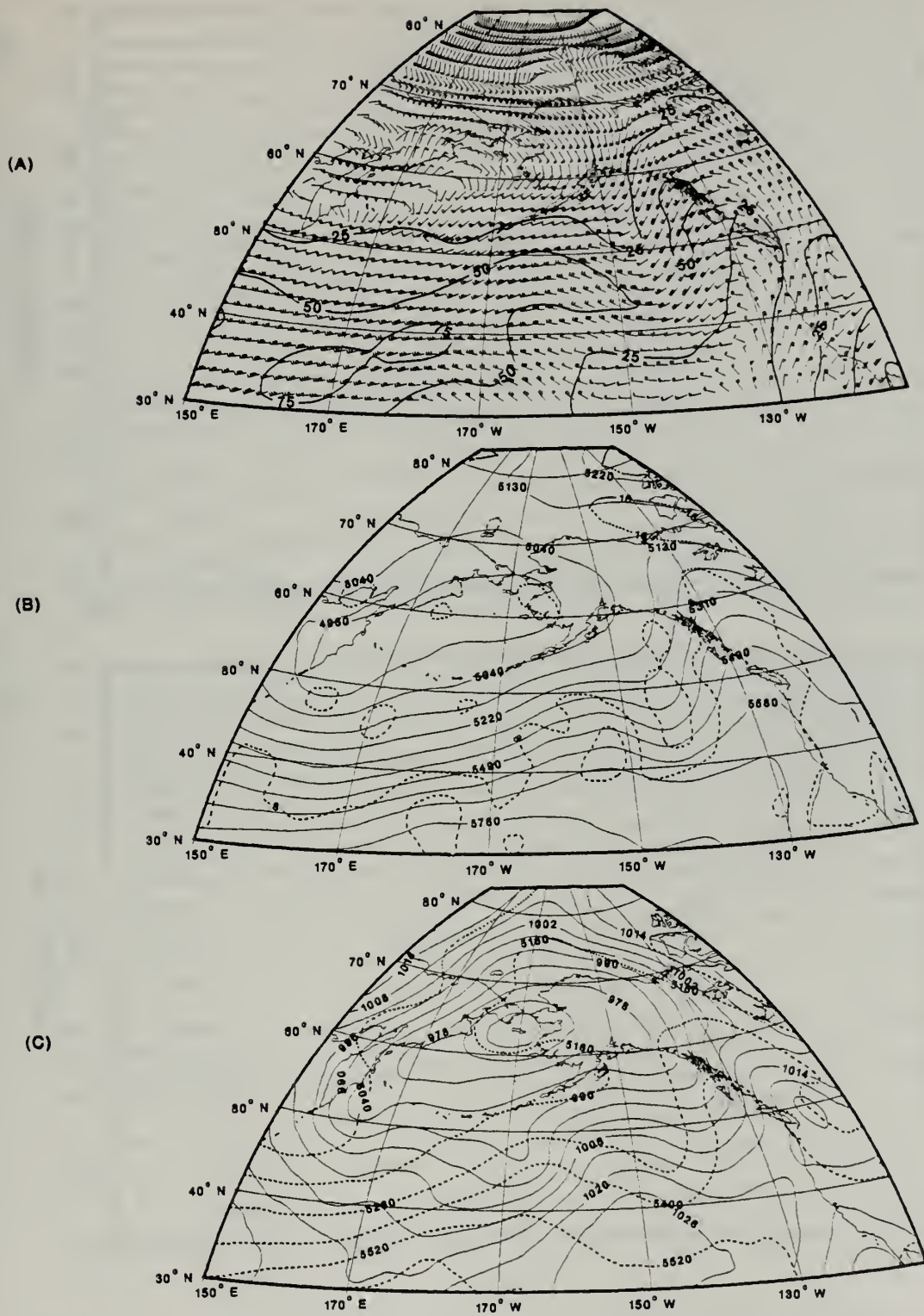


Figure 26. Same as Figure 4 except for 0000 GMT 17 January 1979.

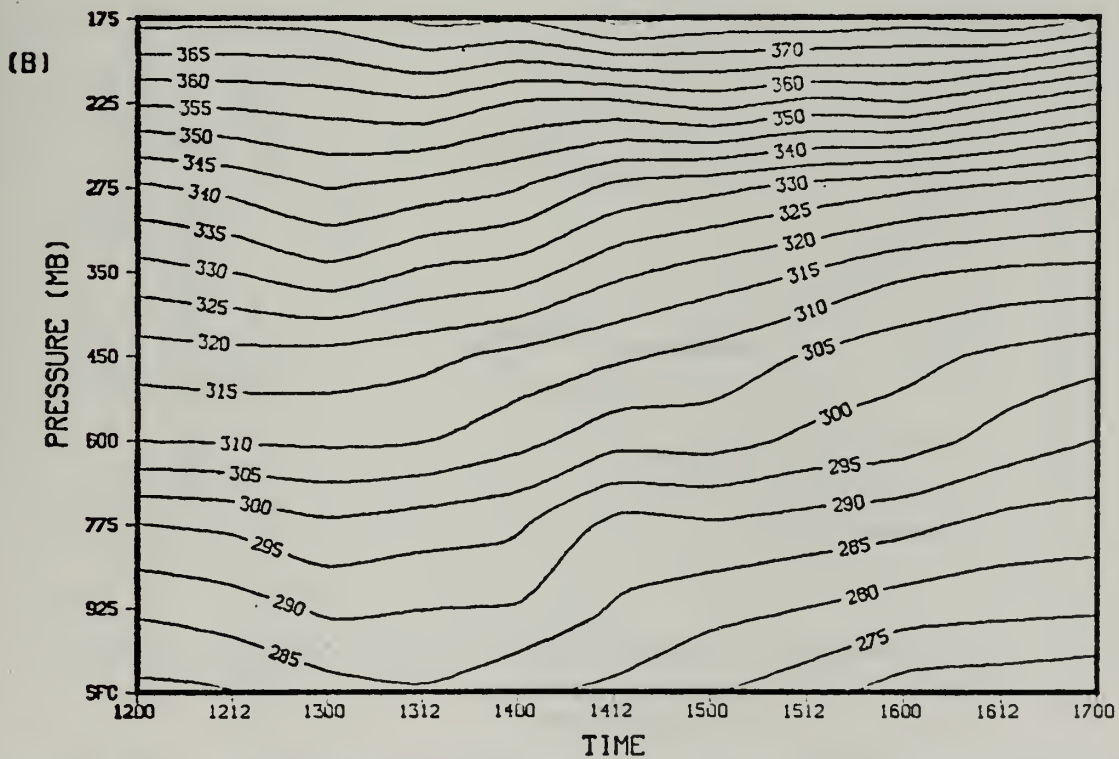
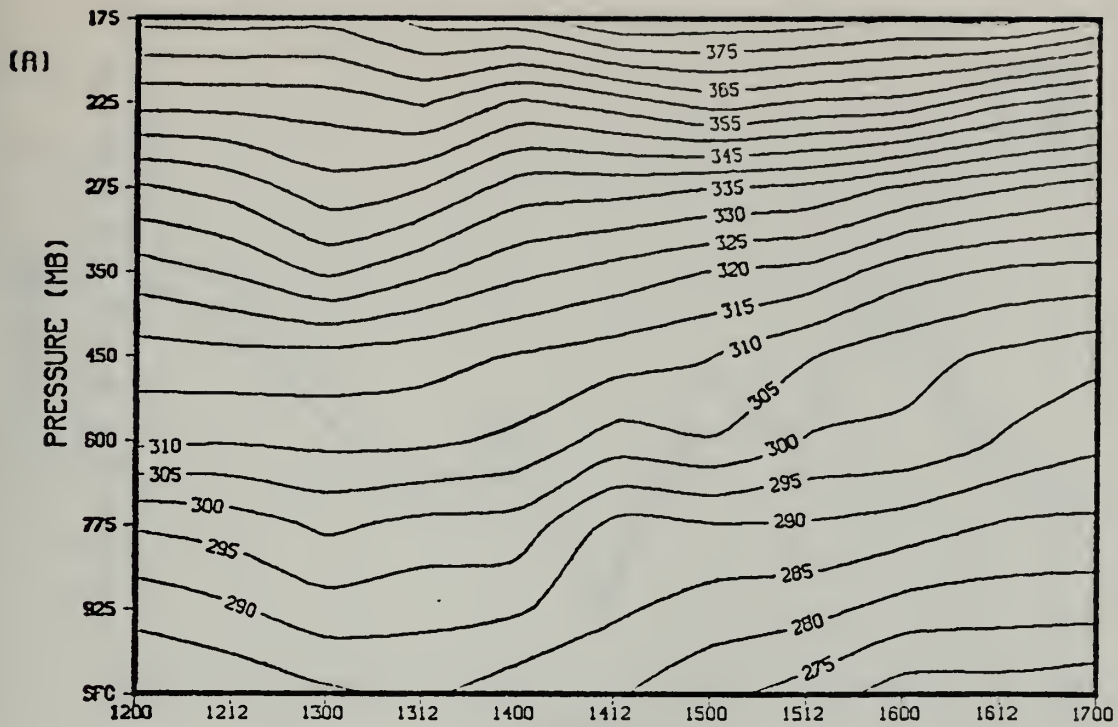


Figure 27. Area-Averaged Potential Temperature Time Sections (A) Radius 6. (B) Radius 10. Values are in Degrees Kelvin. Time 1200 Refers to 0000 GMT 12 January.

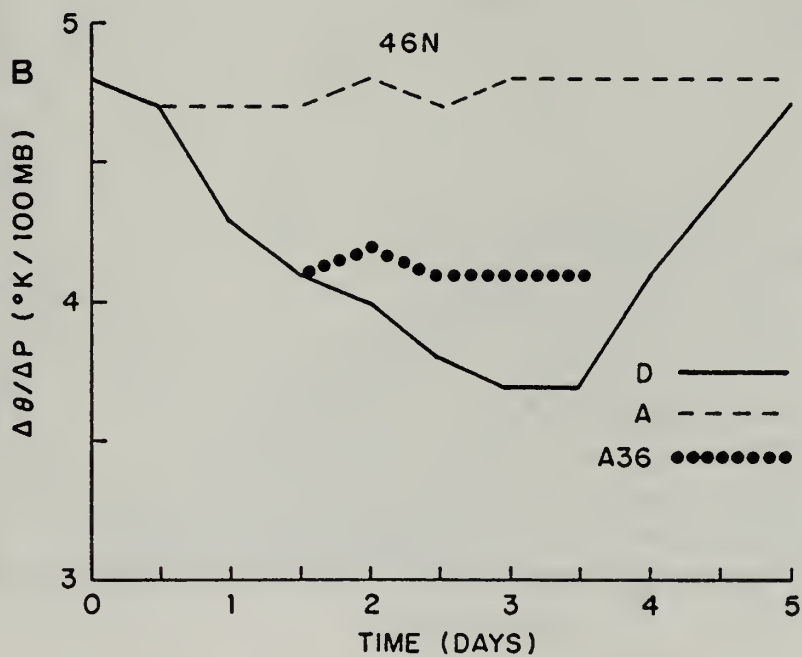
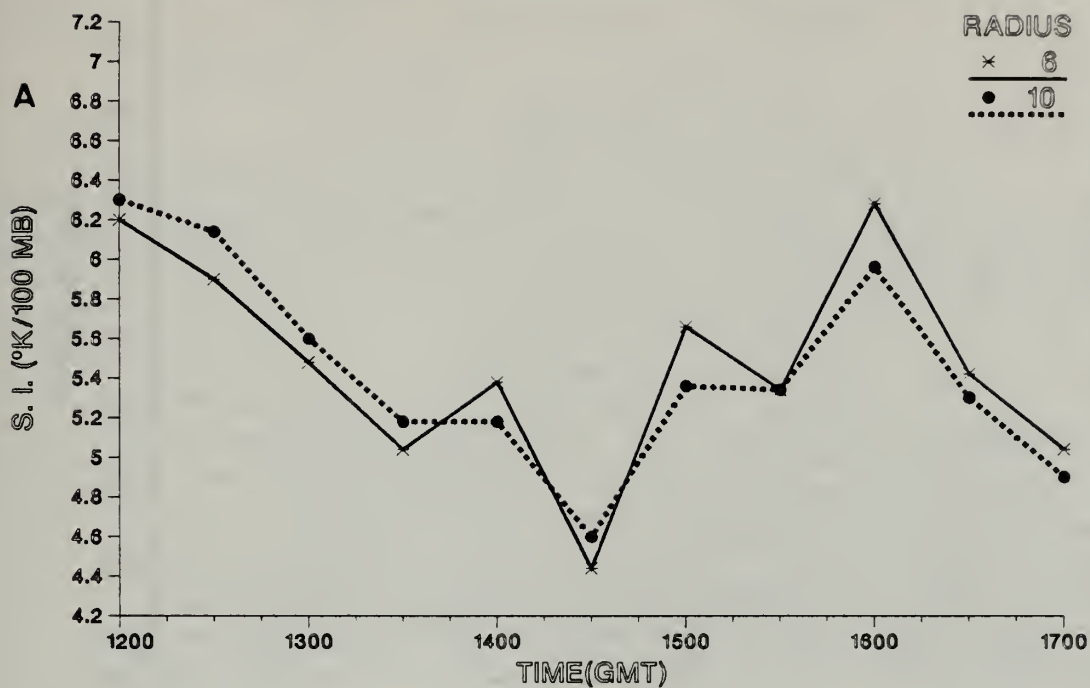


Figure 28. Stability Index (A) Observed (B) Simulated (From Sandgathe, 1981). Values in Degrees Kelvin / 100 mb. Time 1200 Refers to 0000 GMT 12 January.

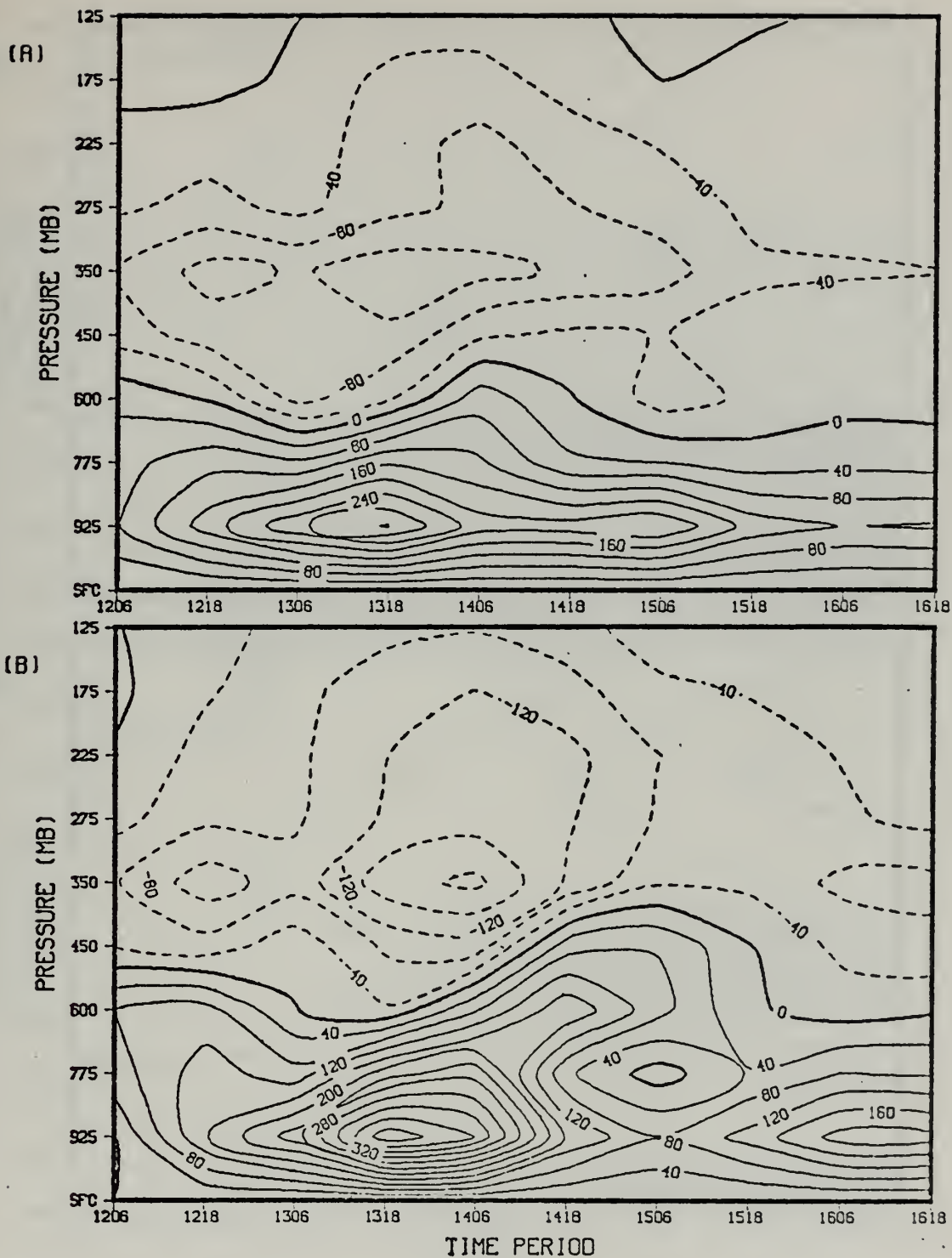


Figure 29. Corrected Lateral Mass Transport Time Sections. (A) Radius 6 (B) Radius 10. Contour Interval is $40 \times (10 \times 11)$. Dashed (Negative) Values Indicate Flux Cut out of the Volume. Units are in gm/sec-100 mb . Period 1206 Refers to 0000-1200 GMT 12 January.

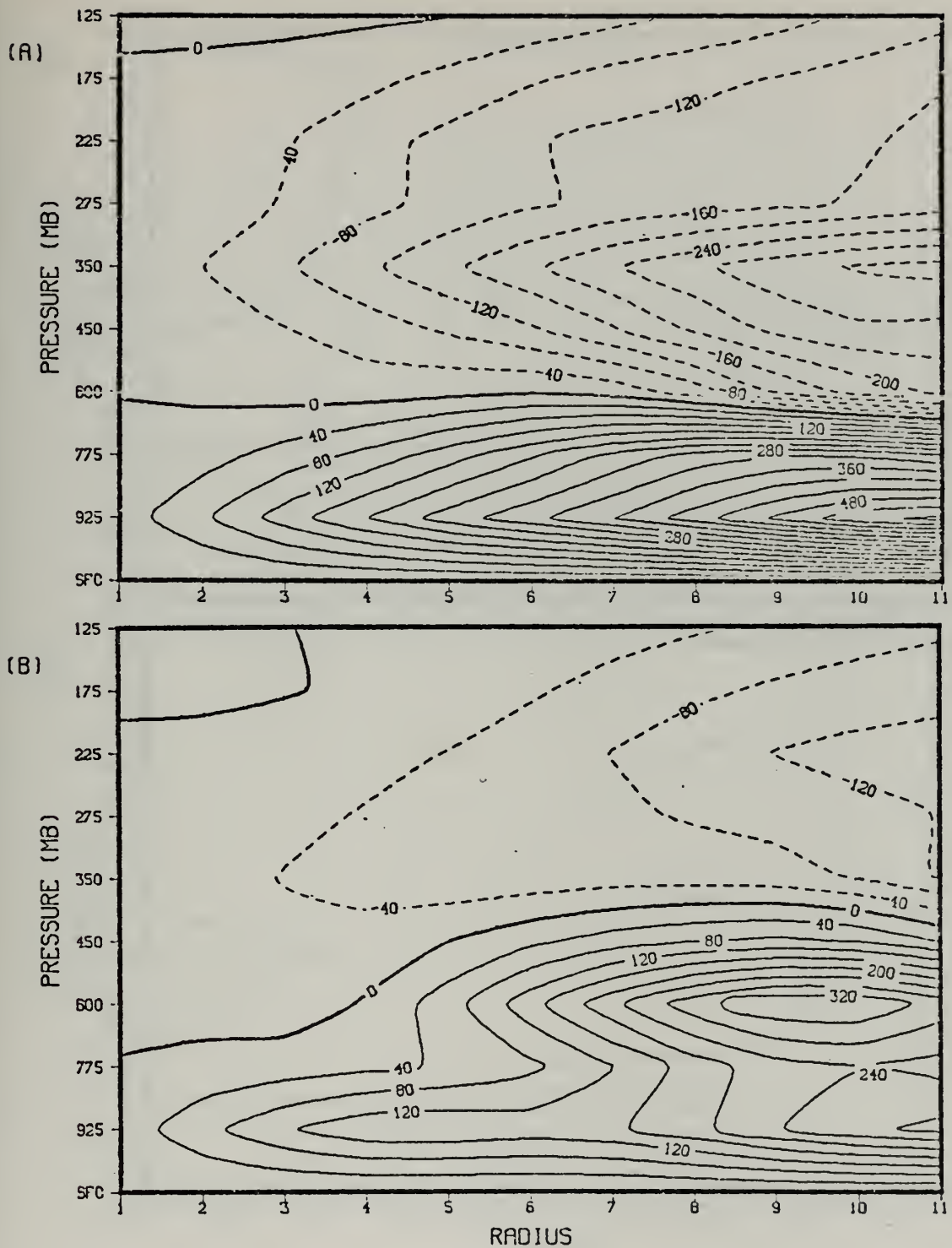


Figure 30. Radial Section of Lateral Mass Transport (A) Time 1400 (B) Time 1412. Units and Contours as in Figure 29.

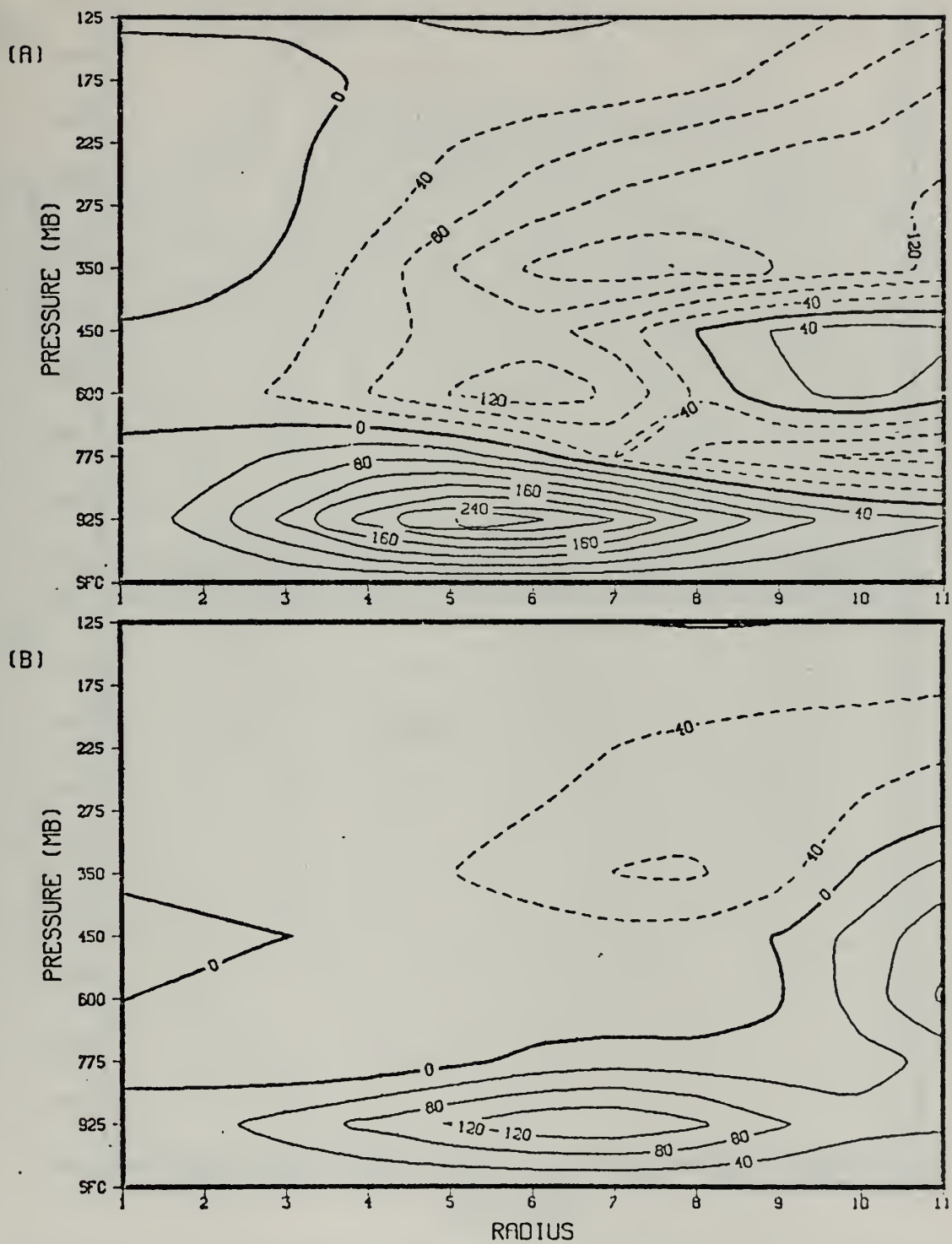


Figure 31. Radial Section of Lateral Mass Transport (A) Time 1500 (B) Time 1512. Units and Contours as in Figure 29.

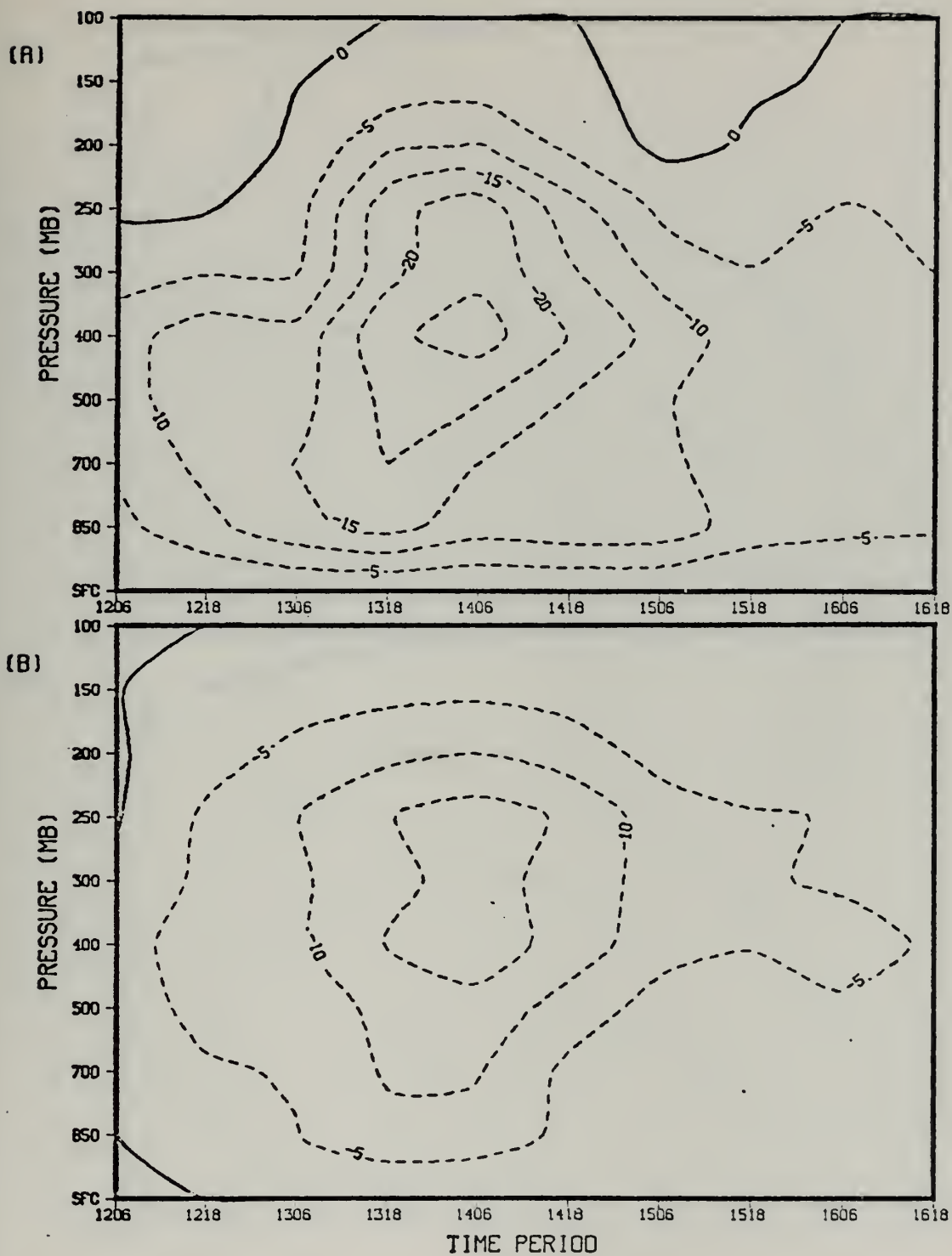


Figure 32. QID Derived Vertical Velocities (A) Radius 6 (B) Radius 10. Units are in mb/1000-sec. Time Periods as in Figure 29.

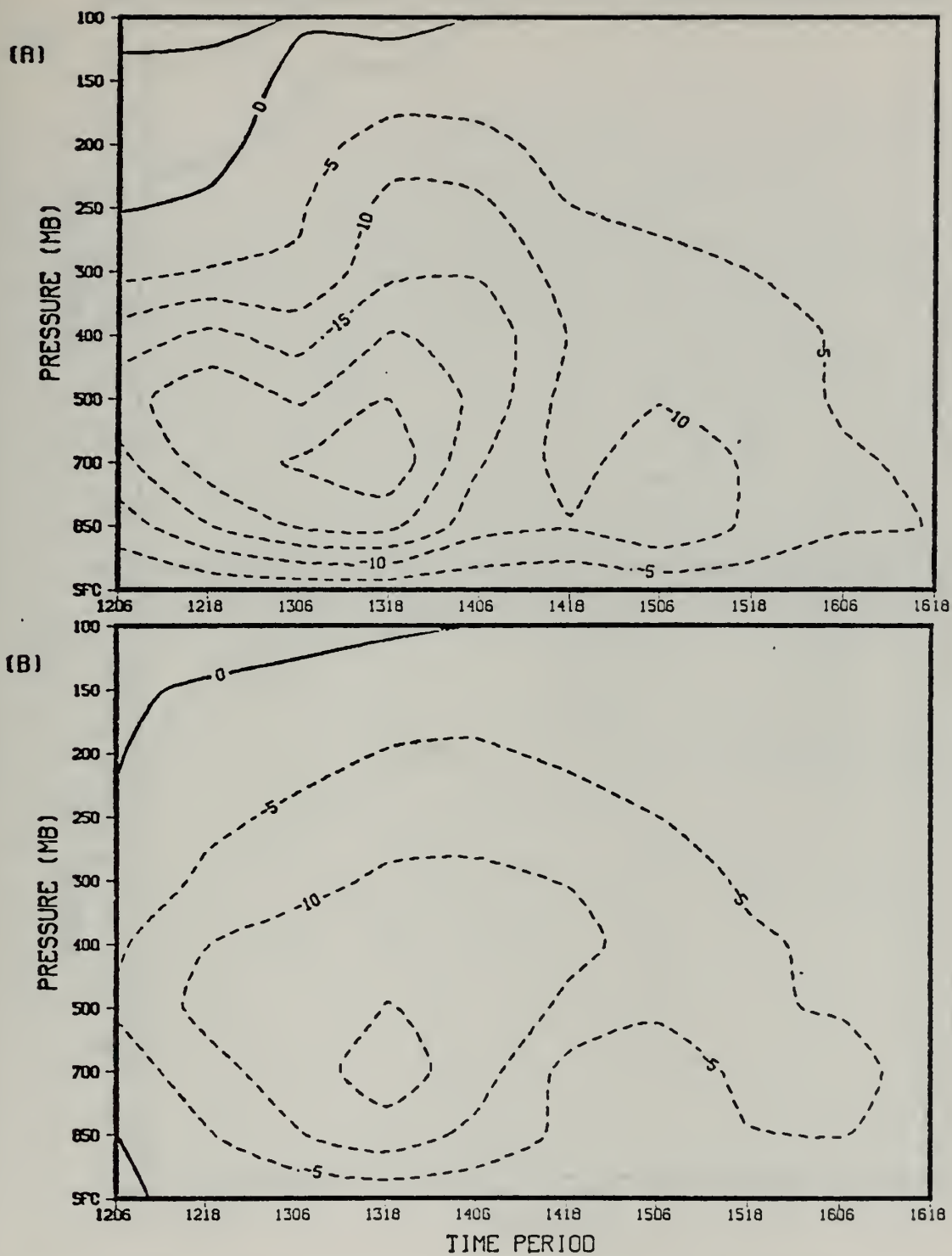


Figure 33. FGGE Derived Vertical Velocities (A) Radius 6 (B) Radius 10. Units are in mb/1000-sec. Time Periods as in Figure 29.

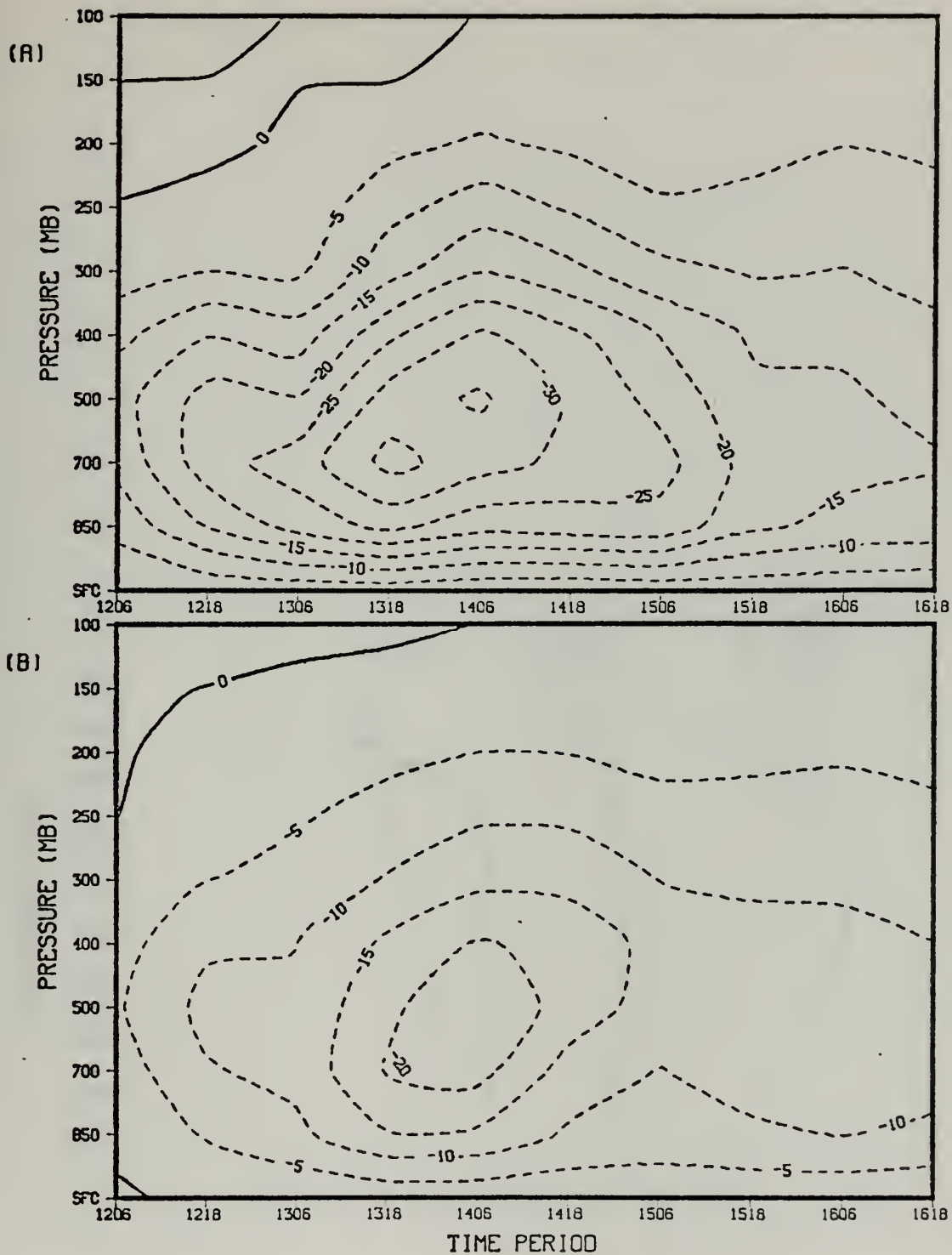


Figure 34. Kinematic Vertical Velocities (A) Radius 6 (B) Radius 10. Units are in mb/1000-sec. Time Periods as in Figure 29.

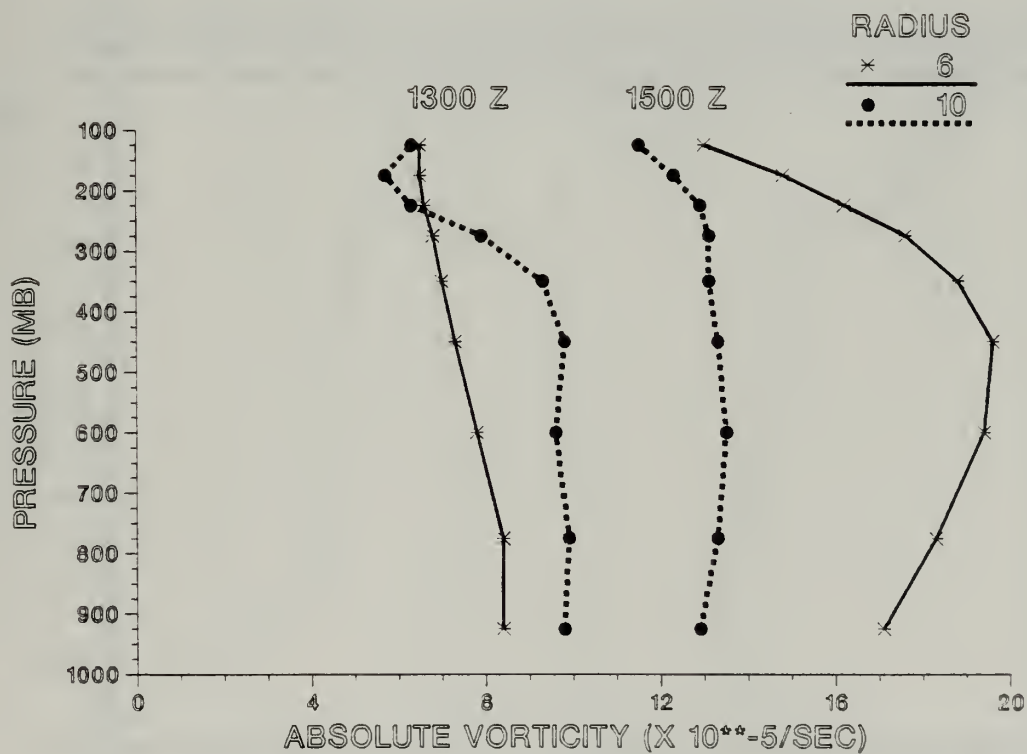


Figure 35. Budget Volume Absolute Vorticity for Radius 6 and Radius 10 for Two Times. Time 1300 Z Refers to 0000 GMT 13 January.

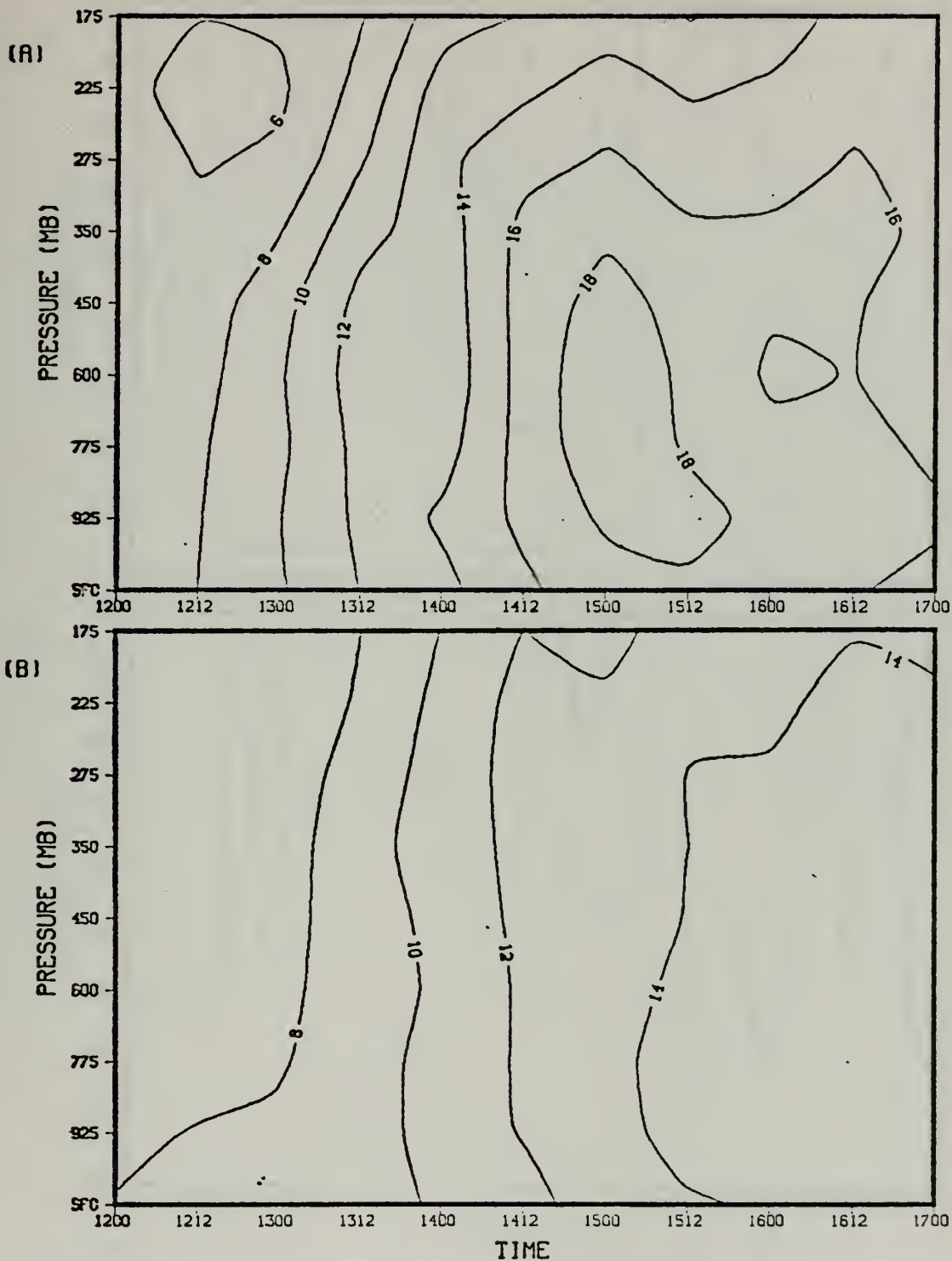


Figure 36. Area-averaged Absolute Vorticity Vertical Time Sections for (A) Radius 6 and (B) Radius 10. Time 1200 Refers to 0000 GMT 12 January. Units are $10^{*-5}/\text{sec}$.

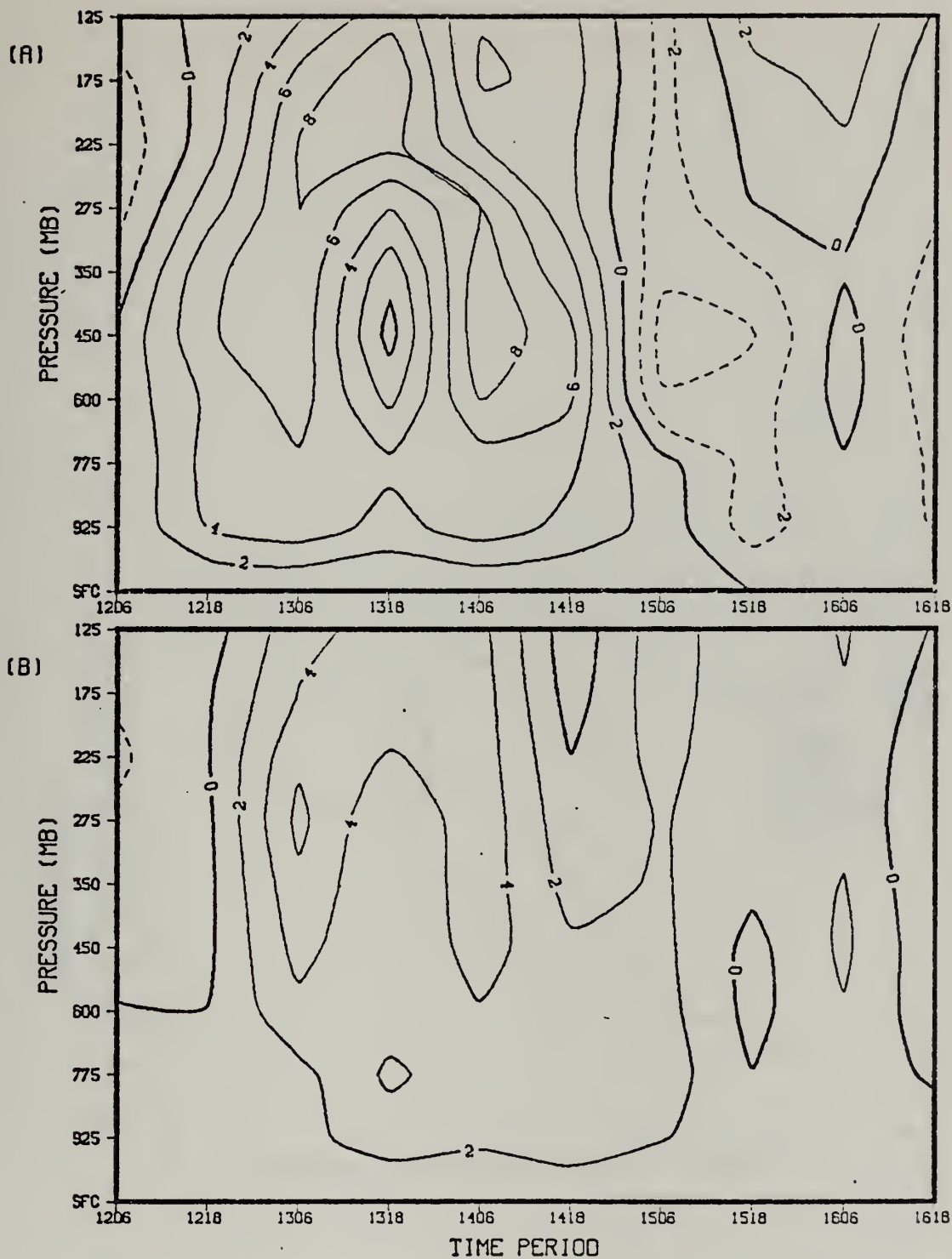


Figure 37. Absolute Vorticity Vertical Time-Tendency Sections for (A) Radius 6 and (B) Radius 10. Period 1206 Refers to 0000-1200 GMT 12 January. Units are $10 \times 10^{-10} / (\text{sec}^2)$. Solid Contours reflect vorticity increases.

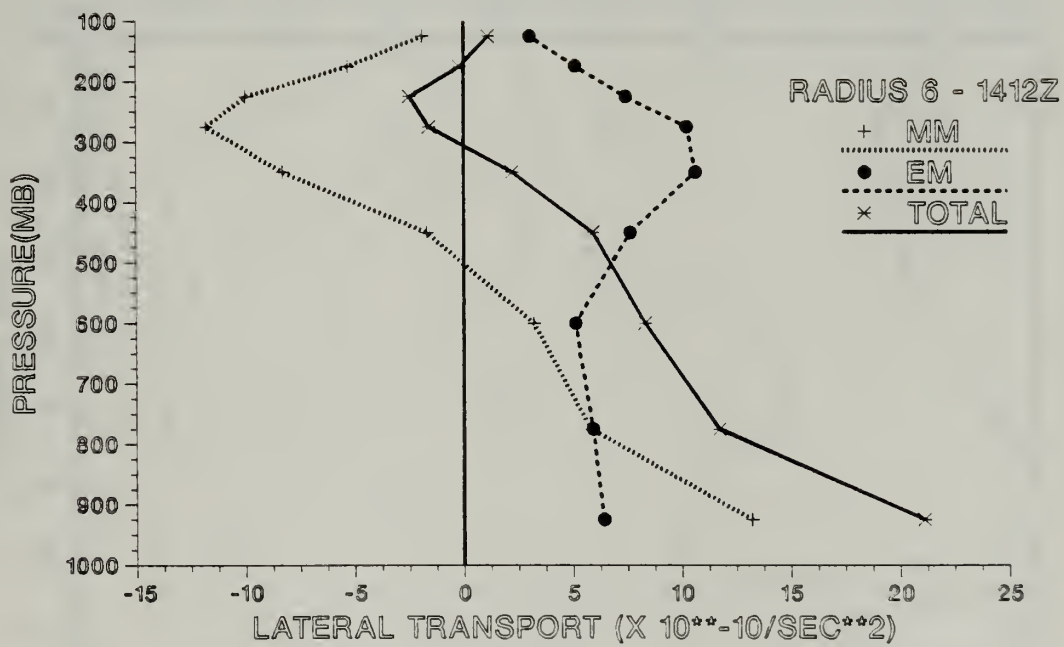


Figure 38. Total, Mean and Eddy Mode Lateral Vorticity Transport During Maximum Development. Time as in Figure 35. Units as in Figure 36.

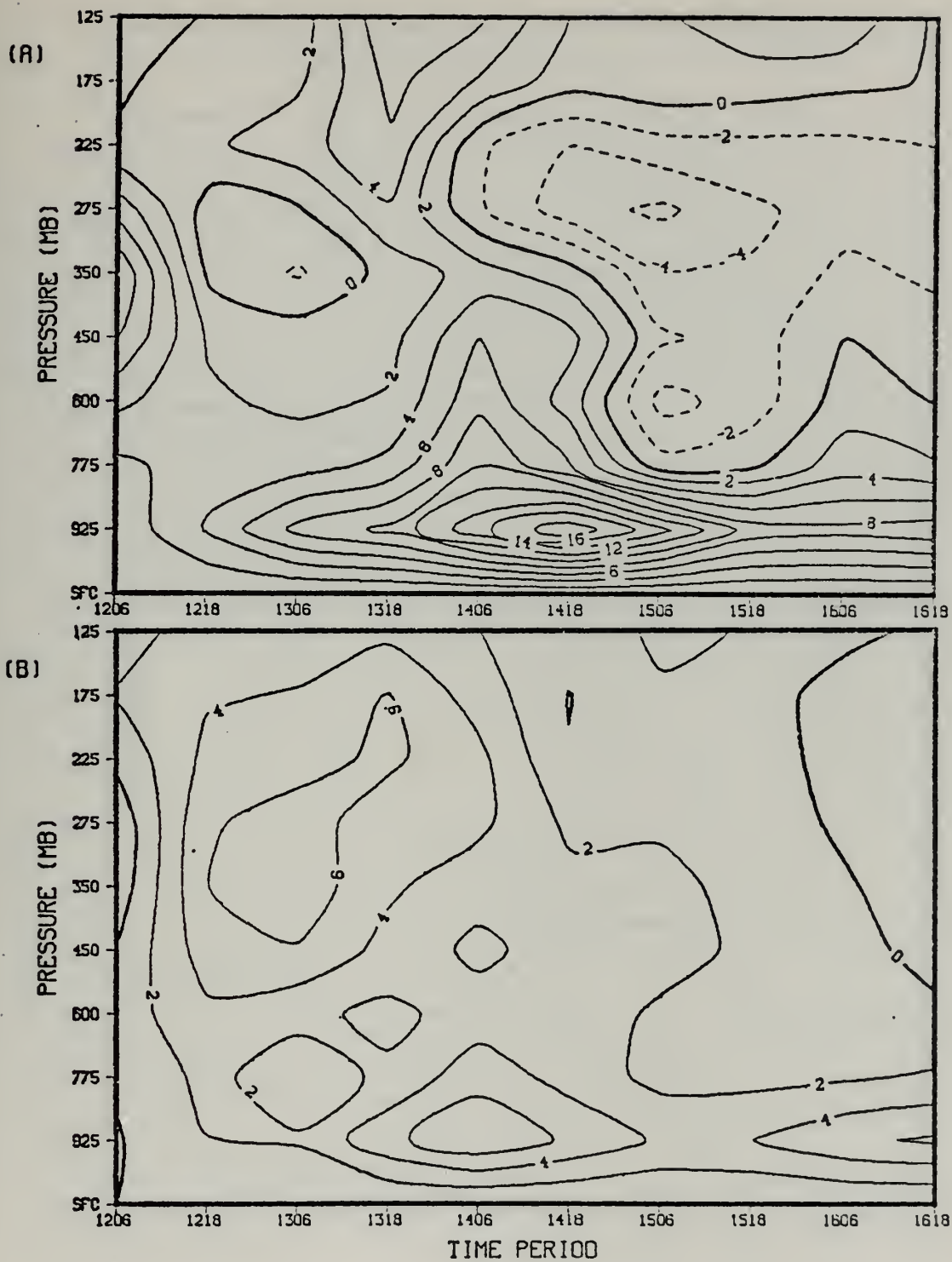


Figure 39. Same as Figure 37 except for Lateral Vorticity Transport.

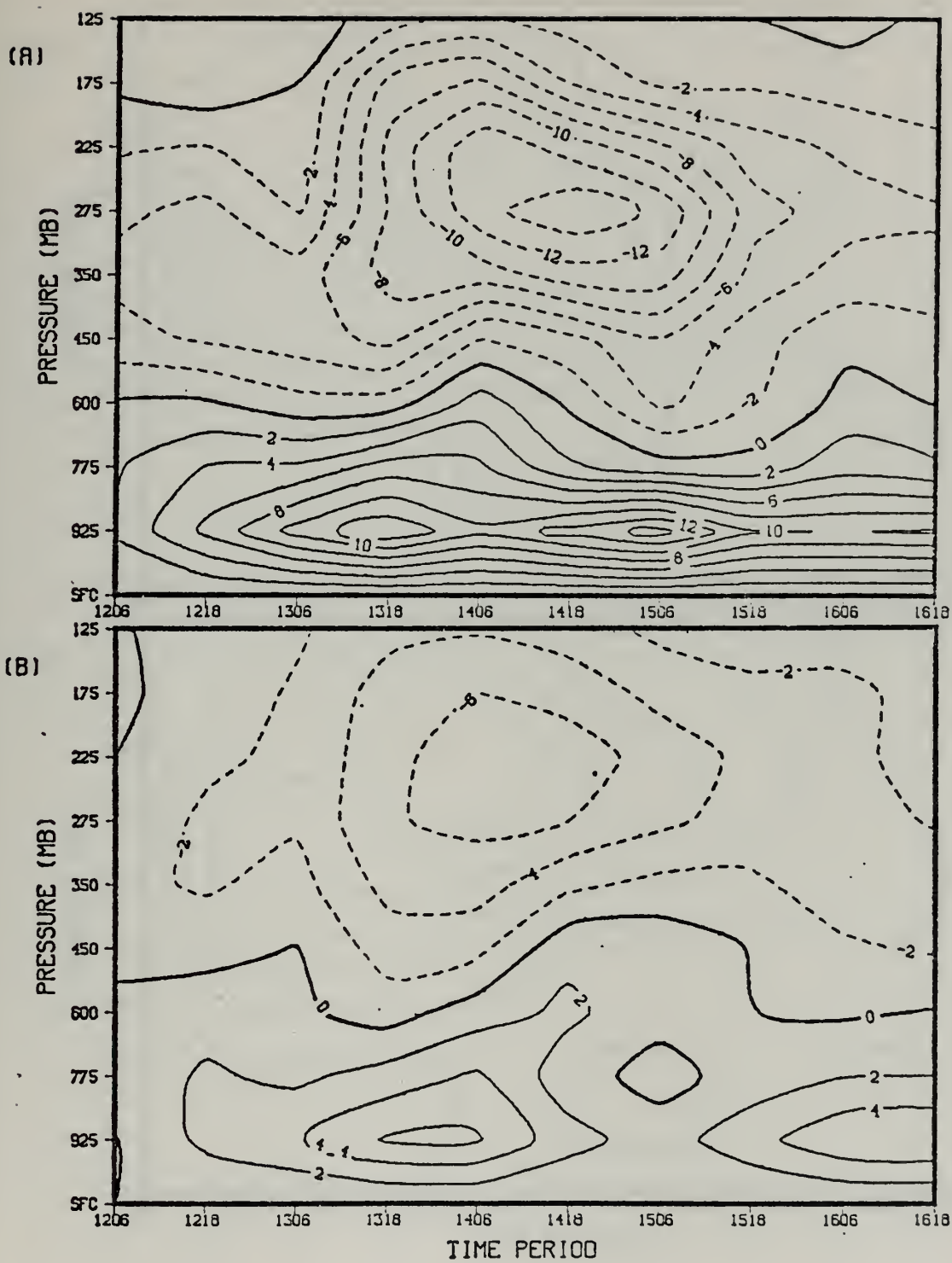


Figure 40. Same as Figure 37 except for Mean Mode Lateral Transport.

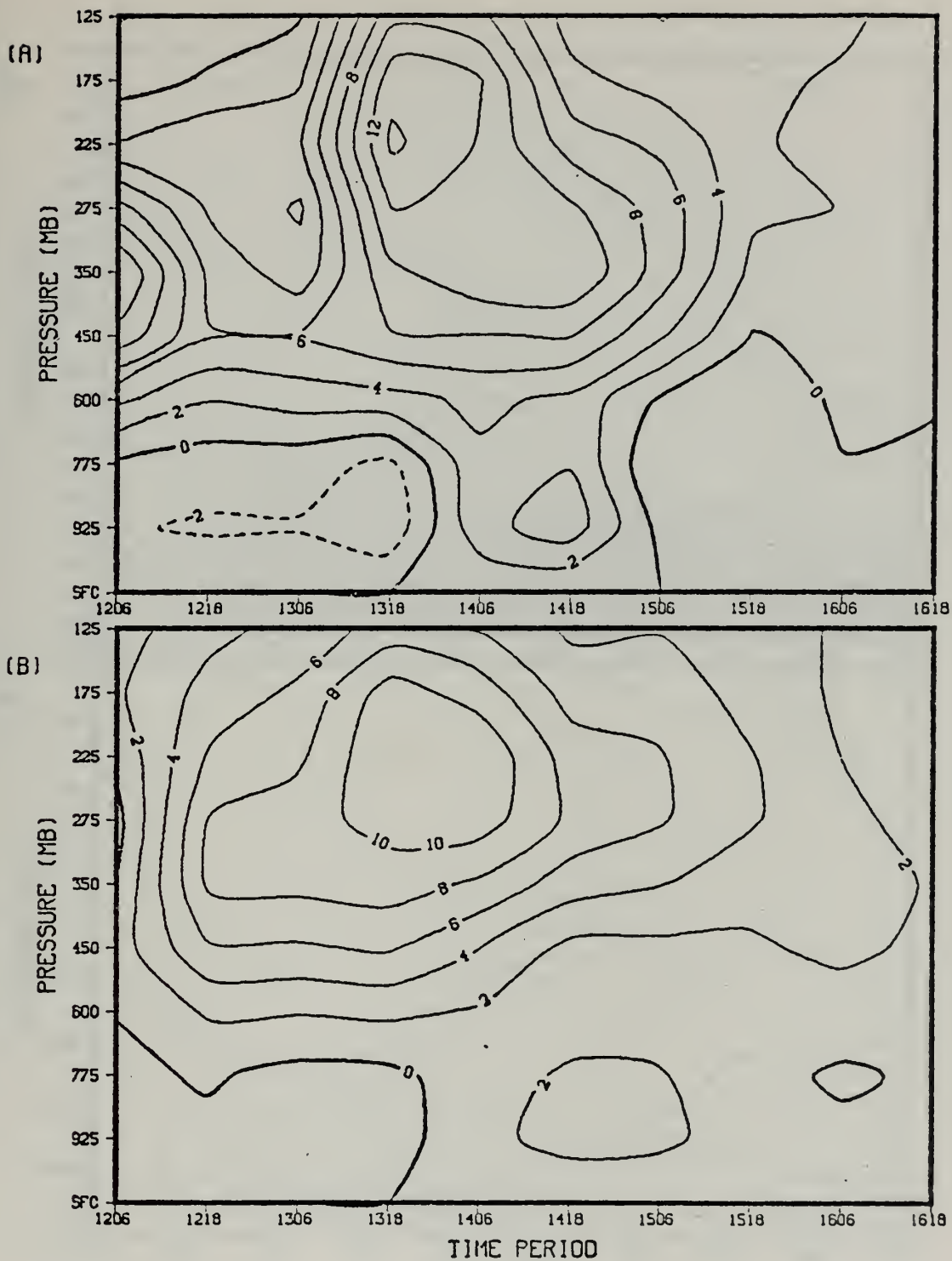


Figure 41. Same as Figure 37 except for Eddy Mode Lateral Transport.

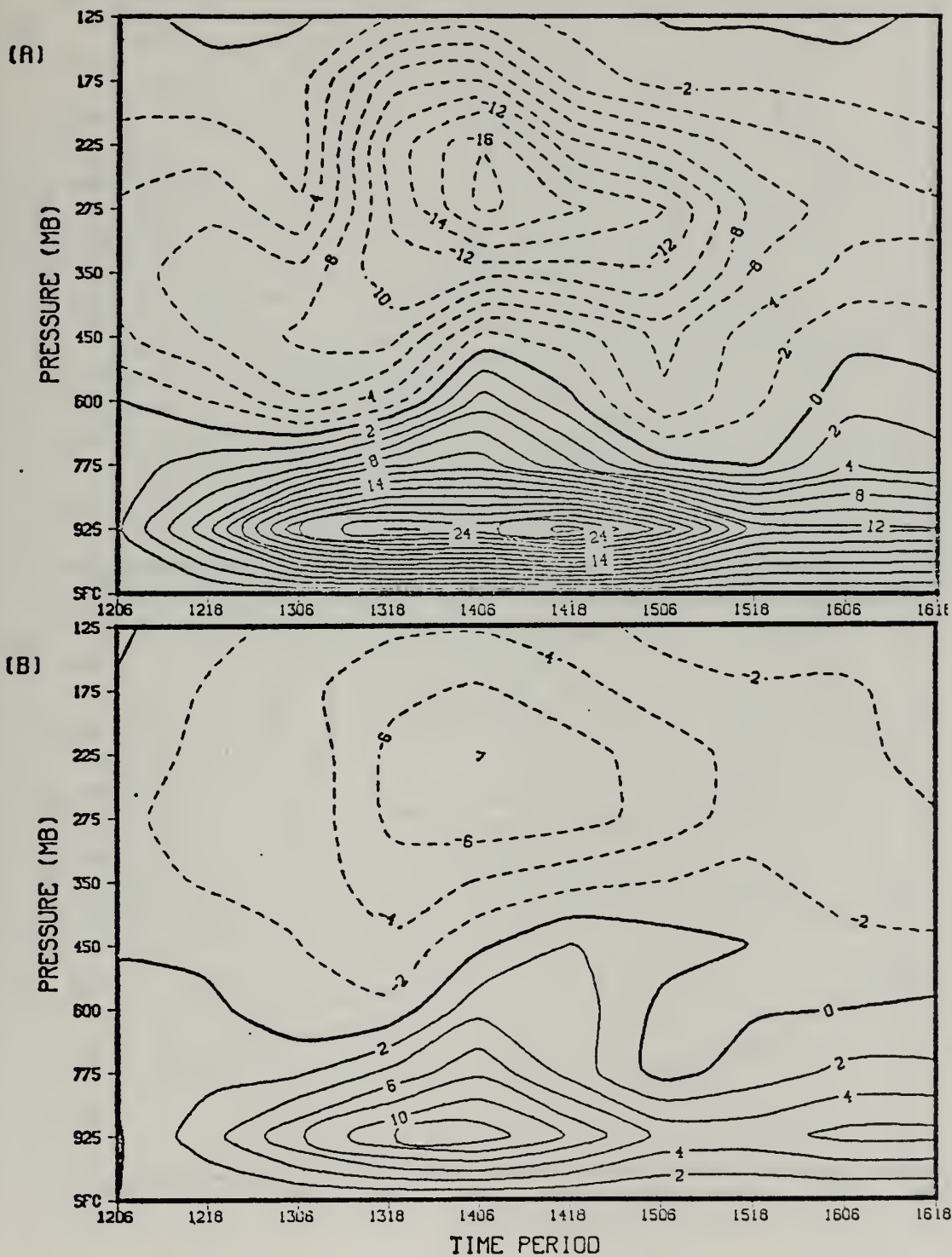


Figure 42. Same as Figure 37 except for Lateral Vorticity Divergence.

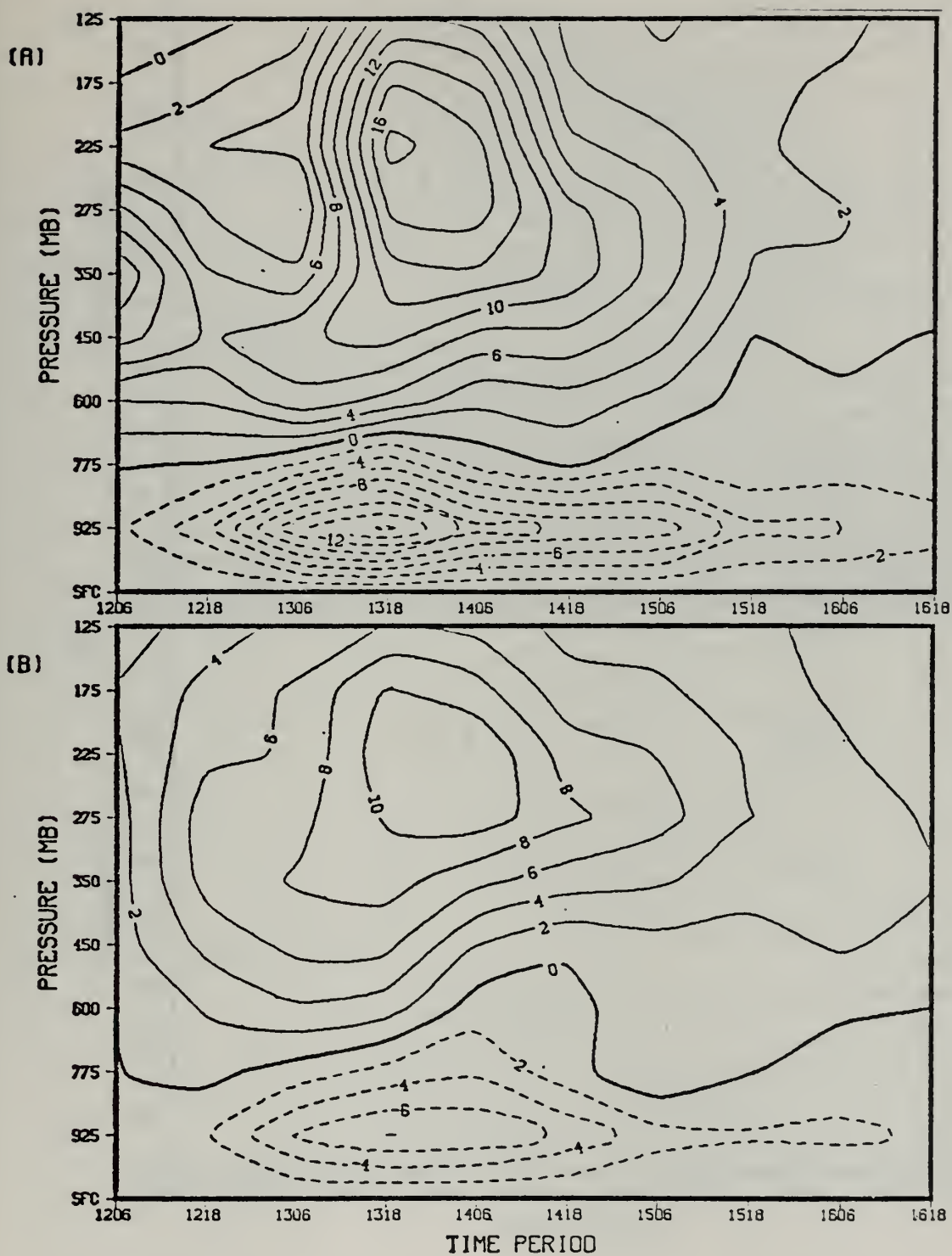


Figure 43. Same as Figure 37 except for Lateral Vorticity Advection.

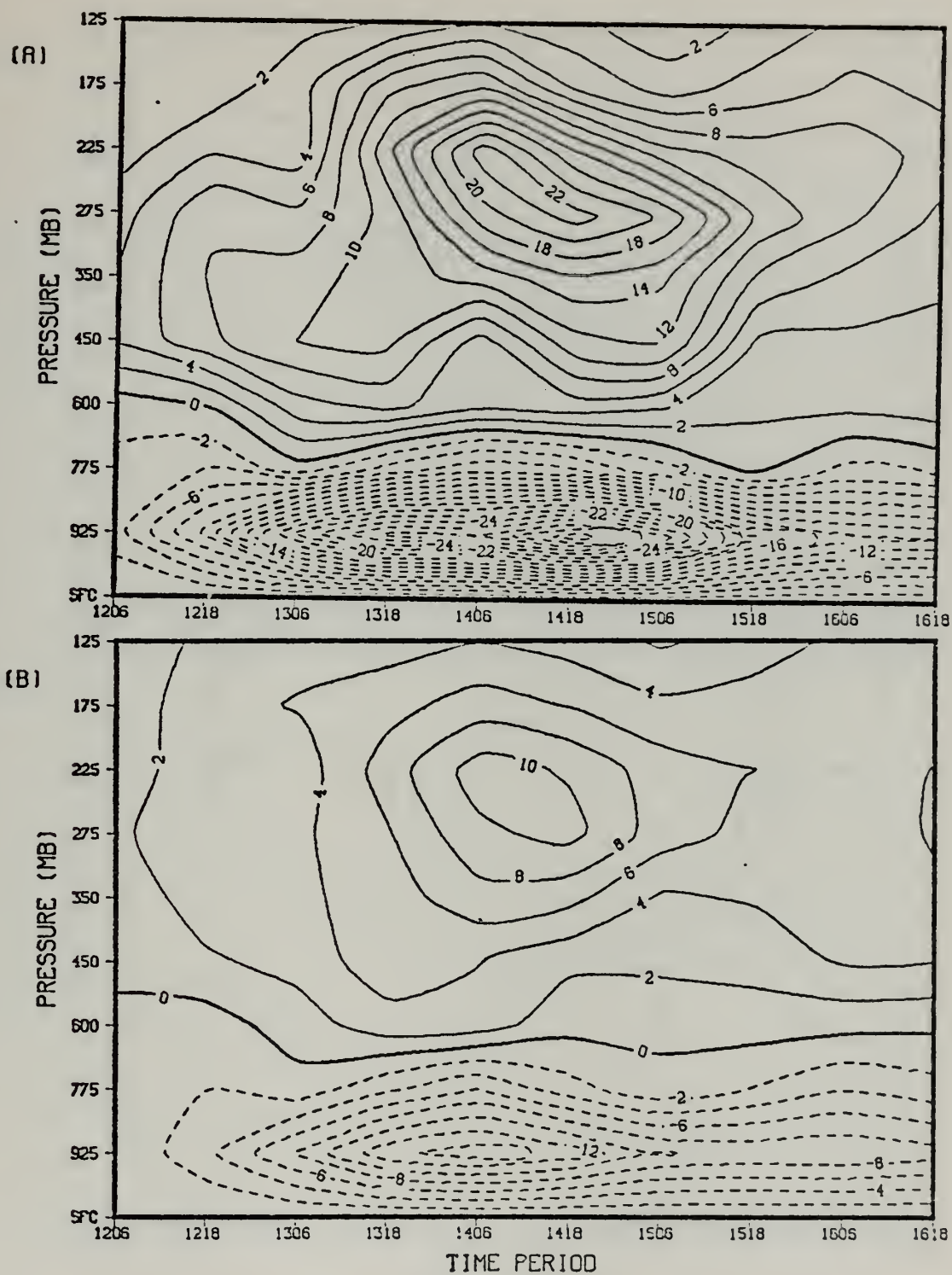


Figure 44. Divergence of the Vertical Transport. Units, times and contours as in Figure 37.

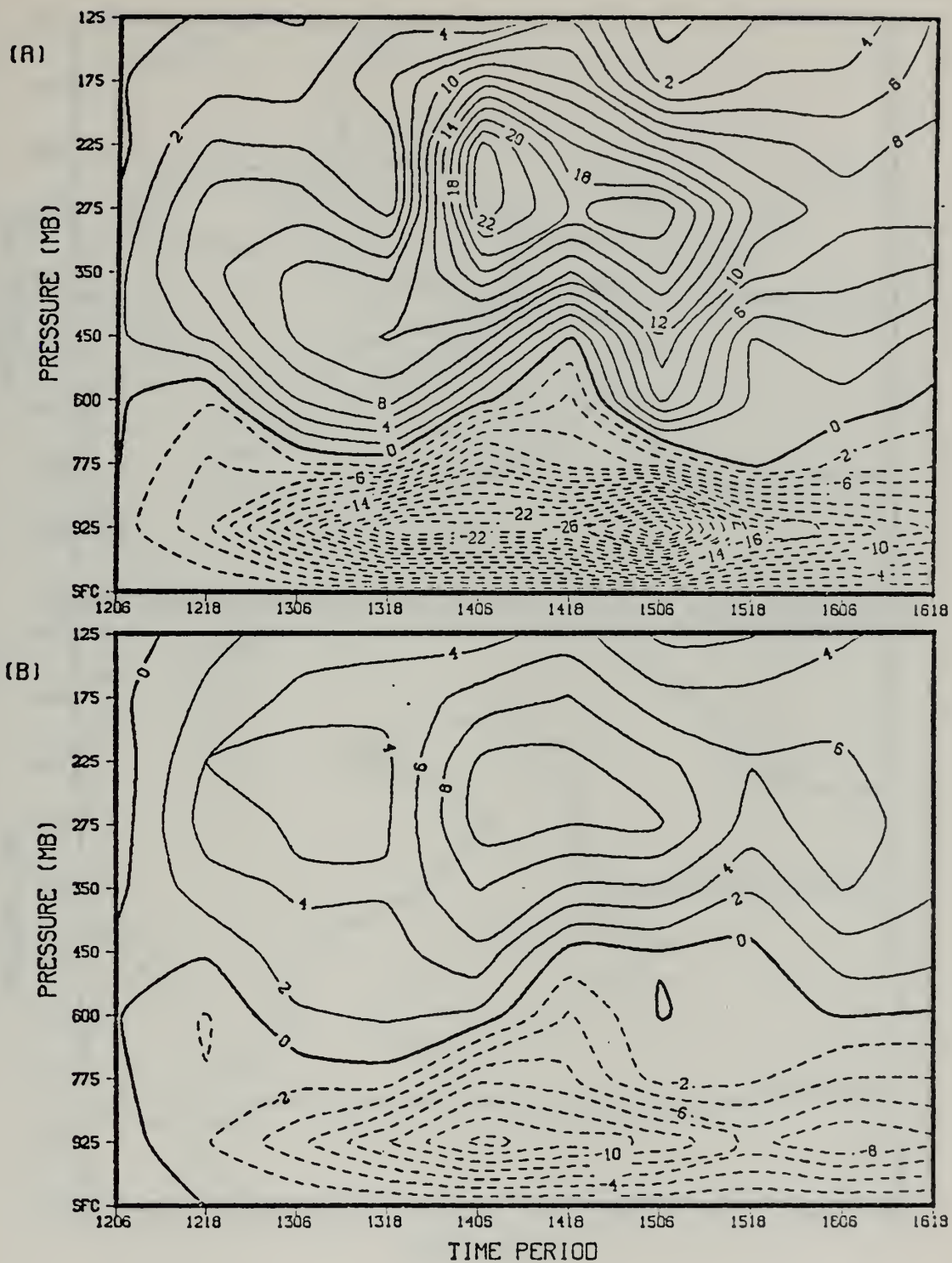


Figure 45. Same as Figure 37 except for Vertical Vorticity Divergence.

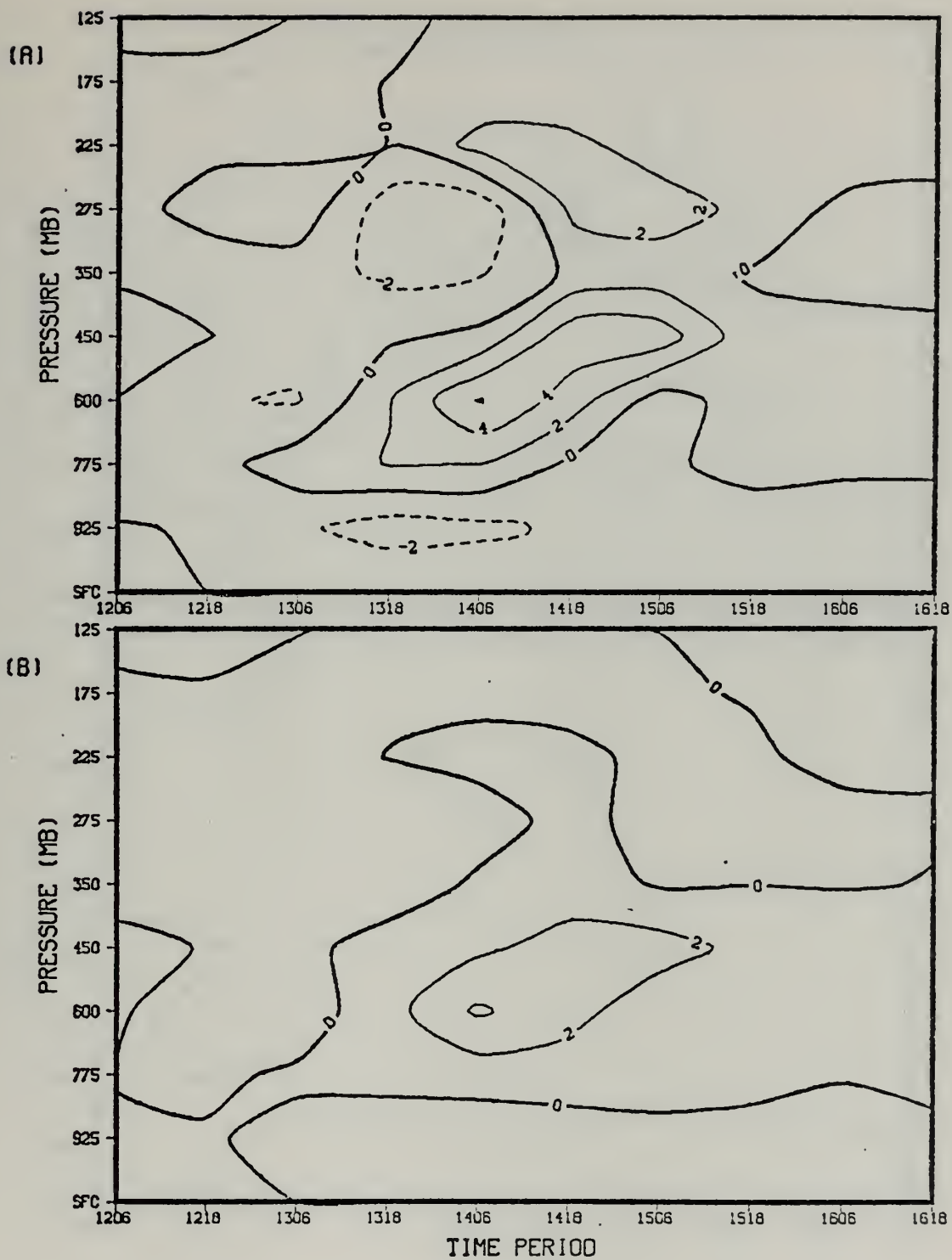


Figure 46. Same as Figure 37 except for Vertical Vorticity Advection.

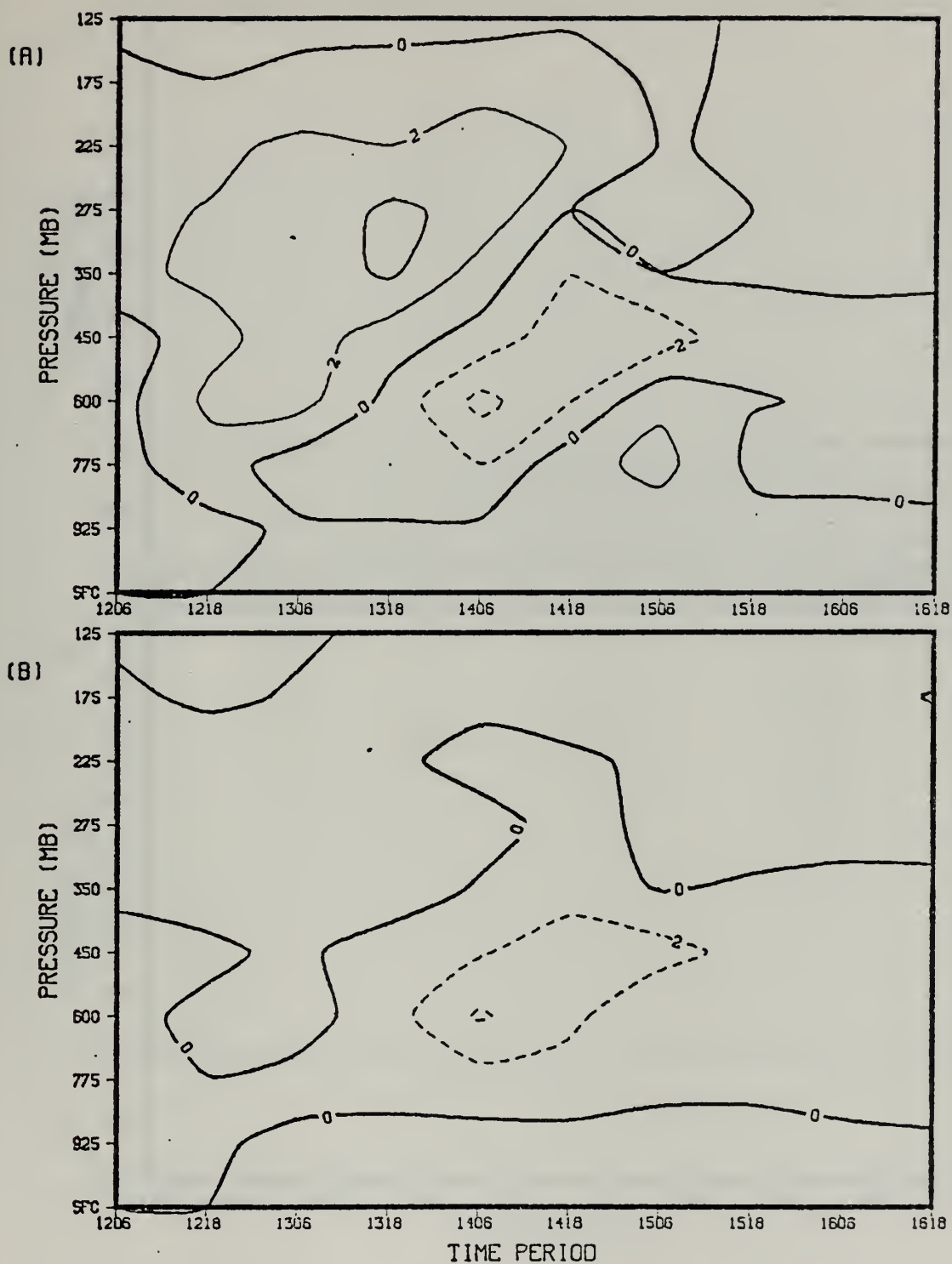


Figure 47. Same as Figure 37 except for the Tilting Term.

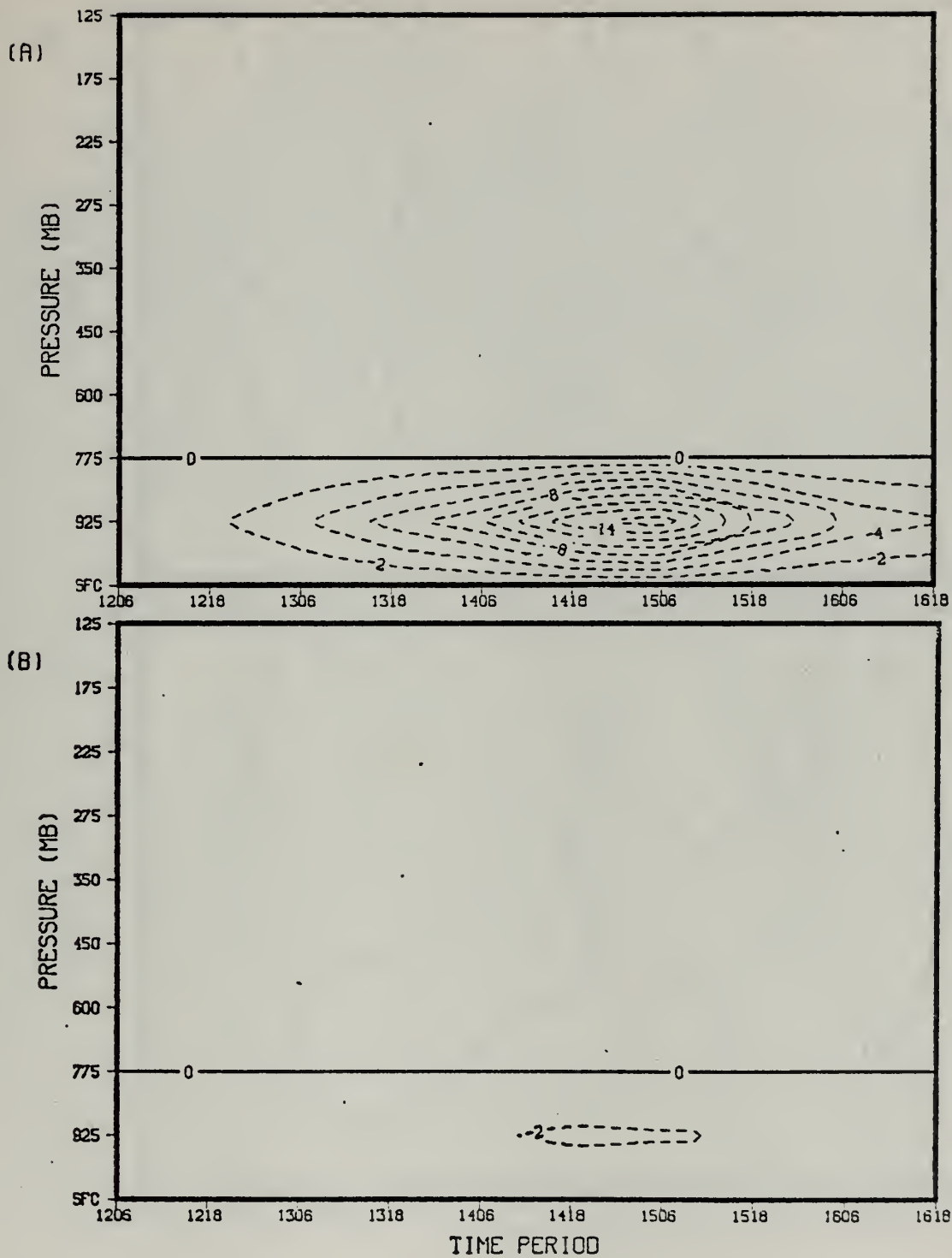


Figure 48. Same as Figure 37 except for Frictional Dissipation.

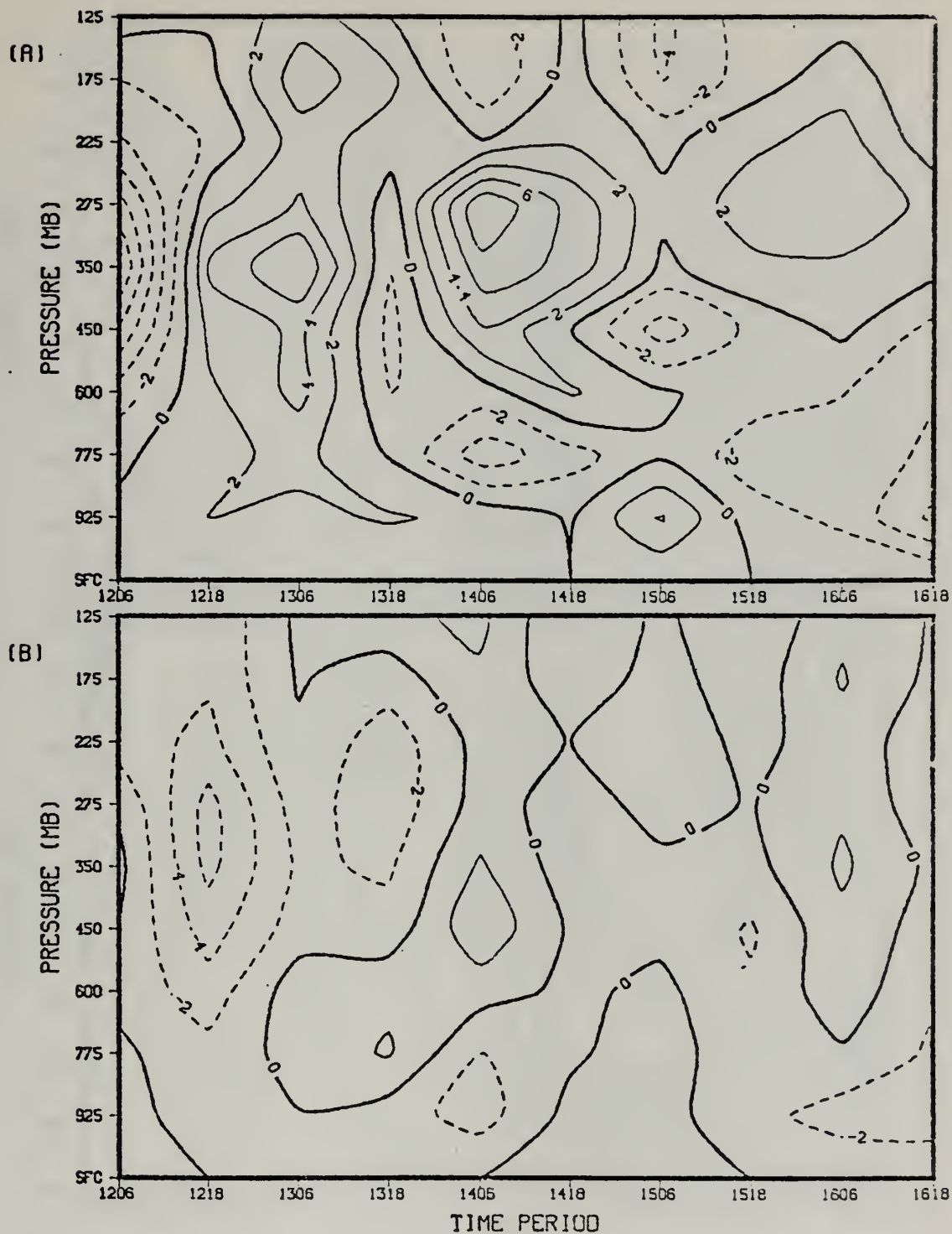


Figure 49. Same as Figure 37 except for Budget Residuals.
 Positive Values Indicate Vorticity Excess.
 Negative Values Indicate Vorticity Deficits.

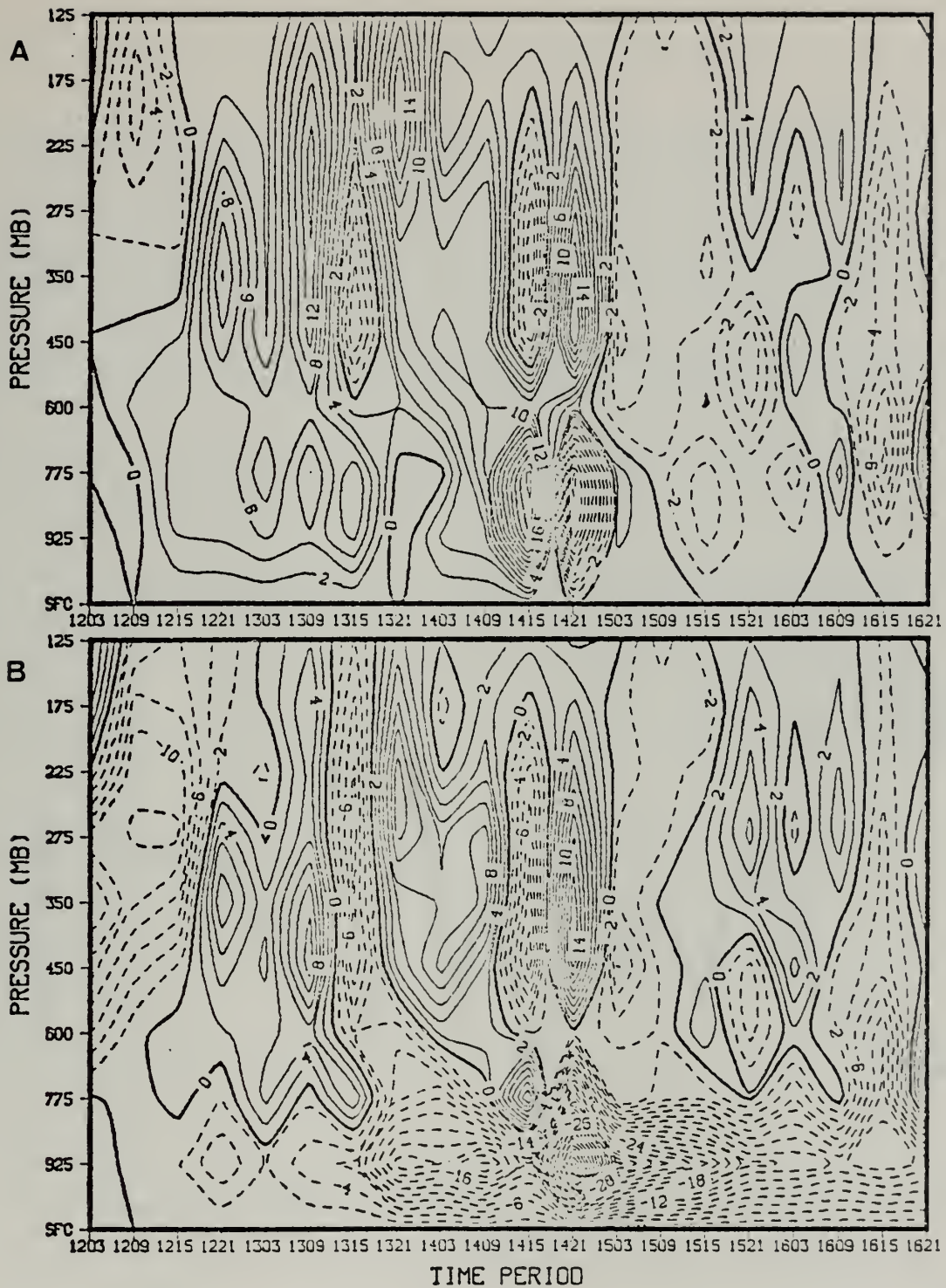


Figure 50. FGGE 6-h Radius 6 Vorticity Budget Fields for (A) Time Tendencies (B) Budget Residuals. Period 1203 Refers to 0000-0600 GMT 12 January and is valid for 0300 GMT. Contours as in Figure 37.

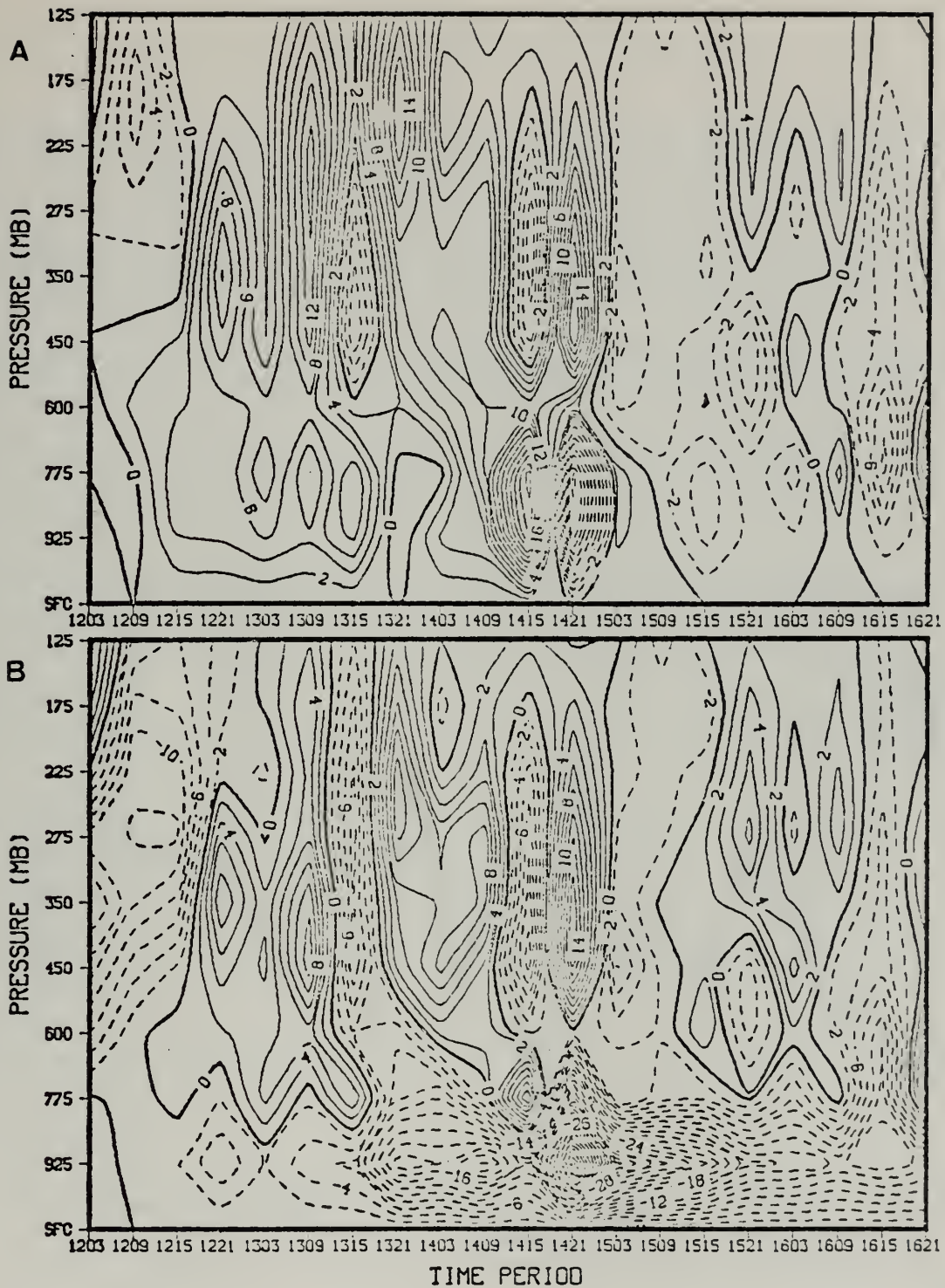


Figure 50. FGGE 6-h Radius 6 Vorticity Budget Fields for (A) Time Tendencies (B) Budget Residuals. Period 1203 Refers to 0000-0600 GMT 12 January and is Valid for 0300 GMT. Contours as in Figure 37.

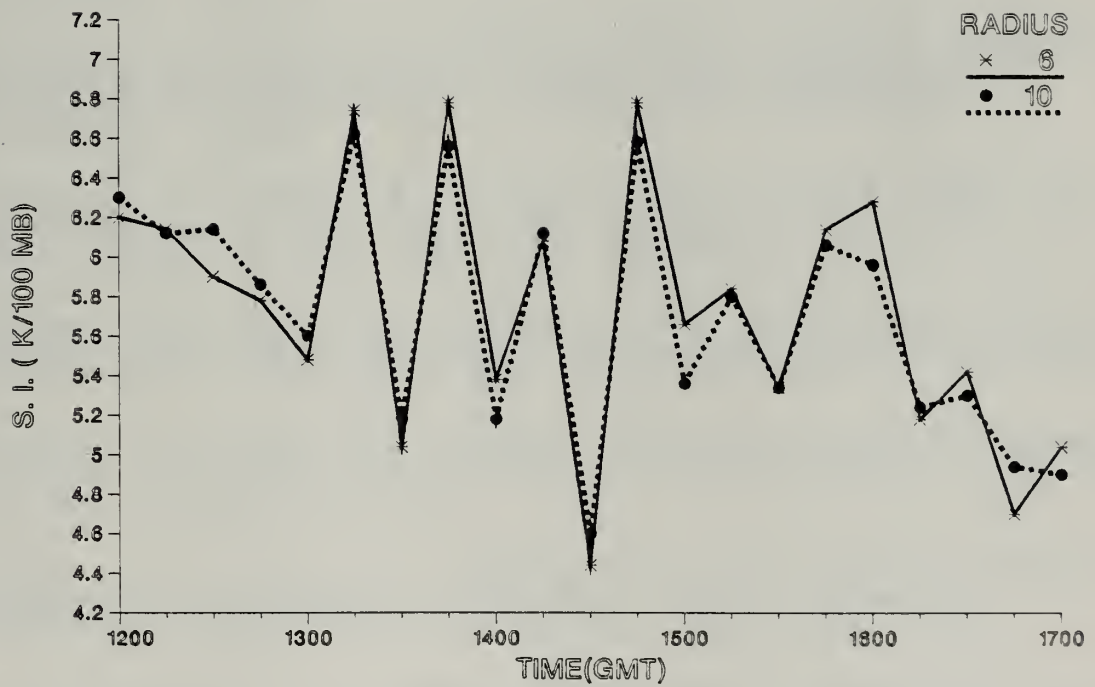


Figure 51. FGGE 6-h Stability Trace. Units and Times as in Figure 28.

LIST OF REFERENCES

- Baker, W. E., E. Edelman, M. Iredell, D. Hahn, and S. Jakkempudi, 1981: Objective analysis of observational data from the FGGE observing systems. NASA Tech. Memo 82062, Goddard Space Flight Center, 132 pp.
- Bengtsson, L., M. Kanamitsu, P. Kallberg, and S. Uppala, 1982: FGGE 4-Dimensional data assimilation at ECMWF. Bull. Am. Met. Soc., 63, 29-43.
- Bjerknes, J., 1956: The diffluent upper trough. Archiv fur Meteorologie, Geophysik und Bioklimatologie, Series A, 17 41-46.
- Conant, P. R., 1982: A study of east-coast cyclogenesis employing quasi-Lagrangian diagnostics. M.S. Thesis, Naval Postgraduate School, 102 pp.
- Gyakum, J. R., 1981: On the nature of explosively developing cyclones in the northern hemisphere extratropical atmosphere. Ph.D. Thesis, Massachusetts Institute of Technology, 225 pp.
- Holland, G. J. and R. T. Merrill, 1983: Tropical cyclone intensification mechanisms. Unpublished manuscript, Department of Atmospheric Sciences, Colorado State University, 56 pp.
- Halem, M., E. Kalnay, W. E. Baker, and R. Atlas, 1982: An assessment of the FGGE satellite observing system during SOP-1. Bull. Am. Met. Soc., 63, 407-427.
- Johnson, D. R. and W. K. Downey, 1975a: Azimuthally averaged transport and budget equations for storms: quasi-Lagrangian diagnostics 1. Mon. Wea. Rev., 103, 967-979.
- Johnson, D. R. and W. K. Downey, 1975b: The absolute angular momentum of storms: quasi-Lagrangian diagnostics 2. Mon. Wea. Rev., 103, 1063-1076.
- Johnson, D. R. and W. K. Downey, 1976: The absolute angular momentum budget of an extratropical cyclone: quasi-Lagrangian diagnostics 3. Mon. Wea. Rev., 104, 3-14.
- Kung, E. C. and W. E. Baker, 1975: Energy transformations in middle latitude disturbances. Quart. J. Roy. Meteor. Soc., 101, 793-815.
- Lemcyne, J., 1982: The Ocean Ranger's night of death. Newsweek. Nr 1, 99, 48.
- Marine Weather Review, 1979: Mariners Weather Log, 23, No. 2, NCAA, 136-140.

Paegle, J., 1983: Some characteristics of ECMWF level III-b data sets. Global Weather Experiment Newsletter, 1, May issue.

Petterssen, S., D. L. Bradbury, and K. Pederson, 1962: The Norwegian cyclone models in relation to heat and cold sources. Geophys. Pub., 24, 243-280.

Petterssen, S. and S. J. Smebye, 1971: On the development of extratropical cyclones. Quart. J. Roy. Meteor. Soc., 97, 457-482.

Roman, D., 1981: Application of quasi-Lagrangian diagnostics and FGGE data in a study of east-coast cyclogenesis. M.S. Thesis, Naval Postgraduate School, 93 pp.

Sanders, F. and J.R. Gyakum, 1980: Synoptic-dynamic climatology of the "bcmb". Mon. Wea. Rev., 108, 1589-1606.

Sandgathe, S. A., 1981: A numerical study of the role of air-sea fluxes in extratropical cyclogenesis. Ph.D. Thesis, Department of Meteorology, Naval Postgraduate School, 134 pp.

Shapiro, L. J. and D. E. Stevens, 1980: Parameterization of convective effects on the momentum and vorticity budgets of synoptic-scale Atlantic tropical waves. Mon. Wea. Rev., 108, 1816-1826.

Wash, C. H., 1978: Diagnostics of observed and numerically simulated extratropical cyclones. Ph.D. Thesis, Department of Meteorology, University of Wisconsin, 215 pp.

Weldon, R. B., 1977: An oceanic cyclogenesis - its cloud pattern interpretation. Satellite Information Note 77/7, NESS Applications Group, NOAA, 1-11.

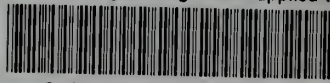
INITIAL DISTRIBUTION LIST

	No. Copies
1. Defense Technical Information Center Cameron Station Alexandria, VA 22314	2
2. Library, Code 0142 Naval Postgraduate School Monterey, CA 93940	2
3. Professor Robert J. Renard, Code 63Rd Department of Meteorology Naval Postgraduate School Monterey, CA 93940	1
4. Professor Christopher N. K. Mooers, Code 68Mr Department of Oceanography Naval Postgraduate School Monterey, CA 93940	1
5. Professor Carlyle H. Wash, Code 63Cw Department of Meteorology Naval Postgraduate School Monterey, CA 93940	9
6. Professor Russel L. Elsberry, Code 63Es Department of Meteorology Naval Postgraduate School Monterey, CA 93940	1
7. Lt. Wynn E. Calland 1201 Williamsburg Way Charleston, W. Va. 25314	3
8. Capt. Alan R. Shaffer, Code 63 Department of Meteorology Naval Postgraduate School Monterey, CA 93940	1
9. Director Naval Oceanography Division Naval Observatory 34th and Massachusetts Avenue NW Washington, D.C. 20390	1
10. Commander Naval Oceanography Command Central NSTL Station Bay St. Louis, MS 39522	1

11. Commanding Officer 1
Naval Oceanographic Office
NSTL Station
Bay St. Louis, MS 39522
12. Commanding Officer 1
Fleet Numerical Oceanography Center
Monterey, CA 93940
13. Commanding Officer 1
Naval Ocean Research and Development
Activity
NSTL Station
Bay ST. Louis, MS 39522
14. Commanding Officer 1
Naval Environmental Prediction Research
Facility
Monterey, CA 93940
15. Chairman, Oceanography Department 1
U.S. Naval Academy
Annapolis, MD 21402
16. Chief of Naval Research 1
800 N. Quincy Street
Arlington, VA 22217
17. Office of Naval Research (Code 480) 1
Naval Ocean Research and Development
Activity
NSTL Station
Bay ST. Louis, MS 39522
18. Commander 1
Oceanographic Systems Pacific
Box 1390
Pearl Harbor, HI 96860

thesC1914

Quasi-lagrangian diagnostics applied to



3 2768 002 08457 6

DUDLEY KNOX LIBRARY